Università degli Studi di Genova
Dipartimento di Chimica e
Chimica Industriale

Organic & Hybrid Photonic Crystals for Controlling Light-Matter Interaction Processes

Giovanni Manfredi
PhD candidate in
Scienza e Tecnologia della Chimica e dei Materiali
XXX Ciclo

Advisor:
Prof. Davide Comoretto

Index

Chapter I

Introduction

In the last years, the properties of light in periodically modulated dielectric materials have been under the spotlight of scientific research.[1] A great effort has been posed in the theoretical and experimental development of these structures since they allow to guide photons in otherwise unconceivable trajectories, to localize and confine them in small volumes, and to engineer light-matter interaction.[2]

Photonic crystals (PhCs) are an advanced class of materials that can be used in a variety of applications from optoelectronics to biosensors. They are similar to semiconductors[2] where the presence of an electronic potential creates energy bands of allowed or denied electron energies. The periodic distribution of dielectric materials having different refractive index on sub-micrometer scale creates a photonic band gap (PBG) that deny the propagation of photons inside the lattice. The spectral position of the PBG, which is basically the PhC color, can be tuned acting on the refractive index of the composing materials or on the lattice spacings. It is then easily possible to modify the spectral properties of the crystal just modifying some parameters, opening the way to many possibilities, for example photoswitching or sensing.[3-8]

Inorganic PhCs allow to have very high-quality structures exploiting well established production methods like vapor deposition or lithography.[9-11] These technologies are indeed quite interesting but a particular interest may be directed toward methods that enable easily scalable and cost-effective manifactures.[12]

In this regard, polymers are a class of materials that could be processed through such technologies. A special academic, institutional, and industrial interest is posed on these materials and on plastic photonics.

Even the European Union is interested in the development of organic electrooptical and photonic devices. There have been funded projects aimed to engineer low cost photonic devices easy to produce and flexible, properties hardly achievable through the use of inorganic materials. The aim is to create synergies between industries and academy to place Europe in a leading position in the commerce and development of photovoltaics, informatics and optoelectronics.[13-14]

Considering this hectic and inspiring background, this thesis is focused on the production of planar polymer PhCs for different applications. Such structures are composed by alternated layers of polymers having different refractive index. Since they are much simpler than 2D or 3D PhCs, they can be produced for commercial uses through techniques like melt-processing[15-16] even though, on lab scale, spin coating is more versatile.

Such devices can be used in multiple applications as antireflective coatings, optical microcavities, planar waveguides and optical switches.

Here, we present their use for sensing, emission reshaping, and lasing. Moreover, the thesis will discuss about the production of polymer multilayers using spin coating.

Thesis structure

This thesis reports the main results obtained by the candidate during its PhD studies period. It is divided in 5 main chapters. In the introduction, we present the main concepts necessary to understand the thesis. We explain the concept of PhC, the properties of planar PhCs, the advantages and disadvantage of using polymers, and the technique used to create samples presented and discussed in the work. The chapters from 2 to 5 are dedicated each one to a different subject studied during the PhD period. Each of these chapters is introduced explaining the reasons behind the work and reports the obtained results. Moreover, they are thought so that a reader can skip directly to the relative chapter without reading the previous ones if he's interested in a specific topic.

Chapter 2 is dedicated to the study of spin coating of polymer layers for photonic applications. The majority of the experimental work for this chapter has been conducted in the Dresden center for integrated and applied photonics.

Chapter 3 is dedicated to the modelling of the optical response of polymer planar PhCs for sensing applications.

Chapter 4 and 5 are dedicated to the use of core shell nanocrystals in polymer PhC to obtain emission reshaping and lasing, respectively.

The chapters are heavily inspired by works published by the author during the PhD or by works in preparation that are going to be submitted for publication. Therefore, substantial part of the results may be already found in literature.

Given the difference among the treated subjects, the thesis has been written in a succinct way. All the details about the experimental methods are reported only if significant to the discussion. A general chapter about experimental methods is deliberately omitted since scarcely interesting from a scientific point of view. Even the theory is kept as simple as possible and recalled only when needed in order to simplify the treatment.

Even though this is not a common approach, we find it more suitable to the aim of this thesis which is to give a summary about some proof-of-concept devices created during the author's studies for PhD degree.

Photonic crystals

A photonic crystal is a material composed by a lattice of media having different refractive index. Such lattice has spacings in the order of the visible light wavelength, hence, the typical feature size of a PhC is in the order of some hundreds of nanometers. The presence of many media having different refractive index creates an ordered array of interfaces that can diffract light. Then, the photons scattered in the system can coherently interfere modifying the dispersion relations and the density distribution of photonic states.[17]

It is important to notice that PhC lattice spacings are somehow in an intermediate dimension between atomic scale and macroscopic scale. Indeed, the period must be much longer than the bond length, which is typically in the order of atomic Bohr radius of ~0.5 Å, and shorter than the size of a macroscopic media. The light must indeed encounter a series of different materials so that each one has its own refractive index (this limits the shorter

lattice spacings) but still be able to coherently interfere with the light diffracted at each interface (this limits the longer lattice spacings).
The materials composing a PhC can either be completely transparent or show an extinction coefficient, however, we focus on the case of materials having only a real refractive index and no absorption.
In this type of structures, photons propagation is similar to the one of electrons inside a semiconductor.[1-2, 12, 17] In particular, only photons having specific energies can propagate inside the crystal, while for some energy bands called photonic band gaps (PBGs), propagation is strongly hindered. This is the reason behind the PhCs structural color. Indeed, since no photon can propagate inside the crystal, all the light hitting it with a specific wavelength inside the PBG will be reflected or diffracted in specific directions. Such phenomenon is also responsible for the iridescence (change of color upon observation angle) of such systems. Iridescence and selective reflectance are quite strong in PhC and such nanostructures are extensively used in nature by some animals or plants to obtain gaudy colors or to camouflage themselves.[18-20]
A particular kind of crystal is the distributed Bragg reflector (DBR) composed by alternated layers of two materials having different refractive index. The structure is schematized in Fig. 1.1.

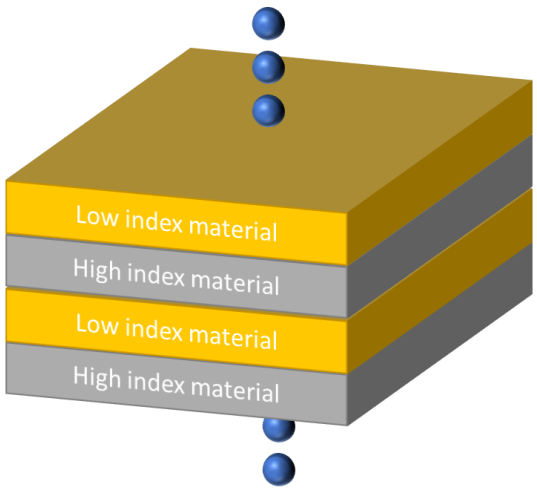

Fig. 1.1 Schematized structure of a DBR

As every PhC, this kind of planar structure creates a PBG which hinders photon propagation. However, due to the planar shape, the only allowed diffraction direction is the backward one. Indeed, if a photon having frequencies inside the crystal PBG hits a DBR, it is strongly reflected. This makes the optical characterization of DBRs quite convenient as it requires simple techniques. The PBG of a DBR is clearly visible in the reflectance spectra as a pronounced peak which position, intensity, and width depend upon the crystal parameters (Fig. 1.2). Moreover, the reflectance background of a DBR shows a series of fringes which are created by the interference of each layer.

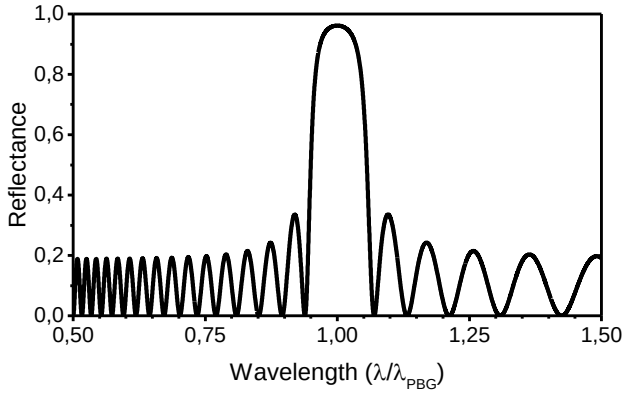

Fig. 1.2 Typical reflectance spectra of a polymer DBR

The planarity also helps in the theoretical study and the optical properties of these structures can be replicated using simple models.[17, 21-22]
Indeed, the spectral position of the band gap, λ_{PBG}, is linked to the properties of the layers composing the system and depends upon the light polarization. It follows the laws:[22]

$$\lambda_{PBG} = 4(d_H + d_L)\frac{n_H n_L \cos\theta_H \cos\theta_L}{n_H \cos\theta_H + n_L \cos\theta_L} \quad \text{TE polarization} \tag{1.1}$$

$$\lambda_{PBG} = 4\frac{d_H \cos^2\theta_H + d_L \cos^2\theta_L}{n_H \cos\theta_L + n_L \cos\theta_H} \quad \text{TM polarization} \tag{1.2}$$

Here, n_H, d_H are the refractive index and thickness of the high index material and n_L, d_L are the refractive index and thickness of the low index material. $\theta_{H,L}$ are the light propagation angles inside the high and low index material which can be derived by Snell law $n_i \sin\theta_i = n_j \sin\theta_j$. Eqs. 1.1 and 1.2 also consider the angle of incidence of the light. Indeed, the PBG shifts for different angles of incidence as the optical path encountered by photons inside the photonic structure is different. Fig. 1.3 shows a contour plot of the reflectance of a DBR as a function of wavelength and light angle of incidence. The reflectance has been calculated using transfer matrix method.[21] The top panel shows the reflectance of s-polarized light. This correspond to the TE polarization where the electric field oscillates on the plane of the sample only. In these conditions, the PBG rigidly shifts toward lower wavelengths as the incidence angle grows. The bottom panel, instead, shows the reflectance calculated for p-polarized light. This is the TM polarization where the electric field oscillates parallel to the plane of incidence. In these conditions, the PBG blueshifts as in the case of s-polarization but also reduces its width. This effect is mainly caused by the reaching of Brewster-angle of the materials composing the system which drastically reduces the reflectance of p-polarized light.

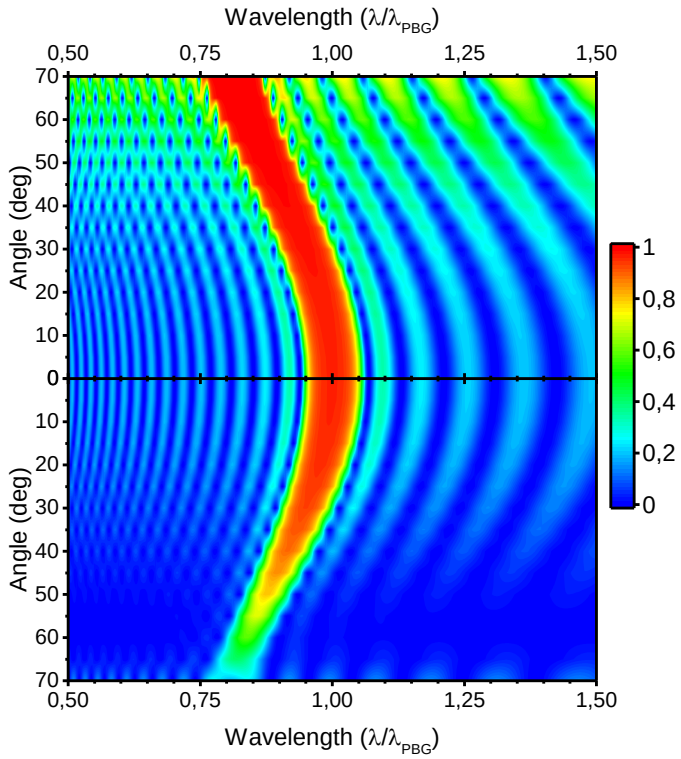

Fig. 1.3 Angular dependence of a DBR reflectance for s-polarization (top panel) and p-polarization (bottom panel).

Due to this angular dependence, some authors prefer not to talk about PBG but instead about photonic stop band for DBRs. Indeed, they do not consider the high reflectance band as a real PBG because DBRs photon propagation inhibition is not omnidirectional and for each wavelength there will always be a direction that can allow light transmission. However, aware of this terminology issue, we still prefer to use the term PBG due to the similarity of the two effects.

When studying DBRs, it is interesting to consider a special condition which the layers composing the system may fulfill. This is called the $\lambda/4$ condition and happens when the optical paths of the high and low refractive index layers are identical. In such case, the system reflectivity is maximized and can be easily calculated using the formula:

$$R_{PBG} = 1 - 4\left(\frac{n_L}{n_H}\right)^N = 1 - 4\left(1 - \frac{\Delta n}{n_H}\right)^N \quad (1.3)$$

Where N is the number of bi-layers composing the system and Δn is the dielectric contrast of the materials. The reflectivity increases with the number of bi-layers and with the dielectric contrast (Δn).

This last parameter is also very important in defining the spectral width of the PBG. In fact, in $\lambda/4$ condition, the width (in energy) is ruled by:

$$\Delta E_{PBG} = \frac{4E_{PBG}}{\pi}\frac{n_H - n_L}{n_H + n_L} = \frac{4E_{PBG}}{\pi}\frac{\Delta n}{2n_L + \Delta n} \quad (1.4)$$

Where E_{PBG} is the energy of the first order PBG. Fig. 1.4 reports the PBG width as a function of dielectric contrast considering n_L=1.5, a value not distant from the one of low index materials commonly used for DBRs. The width grows monotonically and almost linearly with the contrast in the considered interval.

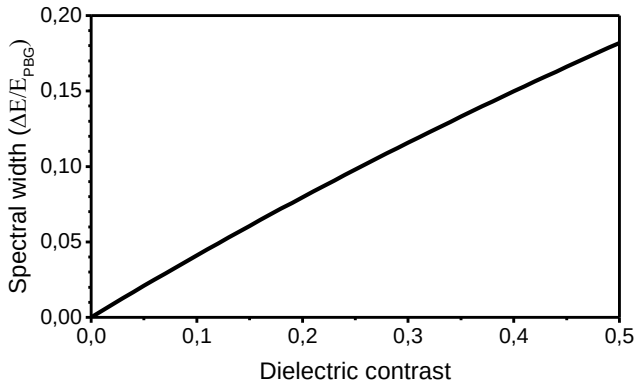

Fig. 1.4 Calculated width of a PBG in a DBR in $\lambda/4$ condition.

The $\lambda/4$ condition has other effects other than maximizing the reflectivity. In particular, it destroys each even order PBG replica. Indeed, in a DBR, the PBG created at the wavelength supplied by Bragg-Snell law λ_{PBG} presents higher order replicas depending upon the relative thickness of the layers composing each repetitive unit in the system. Such replicas, neglecting index dispersion, are positioned at λ_{PBG}/m where m is natural non-zero number. Fig. 1.5 shows the calculated reflectance spectra of a DBR as function of energy and relative optical path of the high index layers. The latter is calculated as the ratio between the optical path of the high index material layers and the optical path of a whole bi-layer. It goes from 0 (no high index material) to 1 (only high index material) and is 0.5 only in the $\lambda/4$ condition. The spectra have been calculated maintaining the total optical path constant so that the first order PBG position is fixed. For the calculation, we also neglected refractive index dispersion. The first order PBG (visible as a red band at 1 on x-axis) is always present except, of course, at the extreme cases of no high index material or no low index material. The PBG at orders over the first, instead, are not always present. In particular, for equal optical paths in the bi-layer, all the even orders disappear as already mentioned. In real cases, the refractive index dispersion may change the properties of the first PBG replicas, however, in limited spectral ranges like the one of visible light, and considering we use transparent materials, the index dispersion is usually so weak that the major effect it can cause is just a small shift of the second, third or fourth order PBGs from the exact $\lambda_{PBG}/2$, $\lambda_{PBG}/3$, or $\lambda_{PBG}/4$ positions.

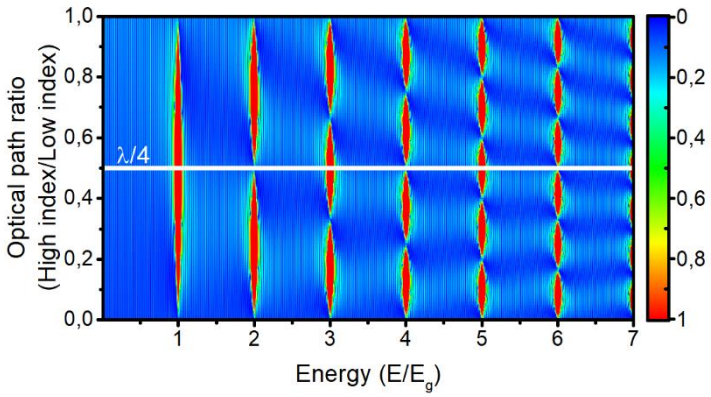

Fig. 1.5 Contour plot of calculated DBR reflectance as a function of optical path ratio and energy.

PhCs works exploiting the periodicity of their dielectric lattice. If this periodicity is violated, new states are created inside the PBG. Such states are also called cavity modes and the defect in the periodicity is called cavity or microcavity. For extension, also the whole structure can be called microcavity.

In this thesis, we focus on planar microcavities which are formed when periodicity defects are inserted inside a DBR. Such defects can be layers of different thickness or made of a different material and take the name of cavity or defect layers. The typical structure is reported in Fig. 1.6 and the typical reflectance spectra of such systems is reported in Fig. 1.7. A low reflectance (high transmittance) sharp frequency interval is created inside the otherwise high reflectance band given by the periodic photonic structure. Also, the fringes outside of the PBG (Fig. 1.2) are modified and split. The position of the cavity mode inside the PBG depends upon the optical path of the cavity layer and, if the latter is large enough, there can be more than one cavity mode as shown in Fig. 1.8. The dependence of the cavity mode from the defect layer optical path can be used to obtain photoswitching as also proven by a paper co-authored by the author of this thesis.[5]

Moreover, cavity modes are extremely localized states; the electric field in strictly confined by the defect and enhanced in a very narrow physical space as reported in Fig. 1.9. Consequently, the interaction between the electric field and any photoactive material is strongly altered.[1-2, 17]

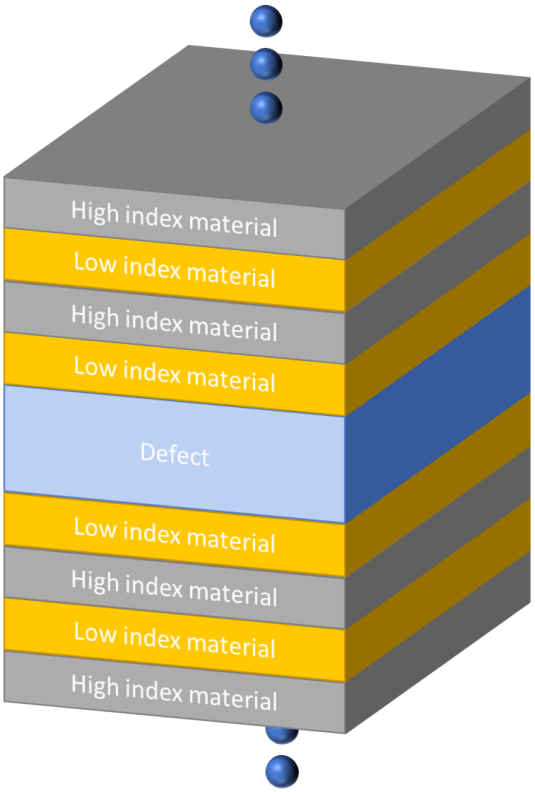

Fig. 1.6 Schematical structure of a planar microcavity.

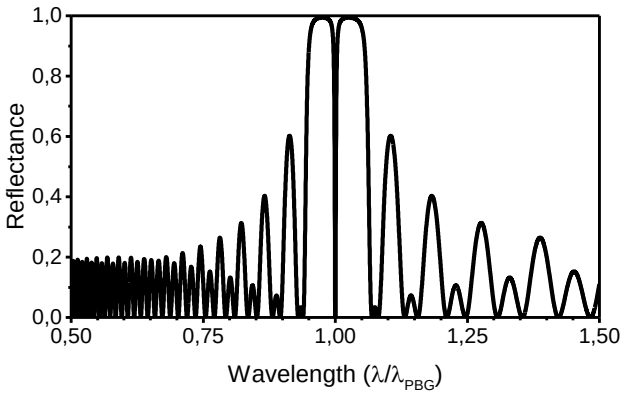

Fig. 1.7 Typical reflectance spectra of a polymer planar microcavity.

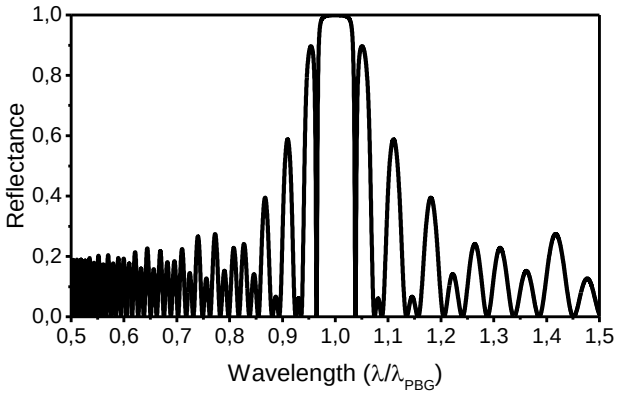

Fig. 1.8 Typical reflectance spectra of a large cavity polymer planar microcavity.

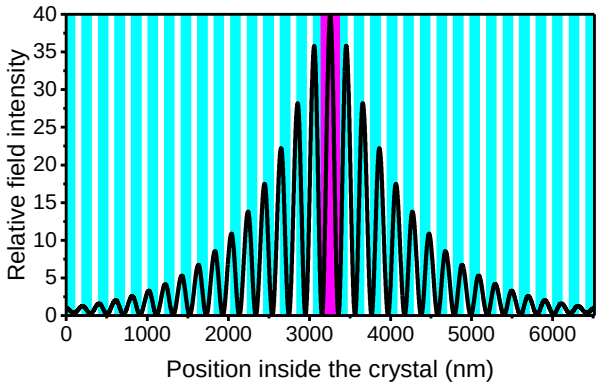

Fig. 1.9 Relative field intensity inside a polymer planar microcavity.

The field localization is a very important effect strictly correlated to the optical quality of the system. The higher the reflectivity of the DBRs composing a microcavity the stronger the confinement and the relative field enhancement will be. Since lot of phenomena like Purcell effect[23-26] and strong coupling[27-30] depends upon the volume of the cavity mode, it is necessary to have a figure of merit which immediately suggest the efficiency of the system. Such figure of merit is the cavity quality factor. Comparing a microcavity to a Fabry-Perot etalon, indeed it is possible to immediately extract the Q-factor from a transmittance or reflectance spectrum as:

$$Q = \frac{\lambda_c}{\Delta\lambda_c} \tag{1.5}$$

Where λ_c is the cavity mode spectral position and $\Delta\lambda_c$ is the cavity mode spectral full width at half maximum.
The Q-factor is also linked to the cavity photon dwelling time by the simple law

$$\tau_{dwell} = \frac{Qn\lambda_c}{2\pi c} \quad (1.6)$$

Where n is the cavity refractive index and c is the speed of light.
The photonic density of states (PDOS) is another important factor in determining how the interaction between light and matter is modified inside a microcavity. Such property, which follows a quadratic law with energy in free space, is modified inside a DBR and a microcavity. Inside a DBR, the PDOS is drastically reduced in correspondence of the PBG neglecting the presence of propagating photons. A microcavity still creates the PDOS reduction in correspondence of the PBG but also creates a strong and sharp enhancement at the cavity mode energies. Such effect is exploited for PL enhancement as will be later seen in chapter 4.

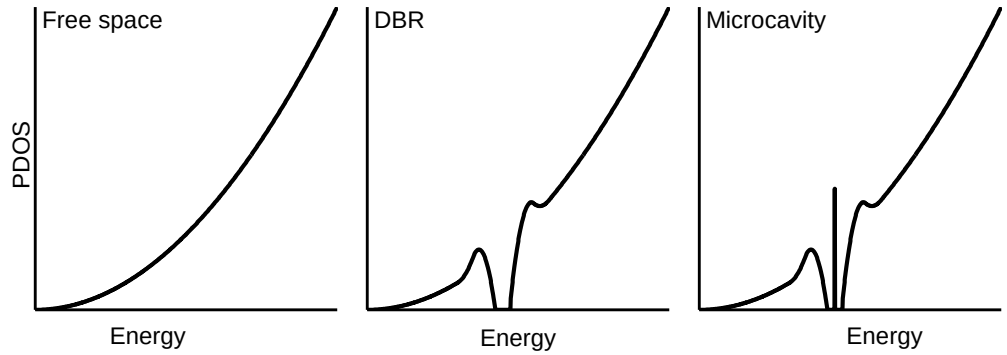

Fig. 1.10 Schematically drawing of the photonic density of states for free space, inside a DBR and inside a microcavity.

Polymer planar photonic crystals

To create a planar photonic crystal like a microcavity or a DBR, we basically need two or more materials having different refractive index. Commercial optical filters and devices are commonly created using transparent inorganic materials. From this point of view, inorganics supply a broad range of refractive indexes. Many oxides can be found with indexes ranging from 1.5 for silicon oxide to over 2.5 for titanium oxide.[31] Conversely, in polymers, as is also reported in Chapter 2, the refractive index always assume a value of about 1.5 and never get extremely high or extremely low. Due to this, the optical performances of polymer DBRs and microcavities are usually considered lower than those of their inorganics counterpart that can allow to reach larger dielectric contrasts. Fig. 1.11 shows the simulated optical response of two DBRs composed by 20 layers and centered at the same wavelength. The black spectrum has been calculated considering a DBR made of SiO_2 and TiO_2 while the red one is calculated considering a DBR of Poly(n-vinylcarbazole) (PVK) and cellulose acetate (CA), one of the most used polymer pairs for DBRs. The reflectance of the inorganic DBR is higher and its PBG is wider. Such performances are not achievable with polymers at the current state of the art, even if some work on very high refractive index and low refractive index polymers or nanocomposites is going on.[32-34]

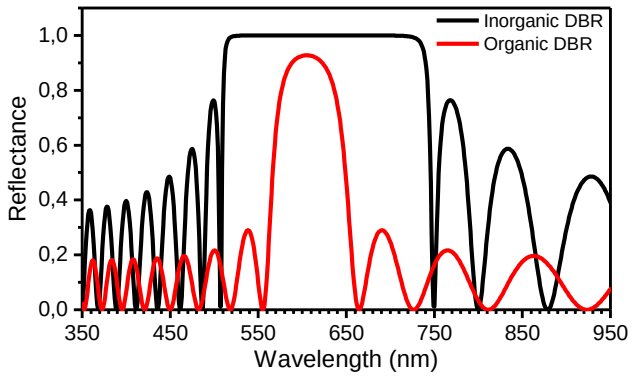

Fig. 1.11 Simulated reflectance of two DBRs composed by the same number of layers and the same central wavelength. The black line is the spectrum calculated considering the typical SiO_2/TiO_2 refractive indexes while the red line report the spectrum calculated considering the typical indexes of CA/PVK.

The limitations induced by the small polymers dielectric contrast may however be reduced. In particular, the reflectivity of polymer DBRs can be increased by spinning a large number of layers, according to eq. 1.3. Structure composed by hundreds of layers have been reported also in this thesis. The polymer processability is indeed higher than that of the common inorganic transparent materials used for PhCs and allows to obtain very flat layers having extremely reduced roughness as will also be shown in chapter 2. The PBG width of a DBR is directly proportional to the dielectric contrast and cannot be changed in any other way. Therefore, polymer DBRs PBG is unavoidably narrower than that of inorganic counterparts. This limits their use as broad band mirrors but may be and advantage in some applications like sensing.

Moreover, polymer DBRs offer an innate flexibility due to peculiar mechanical properties of the used materials.

The real main advantage of using polymers, however, comes from the production techniques. Roll-to-roll coating, co-extrusion and other solution processing techniques permit to obtain large area PhCs in a very cost-efficient way.[35-39] The manufacture of large area polymer planar photonic structures has indeed become a suitable task and some companies are currently commercializing products made of commonly found polymers like PET.[16] Fig. 1.12 shows a demonstrative picture used by Toray in its website. In the picture, the company exposes a semi-reflective sheet thought for automotive. The product is composed by 1000 layers of polymer and is sold in square meters. This is a clear example of the potential given by polymers for multilayer planar photonic devices. The possibility to scale up the production is really tangible and technology is already present on the market.

Fig. 1.12 Picasus, a multilayer planar photonic structure produced and commercialized by Toray. Image taken from the company informative web-site.[16]

Given the possibilities offered by these manufacture techniques, it is now possible to understand the reasons behind the interest on polymer planar PhCs.
In this thesis, all the work presented is based on spin coating. This technique, described in chapter 2, does not provide much scalability and, more than everything, is very expensive from a material point of view. Indeed, only a very small fraction of the original material which composes the used solutions is actually deposited on a device (no more than some percent) with a huge waste of polymers. Nonetheless, spin coating is a terrific technique to be used in a laboratory environment. It is fast, requires cheap equipment, and it is also very versatile.
With all these premises, we then report some of the major results obtained during the work for the author's PhD degree. Such results are not meant to propose fully working solutions but are instead focused on the proposition of proof-of-concept devices for which there are already present the technologies to provide production scale-up.

References

(1) Yablonovitch, E., Inhibited spontaneous emission in solid-state physics and electronics. *Physical Review Letters* **1987,** *58*, 2059-2062.
(2) Joannopulos, J. D.; Meade, R. D.; Win, J. N., *Photonic Crystals: Molding the Flow of the Light*. Princeton University Press: Princeton, 1995.
(3) Lova, P. Polymer Distributed Bragg Reflectors for Label-free Vapor Sensing. PhD Thesis, Nanyang Technological University, Singapore, 2017.
(4) Lova, P.; Bastianini, C.; Giusto, P.; Patrini, M.; Rizzo, P.; Guerra, G.; Iodice, M.; Soci, C.; Comoretto, D., Label-Free Vapor Selectivity in Poly(p-Phenylene Oxide) Photonic Crystal Sensors. *ACS Appl. Mater. Interfaces* **2016,** *8*, 31941-31950.
(5) Knarr III, R. J.; Manfredi, G.; Martinelli, E.; Pannocchia, M.; Repetto, D.; Mennucci, C.; Solano, I.; Canepa, M.; Buatier de Mongeot, F.; Galli, G.; Comoretto, D., In-plane Anisotropic Photoresponse in All-polymer Planar Microcavities. *Polymer* **2016,** *84*, 383-390
(6) Ryan, H.; Maria, C. Photonic Polymer Multilayers for Colorimetric Radiation Sensing. US20160252625, 2016.
(7) Cassagneau, T.; Caruso, F., Conjugated polymer inverse opals for potentiometric biosensing. *Adv. Mater.* **2002,** *14*, 1837-1841.
(8) Chan, E. P.; Walish, J. J.; Thomas, E. L.; Stafford, C. M., Block Copolymer Photonic Gel for Mechanochromic Sensing. *Adv. Mater.* **2011,** *23*, 4702-4706.
(9) Guan, X.-Y.; Leem, J. W.; Lee, S. H.; Jang, H.-J.; Kim, J.-H.; Hann, S.; Yu, J. S., Broadband high-reflective distributed Bragg reflectors based on amorphous silicon films for semiconductor laser facet coatings. *Applied Optics* **2015,** *54*, 1027-1031.
(10) Xue, C.; Zhao, J.; Wu, Y.; Yu, H.; Yang, S.; Wang, L.; Zhao, W.; Wu, Q.; Zhu, Z.; Liu, B.; Zhang, X.; Zhou, W.; Tai, R., Fabrication of large-area high-aspect-ratio periodic nanostructures on various substrates by soft X-ray interference lithography. *Applied Surface Science* **2017,** *425*, 553-557.
(11) Li, K.; Li, J.; Reardon, C.; Schuster, C. S.; Wang, Y.; Triggs, G. J.; Damnik, N.; Müenchenberger, J.; Wang, X.; Martins, E. R.; Krauss, T. F., High speed e-beam writing for large area photonic nanostructures — a choice of parameters. *Sci. Rep.* **2016,** *6*, 32945.
(12) Comoretto, D., *Organic and Hybrid Photonic Crystals*. 1 ed.; Springer International Publishing: Switzerland, 2015; p 497.
(13) Photonics 21 presentation page. http://www.photonics21.org/ (accessed 2017/10/13).
(14) Synchronics presentation page. http://synchronics-etn.eu/ (accessed 2017/10/13).
(15) Singer, K. D.; Kazmierczak, T.; Lott, J.; Song, H.; Wu, Y.; Andrews, J.; Baer, E.; Hiltner, A.; Weder, C., Melt-processed all-polymer distributed Bragg reflector laser. *Opt. Express* **2008,** *16*, 10358-10363.
(16) Toray Picasus Product Presentation. http://www.toray.com/products/films/fil_012.html (accessed 2017/10/13).
(17) Skorobogatiy, M.; Yang, J., *Fundamentals of Photonic Crystal Guiding*. Cambridge University Press: 2009.
(18) Teyssier, J.; Saenko, S. V.; van der Marel, D.; Milinkovitch, M. C., Photonic crystals cause active colour change in chameleons. **2015,** *6*, 6368.
(19) Zhang, S.; Chen, Y., Nanofabrication and coloration study of artificial Morpho butterfly

wings with aligned lamellae layers. **2015,** *5*, 16637.
(20) Vigneron, J. P.; Simonis, P., Natural photonic crystals. *Physica B: Condensed Matter* **2012,** *407*, 4032-4036.
(21) Makino, T., Transfer Matrix Method with Applications to Distributed Feedback Optical Devices. *Progress In Electromagnetics Research* **1995,** *10*, 271-319.
(22) Bajoni, D. Optical Spectroscopy Of Photonic Crystals And Microcavities. PhD thesis, Università di Pavia, 2003.
(23) Lova, P.; Grande, V.; Manfredi, G.; Patrini, M.; Herbst, S.; Würthner, F.; Comoretto, D., All-Polymer Photonic Microcavities Doped with Perylene Bisimide J-Aggregates. *Adv. Opt. Mater.*, DOI: 10.1002/adom.201700523.
(24) Manfredi, G.; Lova, P.; Di Stasio, F.; Krahne, R.; Comoretto, D., Directional Fluorescence Spectral Narrowing in All-Polymer Microcavities Doped with CdSe/CdS Dot-in-Rod Nanocrystals. *ACS Photonics* **2017,** *4*, 1761-1769.
(25) Gérard, J.-M.; Gayral, B., Strong Purcell Effect for InAs Quantum Boxes in Three-Dimensional Solid-State Microcavities. *J. Lightw. Technol.* **1999,** *17*, 2089-2095.
(26) Baba, T.; Sano, D., Low-Threshold Lasing and Purcell Effect in Microdisk Lasers at Room Temperature. *IEEE J. Sel. Topics Quantum Electron* **2003,** *9*, 1340-1346.
(27) Savona, V.; Andreani, L. C.; Schwendimann, P.; Quattropani, A., Quantum well excitons in semiconductor microcavities: Unified treatment of weak and strong coupling regimes. *Solid State Communications* **1995,** *93*, 733-739.
(28) Tischler, J. R.; Bradley, M. S.; Bulovic, V.; Song, J. H.; Nurmikko, A., Strong Coupling in a Microcavity LED. *Physical Review Letters* **2005,** *95*, 036401.
(29) Sumioka, K.; Nagahama, H.; Tsutsui, T., Strong coupling of exciton and photon modes in photonic crystal infiltrated with organic–inorganic layered perovskite. *Appl. Phys. Lett.* **2001,** *78*, 3.
(30) Schouwinka, P.; Berlepschb, H. v.; Dahnec, L.; Mahrt, R. F., Dependence of Rabi-splitting on the spatial position of the optically active layer in organic microcavities in the strong coupling regime. *Chemical Physics* **2002,** *285*, 113.
(31) Polyanskiy, M. Refractive index databse. http://refractiveindex.info (accessed 2017/10/17).
(32) Gazzo, S.; Manfredi, G.; Poetzsch, R.; Wei, Q.; Alloisio, M.; Voit, B.; Comoretto, D., High refractive index hyperbranched polyvinylsulfides for planar one-dimensional all-polymer photonic crystals. *J. Polym. Sci. Part B Polym. Phys.* **2016,** *54*, 73-80.
(33) Higashihara, T.; Ueda, M., Recent Progress in High Refractive Index Polymers. *Macromolecules* **2015,** *48*, 1915-1929.
(34) Wicht, G.; Ferrini, R.; Schüttel, S.; Zuppiroli, L., Nanoporous Films with Low Refractive Index for Large-Surface Broad-Band Anti-Reflection Coatings. *Macromolecular Materials and Engineering* **2010,** *295*, 628-636.
(35) Andrews, J. H.; Crescimanno, M.; Dawson, N. J.; Mao, G.; Petrus, J. B.; Singer, K. D.; Baer, E.; Song, H., Folding flexible co-extruded all-polymer multilayer distributed feedback films to control lasing. *Opt. Express* **2012,** *20*, 15580-15588.
(36) Song, H.; Singer, K.; Lott, J.; Wu, Y.; Zhou, J.; Andrews, J.; Baer, E.; Hiltner, A.; Weder, C., Continuous Melt Processing of All-polymer Distributed Feedback Lasers. *J. Mater. Chem.* **2009,** *19*, 7520-7524.

(37) Weber, M. F.; Stover, C. A.; Gilbert, L. R.; Nevitt, T. J.; Ouderkirk, A. J., Giant Birefringent Optics in Multilayer Polymer Mirrors. *Science* **2000,** *287*, 2451.
(38) Lee, T.-W.; Park, O. O.; Cho, H. N.; Kim, D. Y.; Kim, Y. C., Low-threshold lasing in a microcavity of fluorene-based liquid-crystalline polymer blends. *J. Appl. Phys.* **2003,** *93*, 1367-1370.
(39) L. Hou, Q. H., Y. Mo, J. Peng, and Y. Cao, All-organic Flexible Polymer Microcavity Light-emitting Diodes using 3M Reflective Multilayer Polymer Mirrors. *Appl. Phys. Lett.* **2005,** *87*, 243504.

Chapter II

Spin coating of planar photonic crystals

Spin coating is a reliable and highly reproducible technique used to create films of materials starting by colloidal dispersions or polymer solutions. The technique is conceptually very simple. A solution containing the material to be deposited (for example a polymer or nanoparticles dispersed in a suitable solvent) is dropped over a planar substrate in order to fully cover it. The substrate is then accelerated to a defined rotational speed using a spin coater. In the immediate beginning of the process, most of the material is expelled from the substrate by the centrifugal force while the remaining material forms a film that progressively thins due to solvent evaporation.

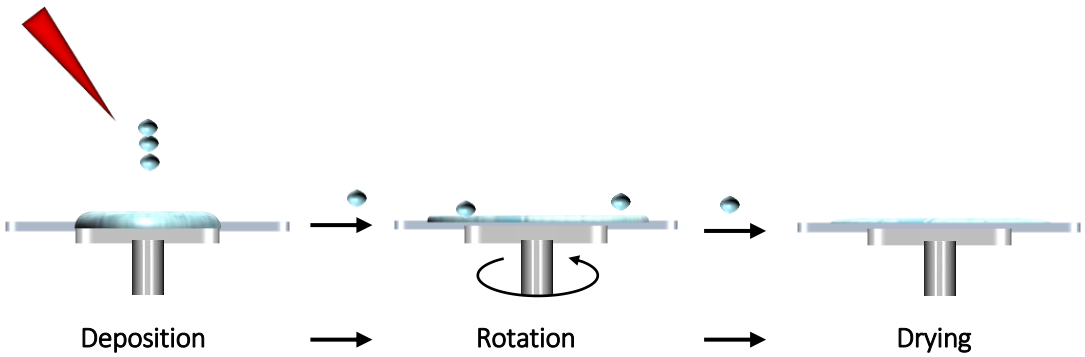

Fig. 2.1 Main steps during spin coating. First a solution or dispersion containing the material to be deposited in dropped over the substrate. Afterward, the substrate is put in rotation and the solvent evaporates leaving a smooth homogeneous solute film.

The technique is very flexible, fast and requires cheap equipment. Moreover it does not generally require specialized workers or optimizations to make single films, for example to create photoresists for lithography in electronics.[1-2] The possibility to create both polymer and inorganic films through solution and sol-gel processing is interesting too.[3-4]
To obtain films with different thicknesses, lot of parameter can be changed: the solvent employed, the concentration of the material in the used solution or suspension, the spin speed, the spinning time (if the rotation is stopped before complete drying is reached), or the environment conditions like temperature or humidity. This great number of parameters, however, may lead to very low reproducibility and to difficulties in the process if the environment is not kept under strict control.

Spin coating parameters

In spin coating, the main parameter to consider is the rotational speed of the substrate, which directly influences the radial force that is applied to the liquid solution and modifies the air turbulence created in proximity of the substrate. Generally, a spin coated film thickness depends upon the maximum speed reached during the procedure as a delicate balance is created between the shear force at the borders of the fluid and the evaporation rate. Higher speeds determine lower thicknesses.

The spin coater environment and the solvent properties strongly influence the solvent evaporation rate during spin coating. The presence of particularly ventilated air or the heating of the sample can drastically rise the evaporation rate and change spin coating mechanics. Moreover, humidity in presence of highly volatile solvents may create breathing figures on the surface of the grown films.[5]

It is difficult to provide a rigorous mathematical model to describe the processes happening during spin coating because of their complexity and a complete description of the technique would require knowledge of fluid dynamics, physics, thermodynamics, chemistry, and the precise value of a large number of parameters influencing the outcome of the process.[1-2, 6-19] Many theoretical works tried to investigate the spin coating process but no definitive and precise laws linking every physical parameter have been obtained. It is possible however to find general rule of thumbs that are followed by every spin coating process. In particular, except some deviations for ultrathin films,[18] as the spin speed increases, the grown films thickness decreases by a power law[7, 20-22]

$$t = \beta\omega^{-\alpha} \tag{2.1}$$

Where β is a constant, and ω is the spin speed. α is an exponent that depends on many details of the process but is usually ~0.5.[20, 23]

Also, the spinning solutions concentration is an extremely powerful tool to tune the properties of the grown films. Indeed, the concentration modifies the solutions viscosity and changes the film final thickness as well as the porosity. It is generally accepted the existence of a dependence of the form

$$t = \beta' c^n \omega^{-\alpha} \tag{2.2}$$

Where c is the solution concentration and n is an exponent which value is discussed in literature. In particular, it has been proposed that n is 1, giving a linear relation between thickness and concentration,[24] or greater than 1.[25]

One important step is the cleaning of the substrate. Operating in a sufficiently dust-free environment is essential since micron sized particles on the substrate can create inhomogeneities on the spin coated films, like comets or striations. These defects become more important during the growth of multilayer structures because they tend to have an effect also on the layers grown above and become quite deleterious on the final result.

The solvent choice is important both in the growth of single films and in the growth of multilayer structures. Indeed, the solvent determines the evaporation rate, as well as the surface tension created between the fluid and the substrate, modifying the films final

morphology. Sometimes, surfactants may be added to the spin coating solution to prevent aggregation or to favour substrate wettability and adhesion.
Moreover, the pair solvent-solute interacts with the substrate. Notably, in the fabrication of polymer multilayers and DBRs where different materials are directly deposited one over each other, the solvent of the polymer which is being spin coated must not dissolve the layers underneath. This condition is called solvents orthogonality and it is the basic requisite to obtain high optical quality planar photonic crystals. This is usually obtained working with polar and non-polar polymer pairs like polystyrene/Cellulose Acetate or polyvinylcarbazole/Cellulose Acetate.[26-27]

Polymer DBRs by spin coating

DBRs are formed by casting alternated layers of different materials. One can use spin coating to grow such structures by creating each new layer directly above the previous ones. However, it is required the process to be highly repeat-able. Moreover, also a control of the grown layers thickness is desirable as this last parameter governs the optical response of a DBR and allows to tune the response of a sample.
In this chapter we report the results of polymer spin coating in order to supply a way to repeat-ably create optical multilayer structures using the most common commercial polymers, i.e. poly(N-vinylcarbazole) (PVK) as high index material and cellulose acetate (CA) and polyacrylic acid (PAA) as low refractive index materials.
These three materials are commonly used in literature. PVK is a standard for high index material because few process-able polymers with high dielectric constant are known.[37-38]
PAA and CA, instead, permit to achieve high dielectric contrast if used together with PVK,[34, 39-40] which is important for DBRs.[41] Moreover, one can use PAA and CA in solvents which are orthogonal to PVK.
We investigate the relation of spin coating parameters with the thickness of the grown layers and their roughness. We also provide the refractive index of the polymers in order to supply parameters for optical structures design. Spin coating, AFM analysis, profilometries, and ellipsometries were conducted in the Dresden integrated center for applied physics and photonic materials.
The spin coating was conducted using a BLE Laboratory Equipment GmbH DELTA 10 close chamber spin coater starting from 1”x1” glass or silicon substrates. The polymer solutions were deposited over the substrate in order to fully cover it and then the sample has been put in rotation. The rotation has been held for 300 s.
After spin coating, all the samples underwent thermal treatment on a heating plate at 140°C for 1 minute.
The solvents used to spin coat CA, PAA and PVK were diaceton alcohol, 2-methyl-2-butanol and chlorobenzene, respectively.
AFM measures were recorded using a AIST-NT Combiscope 1000 in tapping mode. Analysis of films surface roughness was conducted on 2x2 μm^2 topographic maps using the software Gwyddion.[33]
Ellipsometries were executed using an Accurion Nanofilm EP4 ellipsometer and modeling of the measures was conducted through the software EP4Model. The sample analyzed

through ellipsometry were single films grown on silicon substrates.
Determination of films thickness was executed using a Veeco Dektak 150 profilometer. Each film has been carefully scratched to expose the glass substrate underneath and measure the difference in height between the substrate and the film top surface.

Spin coating of cellulose acetate

CA is a low refractive index material. It can be easily spin coated creating solutions in diaceton alcohol. Fig. 2.2 reports the refractive index of a CA film obtained using ellipsometry. The data has been interpreted using a Sell-Maier model. The refractive index value goes from 1.484 at 400 nm to 1.463 at 800 nm and the extinction coefficient is considered negligible. This very low and almost constant index justifies why CA is often chosen to create polymer DBRs.[31-32, 34-35, 39, 42]

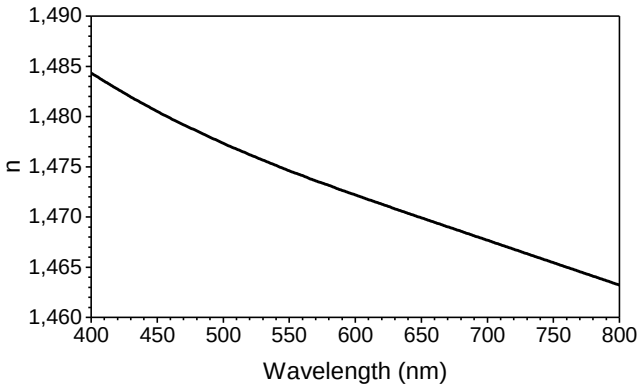

Fig. 2.2 Refractive index n of CA films as deduced by ellipsometry using a Sell-Maier model.

Fig. 2.3 shows a topographic map of the surface of a CA film before and after thermal treatment. There is a change in roughness due to thermal annealing; the surface roughness (rms) reduces from 2.2 ± 0.3 nm to 1.8 ± 0.3 nm. Thermal treatment also influences layer thickness. Indeed, in all the measures, after annealing, each film shrinks of about 6% in thickness, probably due to residual solvent evaporation.

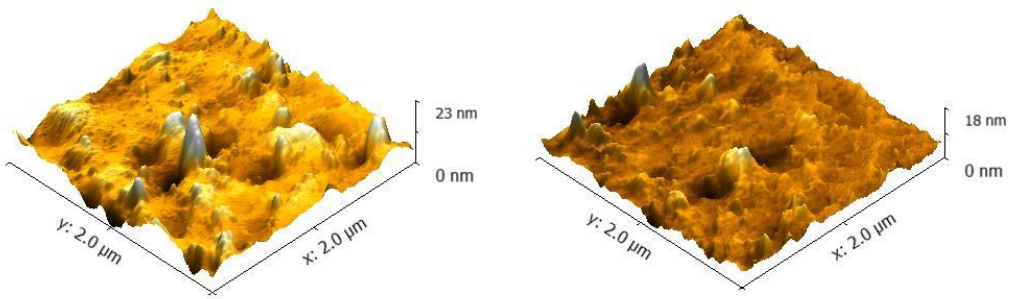

Fig. 2.3 AFM topographic map of spin coated Cellulose Acetate film. On the left, before thermal treament. On the right, after thermal treatment.

Fig. 2.4a shows the thickness of CA films spin coated over PVK after thermal annealing. The thickness is reported as a function of the concentration of the starting solutions. The behavior is clearly linear in concentration and the red lines inside the plot indicate the fitted response for each spin speed. The x-intercept and slope of these fitted curves are reported in Table 2.1 and in Fig. 2.4b against rotation speed. The x-intercepts of the fit assume constant values around 14-15 g/l. This value represents the minimum concentration below which the thickness would be negative using these linear models. The existence of this limit suggests that the linear model loses sense for lower concentrations or a minimum concentration is needed in order to create films by spin coating. The latter hypothesis is also sustained by previous spin coating experience but has not been systematically investigated. The slope of the fits in Fig. 2.4 decays monotonically with spin speed as would be expected by eq. 2.1.

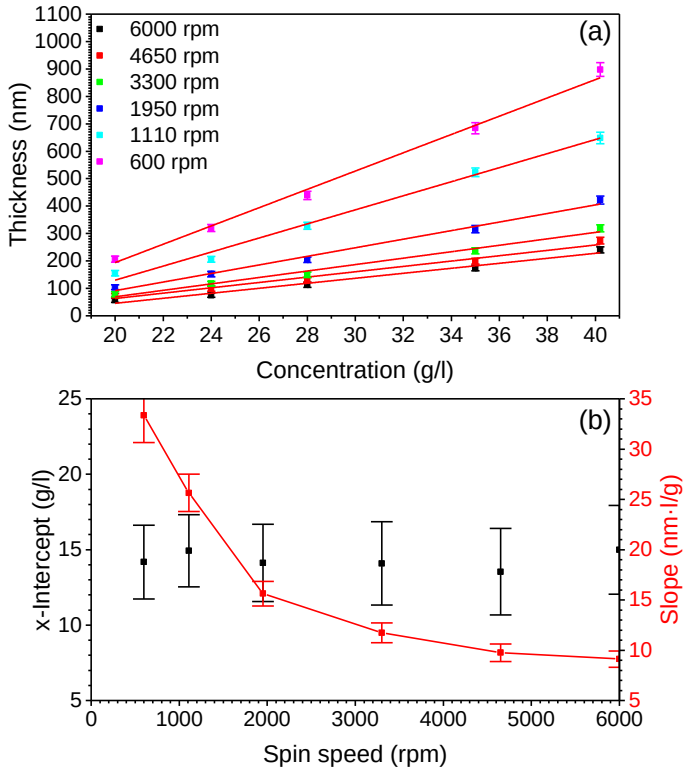

Fig. 2.4 (a) CA film thickness vs solution concentration for each spinning speed. In solid red lines are the linear fits (b) Parameters of the linear fits as a function of spin speed.

Table 2.1 Linear fit parameters of the thickness of CA films spin coated over PVK as a function of concentration for each spin speed

Spin speed (rpm)	x-Intercept (g/l)	Slope (nm·l/g)
6000	15 ± 3	9.1 ± 0.8
4650	14 ± 3	9.8 ± 0.9
3300	14 ± 3	12 ± 1
1950	14 ± 3	16 ± 1
1110	15 ± 2	26 ± 2
600	14 ± 2	33 ± 3

Fig. 2.5a reports the thickness of the same CA films of Fig. 2.4 but this time against the rotation speed. For each starting solution concentration, the data can be fitted using a power law function of the form of eq. 2.1 as suggested by literature.[1-2, 17, 19] The power exponent obtained by the fit is 0.59 ± 0.01, reasonably near the exponent of 0.5 proposed in literature.[6-7, 43] Its deviation toward higher values can be justified by a non-complete drying during the spin coating process.[6] This hypothesis is sustained also by the reduction of thickness after thermal annealing. The β parameter of the fit is reported in Fig. 2.5b. It grows linearly with concentration of the starting solution and intercept the x-axis at 13 ± 1 g/l, in agreement with the x-intercepts found with linear fits reported in Table 2.1.

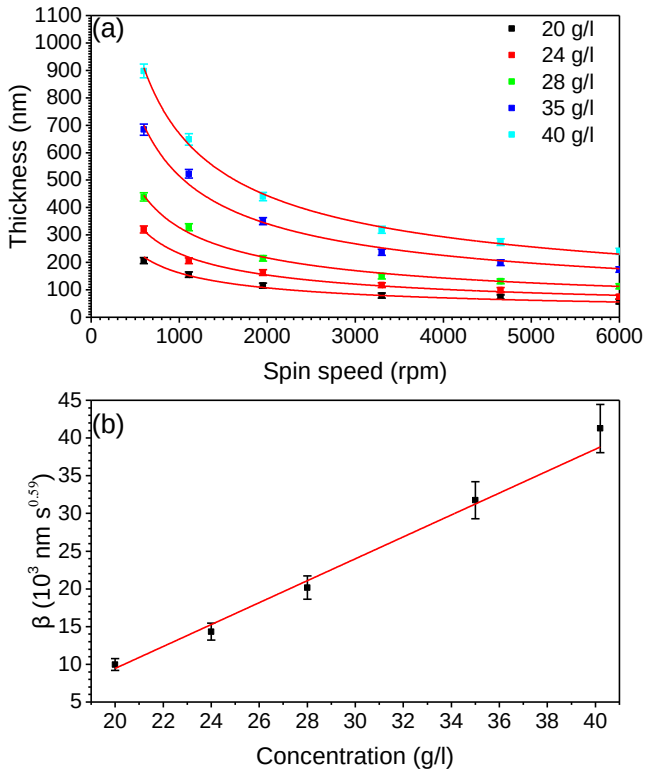

Fig. 2.5 (a) Thickness of CA films created by spin coating over PVK as a function of spin speed. In red the allometric fit for every concentration (b) Parameters of the allometric fits as concentration function.

Spin coating of Polyacrylic acid

PAA is a polar low refractive index polymer and can be spin coated starting from 2-methyl-2-butanol solutions. We measured the refractive index of PAA films using ellipsometry and a Sellmeier model. Its value is reported in Fig. 2.6 and goes from 1.525 at 400 nm to 1.508 at 800 nm while extinction coefficient is negligible in the investigated spectral range.

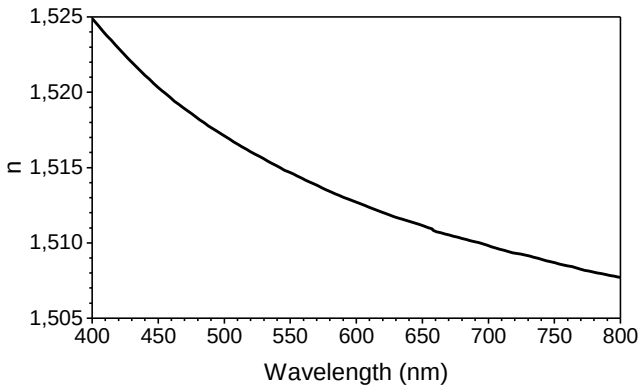

Fig. 2.6 Refractive index n of PAA films as deduced by ellipsometry using a Sell-Maier model.

Indeed, the refractive index of PAA is higher than the CA one. This could be counterproductive in producing DBRs as would grant a lower dielectric contrast. However, the use of PAA instead of CA is interesting as PAA can be dissolved in less viscous solutions which are easier to spin coat and, among the other things, permit to obtain smoother layers and better interfaces.[29, 42, 44] AFM measures (Fig. 2.7 reports the example of a film before and after thermal treatment) of PAA films show a surface roughness of 0.13 ± 0.02 nm which is near the limit of resolution of the instrument. It is not possible to measure differences in roughness after thermal treatment, however PAA films thickness reduces by 16 ± 5% after the annealing.

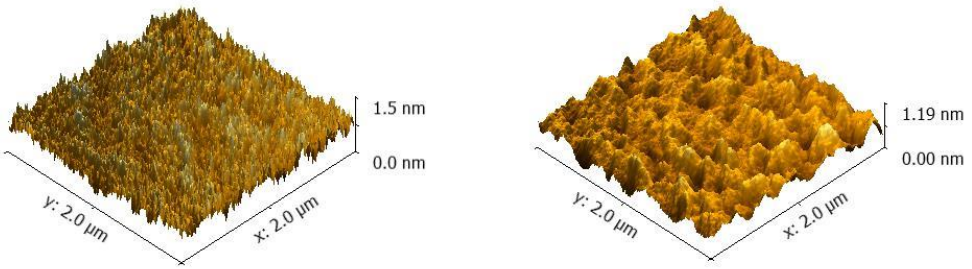

Fig. 2.7 AFM topographic map of spin coated PAA film. On the left, before thermal treament. On the right, after thermal treatment.

Fig. 2.8a shows the thickness of spin coated and annealed PAA films against the concentration of the starting solutions. As in the case of CA, there is a clear linear relationship between the final thickness of the films and the solution concentration used to spin coat. The red lines indicate the fitted results. The x-intercept and slope of the fitted curves are reported in and in Fig. 2.8b versus the spin speed. As in the case of CA, the x-intercepts assume a constant value, this time of 6 ± 2 g/l. The slope still follows a monotonic decreasing behavior.

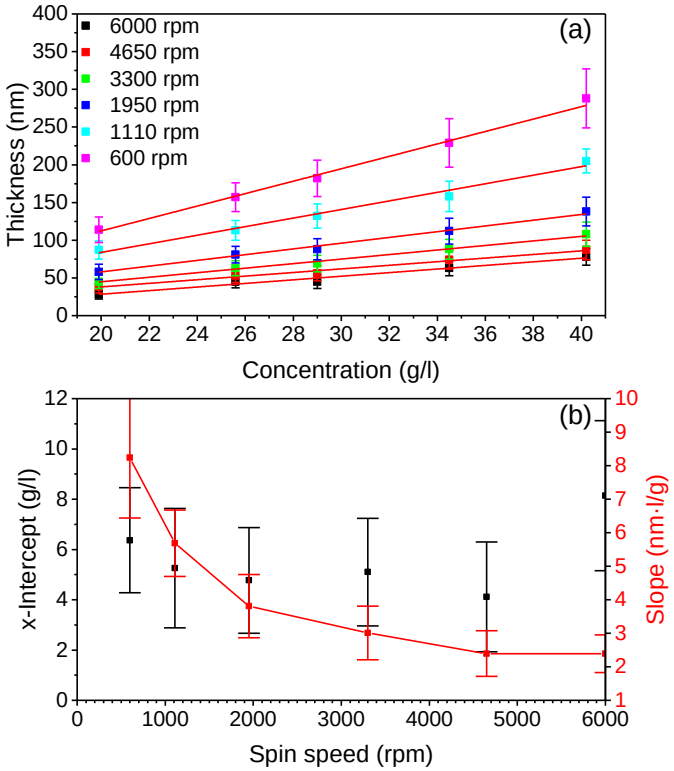

Fig. 2.8 (a) PAA film thickness vs solution concentration for each spinning speed. In solid red lines are the linear fits (b) Parameters of the linear fits as a function of spin speed.

Table 2.2 Linear fit parameters of the thickness of PAA films spin coated over PVK as a function of concentration for each spin speed.

Spin speed (rpm)	x-Intercept (g/l)	Slope (nm·l/g)
6000	8 ± 3	2.4 ± 0.5
4650	4 ± 2	2.4 ± 0.7
3300	5 ± 2	3.0 ± 0.8
1950	5 ± 2	3.8 ± 0.9
1110	5 ± 2	6 ± 1
600	6 ± 2	8 ± 2

Fig. 2.9a reports the thickness of spin coated and annealed PAA films versus the rotation speed. Again, as in the case of CA films, for each starting solution concentration, the data can be fitted using a power law function like the one in eq. 2.1. We obtained an exponent of 0.570 ± 0.001, in agreement with literature, as reported for CA. The obtained k values are instead reported in Fig. 2.9b as a function of concentration. The parameter linearly grows and has an x-intercept of 5.4 ± 0.6 g/l in agreement with the intercepts previously found.

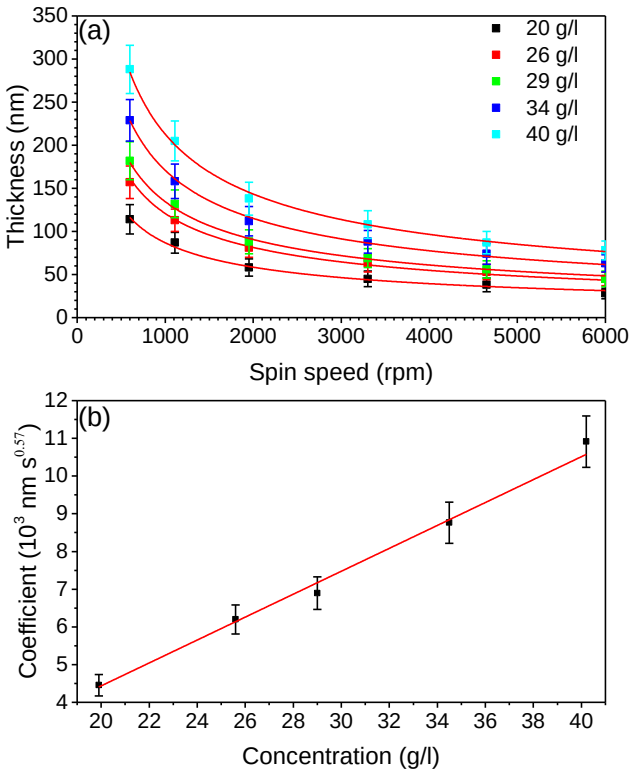

Fig. 2.9 (a) Thickness of PAA films created by spin coating over PVK as a function of spin speed. In red the allometric fit for every concentration (b) Multiplicative coefficient of the allometric fits as concentration function.

Spin coating of Poly(N-vinylcarbazole)

PVK is generally used for LEDs as a transport layer or as emitting material blended with other molecules.[45-48] Since it can form excimers, it presents feeble absorption and emission in the violet part of the visible spectra.[48-49] However, due to the weakness of these effects, PVK can be considered transparent for optical applications and many works shows DBRs and microcavities made using PVK. Indeed, the proximity of the absorbing transition grants the material a high refractive index.[34, 39, 42] Considering only the visible part of the EM spectrum, it's possible to interpret the ellipsometric measures of PVK using a Sellmeier model for the refractive index. Fig. 2.10 shows the results of ellipsometry of PVK films. The index varies from 1.75 at 400 nm to 1.65 at 800 nm. Together with CA, then, it can grant an

index contrast greater than 0.2.

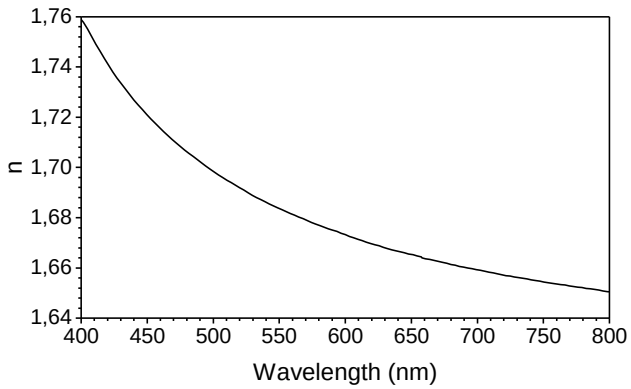

Fig. 2.10 Refractive index n of PVK films as deduced by ellipsometry using a Sellmeier model.

Fig. 2.11 Reports two AFM measures before and after thermal treating PVK films. They show a very small roughness of 0.21 ± 0.09 nm which remain substantially unaltered after the treatment (0.18 ± 0.03 nm). Moreover, the annealing process doesn't show any significant effect on films thickness.

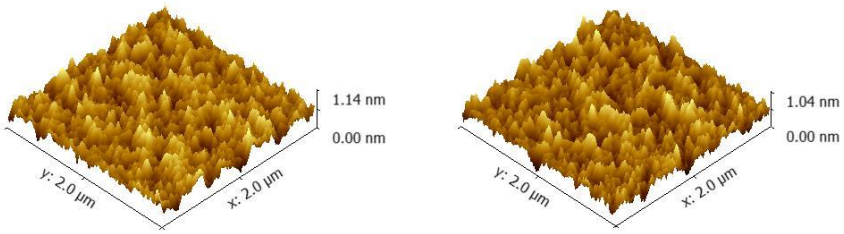

Fig. 2.11 AFM topographic map of spin coated PVK film. On the left, before thermal treament. On the right, after thermal treatment.

PVK films may be growth over different substrates depending upon the low refractive index material we are using to create DBRs. We then studied the thickness of PVK films spin coating on both CA and PAA in order to look at the differences induced by the substrate.
Fig. 2.12a shows the thickness of annealed PVK films spin coated over PAA. A linear behavior is clearly distinguishable. The data has been fitted and the results are reported in red. The fit parameters are reported in Table. 2.3 and in Fig. 2.12b as a function of solution concentrations. As in the previous cases, the fitted lines show x-intercepts that are constant (7.9 ± 0.9 g/l). The slope instead has a monotonic decreasing trend.

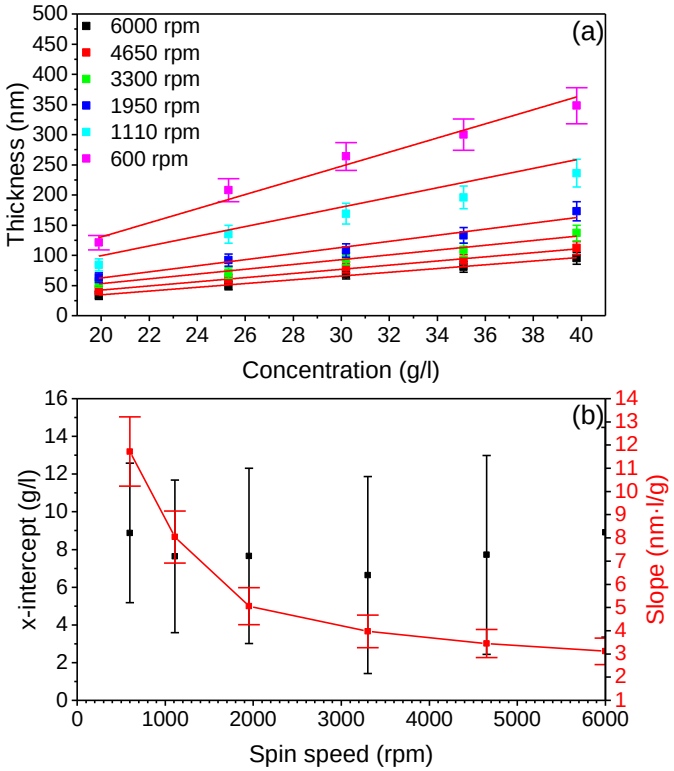

Fig. 2.12 (a) Thickness of PVK films created by spin coating over PAA as a function of concentration. In red the linear fit for every spin speed (b) Parameters of the linear fits as a function of the spin speed.

Table. 2.3 Linear fit parameters of the thickness of PVK films spin coated over PAA as a function of concentration for each spin speed

Spin speed (rpm)	x-Intercept (g/l)	Slope (nm·l/g)
6000	9 ± 6	3.1 ± 0.6
4650	8 ± 5	3.4 ± 0.6
3300	7 ± 5	4.0 ± 0.7
1950	8 ± 5	5.1 ± 0.8
1110	8 ± 4	8 ± 1
600	9 ± 4	12 ± 1

Fig. 2.13 reports the thickness of annealed PVK films spin coated over PAA against the rotation speed. Even in this case, the thickness decreases with rotation speed and can be fitted using a power law function. The fit gives us an exponent is 0.54 ± 0.01. Differently from the case of CA and PAA, the value is nearer to 0.5. Such difference may be due to the higher volatility of the polymer solvent. Indeed, a higher volatility favors evaporation and film drying, assuring a more complete volume reduction of the spin coated films. Fig. 2.13b

shows the k coefficient extracted by fits in function of solution concentration. Its value linearly grows and intercept the x-axis at 8.5 ± 0.6 g/l.

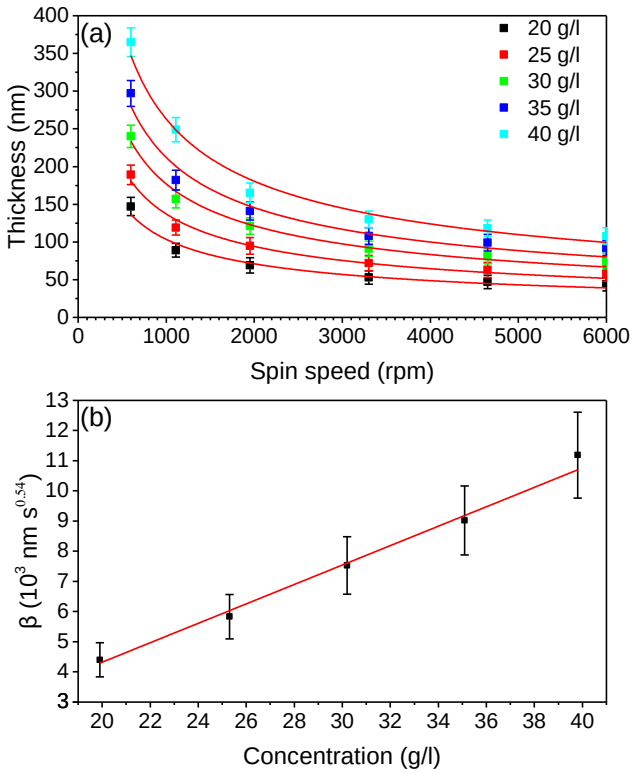

Fig. 2.13 (a) Thickness of PVK films created by spin coating over PAA as a function of spin speed. In red the allometric fit for every concentration (b) Multiplicative coefficient of the allometric fits as a function of the spin speed.

We have conducted analogous measures spin coating PVK over CA. Fig. 2.14a shows the thickness of such films as function of solution concentration. As in the case of spin coating over PAA, the thickness is linear with solution concentration. The x-intercept and slope obtained fitting the data (in red) are reported in Table 2.4 and in Fig. 2.14b as functions of spin speed. The x-intercepts assume a constant value (7 ± 1 g/l).

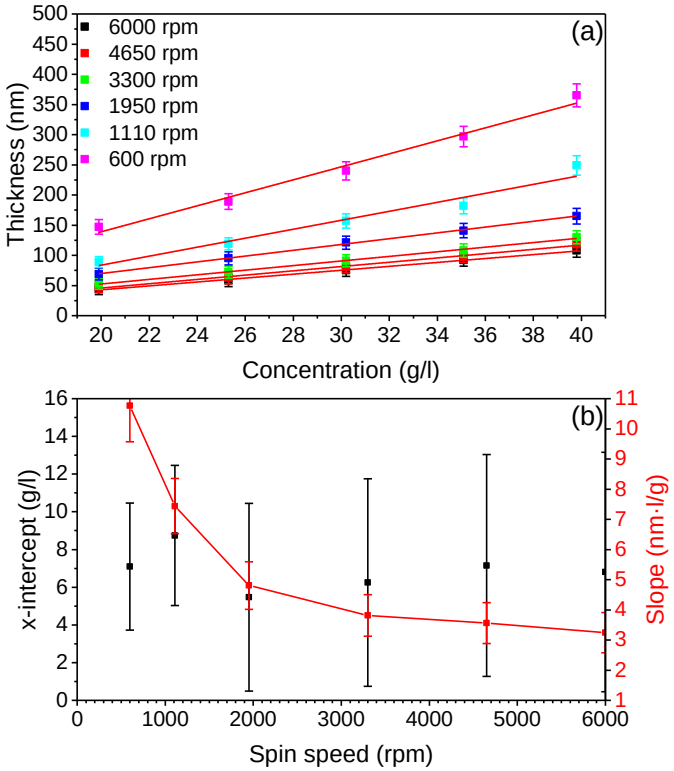

Fig. 2.14 (a) Thickness of PVK films created by spin coating over CA as a function of concentration. In red the linear fit for every spin speed (b) Parameters of the linear fits as a function of the spin speed.

Table 2.4 Linear fit parameters of the thickness of PVK films spin coated over CA as a function of concentration for each spin speed

Spin speed (rpm)	x-Intercept (g/l)	Slope (nm·l/g)
6000	7 ± 6	3.2 ± 0.7
4650	7 ± 6	3.6 ± 0.7
3300	6 ± 6	3.8 ± 0.7
1950	5 ± 5	4.8 ± 0.8
1110	9 ± 4	7.4 ± 0.9
600	7 ± 3	11 ± 1

Fig. 2.15a reports the thickness of annealed PVK films spin coated over CA versus the spin speed. Fitting again to a function of the form of eq. 2.1, we obtain an α exponent of 0.54 ± 0.02, the same value found for spin coating over PAA. The k coefficient, instead, is still linear but has a different growing slope. Its value is reported in Fig. 2.15b as a function of concentration. The x-intercept is 6.6 ± 0.6 g/l, in accordance with the one found before.

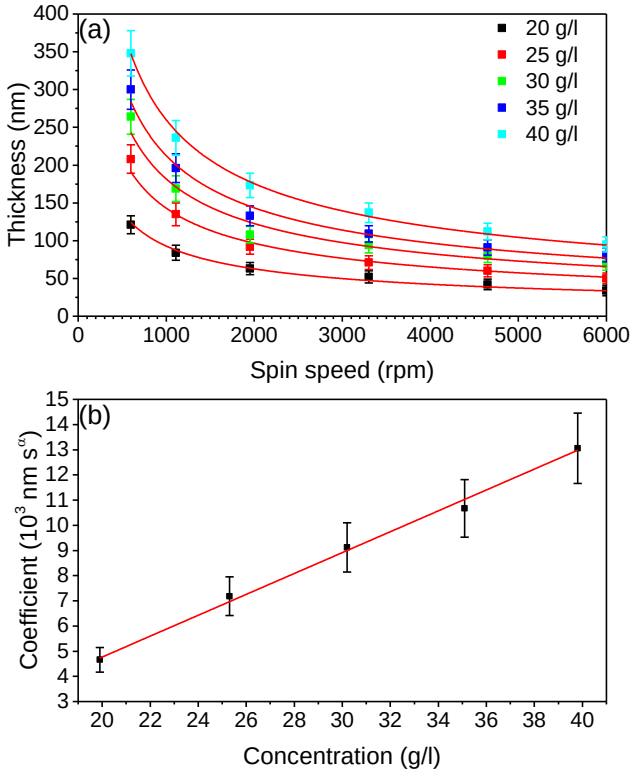

Fig. 2.15 (a) Thickness of PVK films created by spin coating over PAA as a function of spin speed. In red the allometric fit for every concentration (b) Multiplicative coefficient of the allometric fits as a function of the spin speed.

Spin coating PVK over CA and PAA revealed differences in the thickness of the grown film. In particular, no difference is observed in the exponent of the power law governing the thickness. However, a difference exists in the slope of the coefficient β. The only difference introduced between the two cases is the different substrate and, to our knowledge, few works are dedicated to the influence of the substrate on the spin coating process.[14] It seems to take a role only in changing the linear coefficient linking the solution concentration to the final thickness and is not involved in the power exponent which is instead more related to the evaporation process. This makes an interesting subject to further investigation.
For all the materials used we see that the thickness of the obtained layers follows a power law function with spin speed where the multiplicative coefficient β is linear with concentration. Then, for all the cases under investigation, we can relate the obtained film thickness t to spin parameters by:

$$t = m(c - c_0)\omega^{-\alpha} \tag{2.3}$$

Where c_0 is the x-intercept of the multiplicative coefficient, m its growth slope, and α is the fitted power exponent. The three parameters depend on the polymer/solvent pair used while m and c_0 also depends on the spin coating substrate. Table 2.5 summarizes all the

obtained results.

Table 2.5 Surface roughness and spin coating parameters obtained for each material studied in this work

Material	**Solvent**	**Substrate**	**Roughness (nm)**	**C_0 (g/l)**	**M (nm s^{α})**	**α**
CA	DAA	PVK	1.8 ± 0.3	13 ± 1	1453 ± 95	0.59 ± 0.01
PAA	2-methyl-2-butanol	PVK	0.13 ± 0.02	5.4 ± 0.6	304 ± 14	0.570 ± 0.001
PVK	Chlorobenzene	PAA	0.21 ± 0.09	8.5 ± 0.6	415 ± 15	0.54 ± 0.01
PVK		CA		6.6 ± 0.6	322 ± 17	0.54 ± 0.02

References

(1) Toshio, Y.; Taro, M.; Masaru, A.; Mitsumasa, U., Thin-Film Formation by Spin Coating: Characteristics of a Positive Photoresist. *Jpn. J. Appl. Phys.* **1995,** *34*, 6279.
(2) Meyerhofer, D., Characteristics of resist films produced by spinning. *J. Appl. Phys.* **1978,** *49*, 3993-3997.
(3) Jiang, K.; Zakutayev, A.; Stowers, J.; Anderson, M. D.; Tate, J.; McIntyre, D. H.; Johnson, D. C.; Keszler, D. A., Low-temperature, solution processing of TiO2 thin films and fabrication of multilayer dielectric optical elements. *Solid State Sciences* **2009,** *11*, 1692-1699.
(4) Fardad, M. A.; Mishechkin, O. V.; Fallahi, M., Hybrid sol-gel materials for integration of optoelectronic components. *J. Lightw. Technol.* **2001,** *19*, 84-91.
(5) Bolognesi, A.; Mercogliano, C.; Yunus, S.; Civardi, M.; Comoretto, D.; Turturro, A., Self-organization of polystyrenes into ordered microstructured films and their replication by soft lithography. *Langmuir* **2005,** *21*, 3480.
(6) Norrman, K.; Ghanbari-Siahkali, A.; Larsen, N. B., 6 Studies of spin-coated polymer films. *Annual Reports Section "C" (Physical Chemistry)* **2005,** *101*, 174-201.
(7) Lawrence, C. J., The mechanics of spin coating of polymer films. *Physics of Fluids (1958-1988)* **1988,** *31*, 2786-2795.
(8) Temple-Boyer, P.; Mazenq, L.; Doucet, J. B.; Conédéra, V.; Torbiéro, B.; Launay, J., Theoretical studies of the spin coating process for the deposition of polymer-based Maxwellian liquids. *Microelectronic Engineering* **2010,** *87*, 163-166.
(9) Strawhecker, K. E.; Kumar, S. K.; Douglas, J. F.; Karim, A., The Critical Role of Solvent Evaporation on the Roughness of Spin-Cast Polymer Films. *Macromolecules* **2001,** *34*, 4669-4672.
(10) Norrman, K.; Ghanbari-Siahkali, A.; Larsen, N. B., 6 Studies of spin-coated polymer films. *Annual Reports Section "C" (Physical Chemistry)* **2005,** *101*, 174.
(11) Münch, A.; Please, C. P.; Wagner, B., Spin coating of an evaporating polymer solution. *Physics of Fluids* **2011,** *23*, 102101.
(12) Iii, D. P. B.; Kaz, D. M.; Taylor, D. J., Surface tension evolution during early stages of drying of sol–gel coatings. *J Sol-Gel Sci Technol* **2008,** *49*, 233-237.
(13) Haas, D. E.; Iii, D. P. B., Evaluation of thermocapillary driving forces in the development of striations during the spin coating process. *Journal of Materials Science* **2002,** *37*, 2109-2116.
(14) Cheung, K. P.; Grover, R.; Wang, Y.; Gurkovich, C.; Wang, G.; Scheinbeim, J., Substrate effect on the thickness of spin-coated ultrathin polymer film. *Appl. Phys. Lett.* **2005,** *87*, 214103.
(15) Skrobis, K. J.; Denton, D. D.; Skrobis, A. V., Effect of early solvent evaporation on the mechanism of the spin-coating of polymeric solutions. *Polym. Eng. Sci.* **1990,** *30*, 193-196.
(16) Washo, B. D., Rheology and Modeling of the Spin Coating Process. *IBM Journal of Research and Development* **1977,** *21*, 190-198.
(17) Extrand, C. W., Spin coating of very thin polymer films. *Polym. Eng. Sci.* **1994,** *34*, 390-394.
(18) Hall, D. B.; Underhill, P.; Torkelson, J. M., Spin coating of thin and ultrathin polymer films. *Polym. Eng. Sci.* **1998,** *38*, 2039-2045.
(19) Emslie, A. G.; Bonner, F. T.; Peck, L. G., Flow of a Viscous Liquid on a Rotating Disk. *J.*

Appl. Phys. **1958,** *29*, 858-862.
(20) Chang, C.-C.; Pai, C.-L.; Chen, W.-C.; Jenekhe, S. A., Spin coating of conjugated polymers for electronic and optoelectronic applications. *Thin Solid Films* **2005,** *479*, 254-260.
(21) Yimsiri, P.; Mackley, M. R., Spin and dip coating of light-emitting polymer solutions: Matching experiment with modelling. *Chem. Eng. Sci.* **2006,** *61*, 3496-3505.
(22) *Organic and Hybrid Photonic Crystals*. Springer International Publishing: Switzerland, 2015.
(23) Norrman, K.; Ghanbari-Siahkali, A.; Larsen, N. B., Studies of spin-coated polymer films. *Annu. Rep. Prog. Chem., Sect. C: Phys. Chem.* **2005,** *101*, 174-201.
(24) Lima, J. P. H.; de Andrade, A. M., Morphological analysis of poly(o-methoxyaniline) thin-films deposited by spin coating technique. *Journal of Materials Science: Materials in Electronics* **2006,** *17*, 593-596.
(25) Walsh, C. B.; Franses, E. I., Ultrathin PMMA films spin-coated from toluene solutions. *Thin Solid Films* **2003,** *429*, 71-76.
(26) Frezza, L.; Patrini, M.; Liscidini, M.; Comoretto, D., Directional Enhancement of Spontaneous Emission in Polymer Flexible Microcavities. *J. Phys. Chem. C* **2011,** *115*, 19939-19946.
(27) Canazza, G.; Scotognella, F.; Lanzani, G.; Silvestri, S. D.; Zavelani-Rossi, M.; Comoretto, D., Lasing from all-polymer microcavities. *Laser Phys. Lett.* **2014,** *11*.
(28) K. Unger, R. R., C. Czibula, C. Ganser, C. Teichert, G. Jakopic, G. Canazza, S. Gazzo, D. Comoretto In *Distributed Bragg reflectors: Morphology of cellulose acetate and polystyrene multilayer*, 16th International Conference on Transparent Optical Networks (ICTON), Graz (AUT), 6-10 July 2014; IEEE Xplore Digital Library: Graz (AUT), 2014; p Th.B4.5.
(29) Tippo, T.; Thanachayanont, C.; Muthitamongkol, P.; Junin, C.; Hietschold, M.; Thanachayanont, A., The effects of solvents on the properties of ultra-thin poly (methyl methacrylate) films prepared by spin coating. *Thin Solid Films* **2013,** *546*, 180-184.
(30) Komikado, T.; Inoue, A.; Masuda, K.; Ando, T.; Umegaki, S., Multi-layered mirrors fabricated by spin-coating organic polymers. *Thin Solid Films* **2007,** *515*, 3887-3892.
(31) Komikado, T.; Inoue, A.; Masuda, K.; Ando, T.; Umegaki, S., Multi-layered mirrors fabricated by spin-coating organic polymers. *Thin Solid Films* **2007,** *515*, 3887-3892.
(32) Álvarez, A. L.; Tito, J.; Vaello, M. B.; Velásquez, P.; Mallavia, R.; Sánchez-López, M. M.; Fernández de Ávila, S., Polymeric multilayers for integration into photonic devices. *Thin Solid Films* **2003,** *433*, 277-280.
(33) Lova, P.; Bastianini, C.; Giusto, P.; Patrini, M.; Rizzo, P.; Guerra, G.; Iodice, M.; Soci, C.; Comoretto, D., Label-Free Vapor Selectivity in Poly(p-Phenylene Oxide) Photonic Crystal Sensors. *ACS Applied Materials & Interfaces* **2016,** *8*, 31941-31950.
(34) Manfredi, G.; Lova, P.; Di Stasio, F.; Krahne, R.; Comoretto, D., Directional Fluorescence Spectral Narrowing in All-Polymer Microcavities Doped with CdSe/CdS Dot-in-Rod Nanocrystals. *ACS Photonics* **2017,** *4*, 1761-1769.
(35) Lova, P.; Manfredi, G.; Boarino, L.; Comite, A.; Laus, M.; Patrini, M.; Marabelli, F.; Soci, C.; Comoretto, D., Polymer Distributed Bragg Reflectors for Vapor Sensing. *ACS Photonics* **2015,** *2*, 537-543.
(36) Lova, P.; Manfredi, G.; Boarino, L.; Comite, A.; Laus, M.; Patrini, M.; Marabelli, F.; Soci, C.; Comoretto, D., Hybrid Nanocomposite for 1D Photonic Crystals as Simple Colorimetric

Sensor. *ACS Photonics* **2015,** *2*, 537-543.
(37) Gazzo, S.; Manfredi, G.; Pötzsch, R.; Wei, Q.; Alloisio, M.; Voit, B.; Comoretto, D., High refractive index hyperbranched polyvinylsulfides for planar one-dimensional all-polymer photonic crystals. *Journal of Polymer Science Part B: Polymer Physics* **2016,** *54*, 73-80.
(38) Higashihara, T.; Ueda, M., Recent Progress in High Refractive Index Polymers. *Macromolecules* **2015,** *48*, 1915-1929.
(39) Menon, V. M.; Luberto, M.; Valappil, N. V.; Chatterjee, S., Lasing from InGaP quantum dots in a spin-coated flexible microcavity. *Opt. Express* **2008,** *16*, 19535-19540.
(40) Canazza, G.; Scotognella, F.; Lanzani, G.; Silvestri, S. D.; Zavelani-Rossi, M.; Comoretto, D., Lasing from all-polymer microcavities. *Laser Phys Lett* **2014,** *11*, 035804.
(41) Skorobogatiy, M.; Yang, J., Fundamentals of Photonic Crystal Guiding. *Fundamentals of Photonic Crystal Guiding* **2009**, 1-267.
(42) Valappil, N. V.; Luberto, M.; Menon, V. M.; Zeylikovich, I.; Gayen, T. K.; Franco, J.; Das, B. B.; Alfano, R. R., Solution processed microcavity structures with embedded quantum dots. *Photonics and Nanostructures - Fundamentals and Applications* **2007,** *5*, 184-188.
(43) Tyona, M. D., A theoritical study on spin coating technique. *Advances in materials Research* **2013,** *2*, 195-208.
(44) Lova, P.; Grande, V.; Manfredi, G.; Patrini, M.; Herbst, S.; Würthner, F.; Comoretto, D., All-Polymer Photonic Microcavities Doped with Perylene Bisimide J-Aggregates. *Advanced Optical Materials* **Accepted**.
(45) Rezvani, M.; Farajollahi, F.; Nikfarjam, A.; Bakhtiarpour, P.; Saydanzad, E., Effect of Solvents, Their Mixture and Thermal Annealing on the Performance of Solution Processed Polymer Light-Emitting Diodes. *Materials* **2013,** *6*, 1994-2006.
(46) Patel, S.; Ramrakhiani, M.; Bisen, D. P., Photophysical studies of polyvinylcarbazole polymer films. *Journal of Applied Polymer Science* **2007,** *104*, 722-726.
(47) Lin, H.-C.; Tsai, C.-M.; Lin, J.-T. s.; Thomas, K. R. J., Novel red and white PLED devices consisting of PVK blended with blue-emitting fluorene derivatives and carbazole dopants. *Synthetic Metals* **2006,** *156*, 1155-1160.
(48) Johnson, G. E., Emission properties of vinylcarbazole polymers. *J. Phys. Chem.* **1975,** *62*, 4697.
(49) Lee, J. S.; Kim, C. H.; Yu, J. W.; Kim, J. K.; Kim, D. Y.; Song, N. W.; Kim, C. Y., Competition between the formation of excimers and excitons during the photoluminescence of light-emitting polymer blends. *J. Polym. Sci. A Polym. Chem.* **2004,** *42*, 557-565.

Chapter III

Sensing with polymer planar photonic crystals

The stunning growth of goods production and the development of industries all over the world are releasing an increasing amount of harmful chemicals into the atmosphere, the water sources, and the soil. A special category of pollutants is represented by volatile organic compounds (VOC) which can be problematic for humans and are a serious environmental harm. This category includes all the organic compounds having boiling point included in the range 0-400 °C and can be further divided into subclasses:

- very volatile compounds ($T_{eb} < 50$ °C)
- volatile compounds (50 °C $< T_{eb} < 240 - 280$ °C)
- semi-volatile ($240 - 280$ °C $< T_{eb} < 380 - 400$ °C).

The category of VOCs contains a great number of substances including very common solvents like acetone, which is suspected to create neurological damages, or tetrachloroethylene, which is often used in dry cleaning and is a suspected carcinogenic agent.[1-2]

The presence of VOCs in indoor environment can cause sick building syndrome,[3] characterized by eye and respiratory irritation, headaches, loss of coordination and nausea.[4] The long-term exposure, instead, can damage liver, kidneys and the central nervous system. It also seems to exist a link between VOCs and the development of cancer.[5]

The reaction of VOCs with oxygen sources like nitrogen oxides and carbon monoxides contributes to the formation of tropospheric ozone.[6] Ozone, in addition to being a greenhouse gas and impacting on global warming,[7] is a powerful oxidizing agent. Hence it causes respiratory illness[8] and can easily react to form new toxic chemical species.[9]

The presence of VOCs is not only related to the release by industrial processes but also to common activities performed in urban areas. Indeed, VOCs can be found in products used for painting works, dry cleaning, or refrigerators. They are also produced in wood burning and are common compounds released by photocopy machines.[3-4, 10]

Since the compounds are so widespread and harmful, it is necessary to have reliable methods and devices to identify and monitor their presence in urban environments where often it is impossible to have clear hints about the nature of air pollutants. This uncertainty is indeed a great obstacle to the choice of the right treatments to operate in order to preserve people's health.

An ideal device for VOC detection in urban environment should be easy to use and easy to understand. It should also be easy to fabricate in order to be wide spread wherever is needed and selective in order to quickly decide the best treatments. In industrial environment, sensitivity and low detection limit are required to detect pollutants in low

concentrations (considering that for example benzene may be carcinogenic already at 1 ppm).
The established technologies can hardly fulfill all the requirements and research is still ongoing on these subjects.[11]
Polymer DBRs may be good candidates linking the presence of VOCs to a simple colorimetric response[12-13] and can be fabricated through techniques already used on industrial scale like co-extrusion.[14]
In this chapter, we report about the working mechanism of DBR sensors and propose a model to describe their optical response. We also report on the production of a cellulose ternary photonic crystal which could be used for polar vapor sensing. While the vast majority of the experimental part has been conducted by Dr. Paola Lova, the simulations and the model creation has been conducted by the PhD candidate Giovanni Manfredi (this thesis author). For what it concerns instead sensing using cellulose ternary photonic crystals, all the experimental part, the data analysis and the writing of the related paper was conducted by this thesis author in collaboration with Prof. Robert Schennach, Technical University Graz - Austria.

Working principles of planar photonic crystal sensors

As already explained in Chapter 1, PhCs present a strong optical response linked to the dimension of the periodic elements in the dielectric lattice and to the refractive index of the media composing the crystal. A change in any of these parameters influences the optical response. Then, it is possible to place a PhC in contact with an analyte that penetrates in the PhC and exploit the response of the media composing the system to study the analyte itself through optical techniques like VIS or IR spectroscopy. Although it is possible to study the whole optical response of a PhC,[15-16] often it is convenient to study just the PBG and its variation over time. The PBG is characterized by a peak of reflectance which is easily observable through visible spectroscopy or even with naked eye if the reflectivity is particularly intense. If observed in reflectivity or transmittance, the PBG is characterized by a spectral position λ_{PBG}, a width $\Delta\lambda_{PBG}$, and a maximum intensity R_{PBG} or T_{PBG}. In the case of DBRs, which are the system studied in this thesis, we recall that the first order PBG wavelength position λ_{PBG} follows the laws:[17]

$$\lambda_{PBG} = 4(d_H + d_L)\frac{n_H n_L \cos\theta_H \cos\theta_L}{n_H \cos\theta_H + n_L \cos\theta_L} \quad \text{TE polarization} \tag{3.1}$$

$$\lambda_{PBG} = 4\frac{d_H \cos^2\theta_H + d_L \cos^2\theta_L}{n_H \cos\theta_L + n_L \cos\theta_H} \quad \text{TM polarization} \tag{3.2}$$

Where n_H, d_H are the refractive index and thickness of the high index material and n_L, d_L are the refractive index and thickness of the low index material. $\theta_{H,L}$ are the light propagation angles inside the high and low index materials which can be derived by Snell law $n_i \sin\theta_i = n_j \sin\theta_j$. The reflectivity of the PBG is dependent upon the number of bi-layers composing the PhC and, if the system is in the $\lambda/4$ condition and the substrate has refractive index n_{sub}, one can apply the formula:[18]

$$R_{PBG} = 1 - \frac{4}{n_{sub}}\left(\frac{n_L}{n_H}\right)^N = 1 - \frac{4}{n_{sub}}\left(1 - \frac{\Delta n}{n_H}\right)^N \quad (3.3)$$

Which states that the maximum reflectivity increases with the increase of the number of bilayers N and increases for higher difference in the indexes of the materials composing the PhC (Δn).
The spectral width of the PBG in $\lambda/4$ condition, instead, is ruled by the law:

$$\Delta E_{PBG} = \frac{4E_{PBG}}{\pi}\frac{n_H - n_L}{n_H + n_L} = \frac{4E_{PBG}}{\pi}\frac{\Delta n}{2n_L + \Delta n} \quad (3.4)$$

Where ΔE_{PBG} is the spectral width of the PBG in energy and E_{PBG} is the energy of the first order PBG. This formula states that the band gap gets larger for higher difference in refractive index among the materials composing the PhC.
Eqs. 3.1-3.4, already reported in chapter 1 but recalled here, are pretty useful if we want to understand what happens when we change one of the parameters of the layers composing a DBR.
A change in layers thickness directly shifts the optical response of a DBR. An increase of the thickness mainly shifts the optical response toward the red while a decrease of layers thickness induces a blue-shift as shown in Fig. 3.1 for a calculated example DBR made by poly(N-vinylcarbazole) and cellulose acetate. The effect on PBG width and intensity is very modest and depends mainly on the change of spectral position which induce a narrowing in wavelength since the PBG width is constant in energy as described in eq. 3.4.

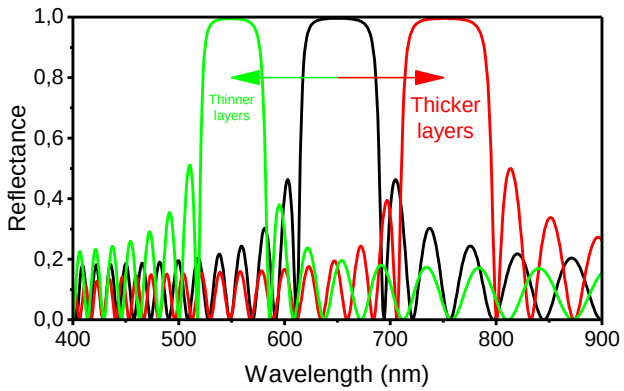

Fig. 3.1 Variation of PBG in an example DBR for a variation of layers thickness of about 30%.

A change in refractive index instead, modifies both the spectral position and the intensity and width of the PBG. In particular, if one of the two indexes increases, the PBG shifts toward longer wavelengths whereas it shifts toward shorter wavelengths if one of the two indexes decreases. The width and the intensity increase or decrease depending upon the new Δn induced by the modification of the index. The effect of modification of high

refractive index is shown in Fig. 3.2 for an example DBR completely similar to the one of Fig. 3.1.

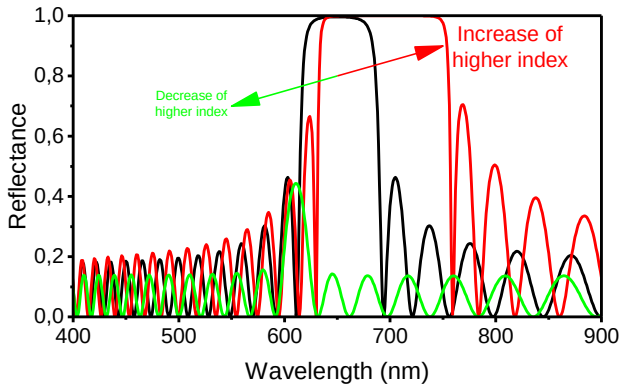

Fig. 3.2 Variation of PBG in an example DBR for a variation of higher index of about 10%.

If an analyte can diffuse inside a DBR, it can modify the PhC layers thickness or refractive index. The induced modifications can then be tracked using optical methods. However, it is interesting to quantify the magnitude of the changes in the optical response. Indeed, if we consider an analyte in liquid phase, the amount of material that can diffuse inside the DBR may be high and the modifications induced might be quite strong. In literature, DBR structures have been proposed for sensing of analytes in liquid phase.[19-21]
If we are interested in airborne VOC detection, however, the concentration of analyte might be much smaller compared to liquid phase. Hence, the amount of material that can diffuse and modify thicknesses or refractive indexes can be quite small and induce only slight modifications. To have a sensor for these compounds then, it is necessary to have a very high sensitivity of the materials to the analyte and a high porosity in order to favor diffusion and accumulation. In literature, DBRs of this kind have been proposed,[22-24] however they are affected by either low response time or high production complexity.

Polymer DBRs for sensing

Polymers and nanocomposite materials allows to obtain process-ability and favor diffusion of analytes at the same time. Moreover, they respond to common solvents swelling in a vigorous way. The thickness of a polymer layer may double in the presence of specific solvents in air. Due to these reasons, they can be used in DBRs for vapor phase solvent sensing.[13] Moreover, the use of specific polymers may grant selectivity to different analytes without using labels.[12]
As part of her PhD project, Dr. Paola Lova, in collaboration with us, worked on the production of polymer DBRs for vapor sensing. As a starting point, she worked on the implementation of polystyrene-ZnO nanoparticles nanocomposites in standard DBR to increase permeability to vapor analytes.[25] More specifically, the work studied the optical response modification induced by toluene vapor exposition. Pure PS/cellulose acetate DBRs were weakly sensible to toluene and their response times were very low. The use of a very porous nanocomposite speeds up the response and allows to achieve better results as

shown in Fig. 3.3.

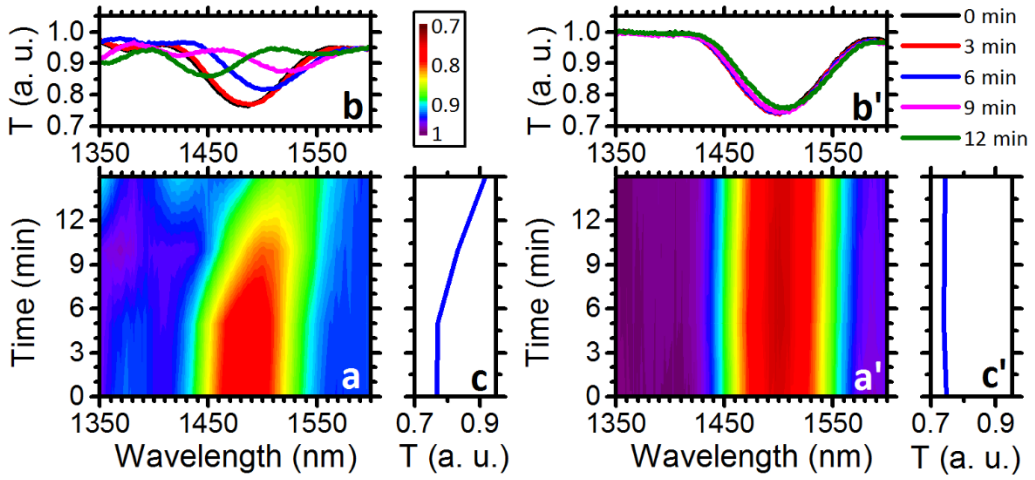

Fig. 3.3 Optical response to toluene vapor of DBR sensors. Nanocomposite DBR on the left and PS/CA DBR on the right. a), a') Contour plots of the transmittance spectra collected every 5 minutes; b), b') Corresponding transmittance spectra; c), c') Time dependent differential transmittance at the initial stop-band wavelength. Taken from Paola Lova's PhD thesis with her permission.

The response of the nanocomposite DBR to toluene vapor exposition has been studied for long time expositions and the transmittance over time is reported in Fig. 3.4 as a contour plot. On the x-axis is the wavelength and on the y-axis is the time in minutes. The transmittance is color coded from red (low transmittance) to blue (high transmittance). The PBG of the sample is visible in red as the low transmittance area. At the beginning is placed at about 1480 nm. As the time goes by, it first reduces in intensity and slightly redshifts. After about 15 minutes, the PBG is not visible anymore (labelled with * in Fig. 3.4) and then appears again at much longer wavelength (~1800 nm) after about 70 minutes (labelled with *' in Fig. 3.4). After this time, the PBG keeps red-shifting until it reaches a saturation point.

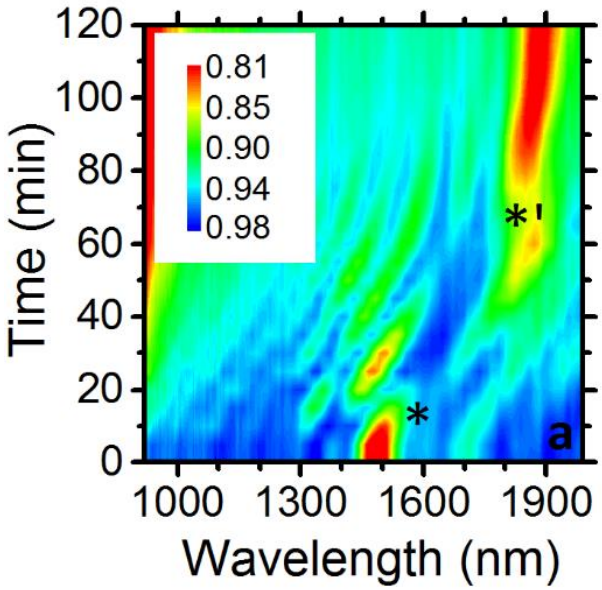

Fig. 3.4 Measured transmittance of a PS:nanocomposite/CA DBR exposed to toluene vapors. Taken from Paola Lova's PhD thesis with her permission.

This complicate behavior of the sample optical transmittance suggests that an inhomogeneous change of the properties of the layers composing the system occurs. Indeed, the disappearance of the PBG might be induced only by a worsening of the system periodicity which is the main responsible for photon propagation inhibition. In order to fully understand the modifications occurring during toluene exposure we tried then to model the response of a generic DBR exposed to some solvent vapors. The simulation, which has also been reported in the paper published,[13] has then be extended to describe the case of methanol penetration inside a PS/CA DBR which has a drastically different behavior.[26] In fact, as reported in Fig. 3.5, in this second case the PBG swells over time without disappearing and without changing drastically in intensity. This behavior suggests that the homogeneity of the layers composing the system is maintained over time and the periodicity never comes less.

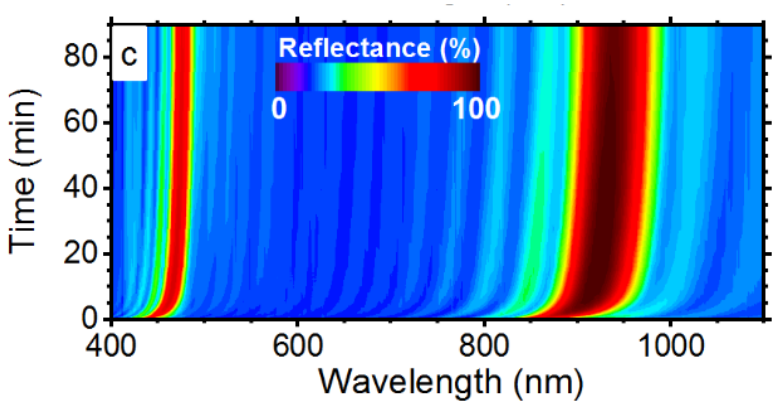

Fig. 3.5 Contour-plot of the temporal evolution of a PS/CA DBR reflectance spectra during methanol exposure. Taken from a paper in preparation[26] with the main author's permission.

Modeling of DBR response during solvent vapor exposure

To simulate the response of polymer DBRs during exposure to solvent vapors, we set-up a model accounting for the concentration of solvent in each layer of the system. To create the model, we need some hypothesis. First, we assume the penetration of the analyte inside the PhC is diffusion driven. It is then a gradient of concentration to supply the driving force of the process.

We also assume the solvent concentration in air is constant, meaning that an infinite source of solvent is placed in the environment but not directly in contact with the DBR.

We also assume that only one of the two materials composing the DBR responds to the solvent molecules. Indeed, in the case of PS:nanocomposite/CA exposed to toluene it is resonable toluene only modifies PS properties while in the case of PS/CA exposed to methanol, the only material responding to the alcohol should be CA. This is given by the fact that PS is soluble in apolar solvents and is resistant to polar solvents whereas CA is soluble in polar solvents and resistant to apolar solvents. It is worth to notice that this solvent orthogonality is a basic prerequisite to create DBRs by spin coating (chapter 2).[27]

If an orthogonal solvent penetrates inside the PhC, it forms a unique phase with the material it dissolves and does not affect the other one. This led us to consider one material as a solvent absorber and the other one as a barrier to solvent diffusion. Since a DBR is composed by parallel alternate layers, we can then define the system as a series of layers in contact one with the next. Each absorbing layer can retain a certain amount of solvent and work as a reservoir having a certain solvent concentration c_i. We must point out that doing so, we assumed the concentration profile of solvent inside each absorbing layer is uniform, meaning that the typical diffusion time inside the layer is much faster compared to the time needed to the solvent to diffuse from one layer to the next one. This assumption will be justified later on in this chapter. The situation is sketched in Fig. 3.6.

Finally, we assume that analyte flux occurs crossing surface of the sample thus neglecting uptake from the sides of the sample. This reasonable since the typical lateral area is orders of magnitude lower than the surface one.

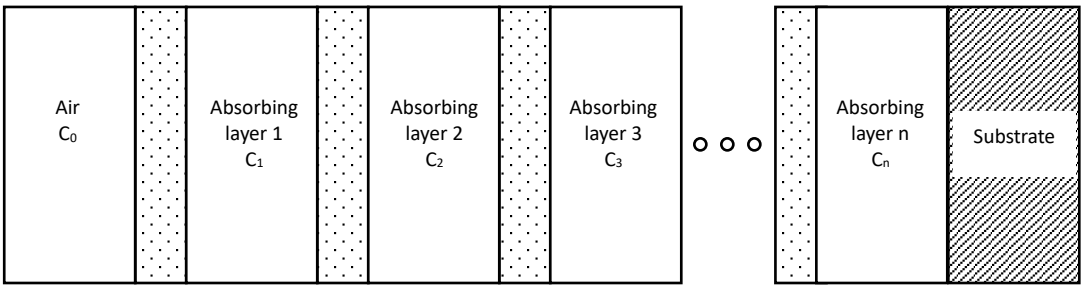

Fig. 3.6 Sketch of the model used to simulate DBR response to vapor exposure. The layers filled with dots are barrier layers.

In this model, the solvent can be exchanged by any i-th layer only with the adjacent ones (i±1). Since there's always a barrier between them, the solvent finds a resistance to diffusion and its flux from the layer i to the layer i+1 follows a Fick like law:

$$J_{i\to i+1} = P_{i,i+1}(c_i - c_{i+1}) \tag{3.5}$$

Where $P_{i,i+1}$ is a permeability constant depending upon the properties of the barrier layer (B_i) between two adjacent absorbing layers A_i, A_{i+1} and c_i, c_{i+1} are their solvent concentrations. We assume each $P_{i,i+1}$ is constant in time and not dependent on the layers solvent concentration. We also supposed, as a first approximation that the sorption coefficients are unitary. The sorption coefficient, which is basically defined as the concentration difference between two materials in equilibrium, may play a significant role in the exchange of material but we are not able to measure it with our instrumentation. We decided then to neglect it and try to get a qualitative modeling as an initial step to approach the problem. We point out that the permeation of vapors inside polymers is not a well investigated subject and a full analytical analysis is absolutely out of the scope of this work. To each A_i, we assign a certain volume V_i that changes with its solvent concentration. We assume the dependence to be linear:

$$V_i = V_i^0(1 + \alpha * c_i) \tag{3.6}$$

Where V_i^0 is the dry layer volume (before exposure) and α is a linear parameter which keeps into account only for a first order Taylor expansion of the real $V(c)$ dependence. This is a swelling factor depending on the amount of analyte there grabbed.
The area of the DBR surface, which is also the area of each layer, is bounded to the substrate dimension and does not change during the exposure to vapors. If we call this area A and the layers thickness h_i, we can write:

$$h_i = \frac{V_i}{A} = h_i^0(1 + \alpha * c_i) \tag{3.7}$$

Knowing the flux of solvent in and out of each absorbing layer and knowing its volume, we can write a mass balance equation:

$$\frac{dQ_i}{dt} = A * (J_{i-1\to i} - J_{i\to i+1}) \tag{3.8}$$

Where $Q_i(t)$ is the total amount of solvent inside the i^{th} layer at the time t. Since we know the layer volume and the amount of material inside it we can now write

$$c_i = \frac{Q_i}{V_i} \tag{3.9}$$

$$\frac{dc_i}{dt} = \frac{1}{V_i}\left(\frac{dQ_i}{dt} - \frac{Q_i}{V_i}\frac{dV_i}{dt}\right) = \frac{1}{V_i}\left(\frac{dQ_i}{dt} - c_i\frac{dV_i}{dt}\right) \tag{3.10}$$

Inserting eq. 3.6 inside eq. 3.10 and using some simple algebra, we obtain

$$\frac{dc_i}{dt} = \frac{dQ_i}{dt}\frac{1}{V_i}\left(1 + \alpha\frac{V_i^0}{V_i}c_i\right)^{-1} = \frac{\frac{dQ_i}{dt}}{V_i^0(1+2\alpha c_i)} \tag{3.11}$$

We can now insert eq. 3.8 in eq. 3.11 and, considering eq. 3.7, we get

$$\frac{dc_i}{dt} = \frac{J_{i-1\to i} - J_{i\to i+1}}{h_i^0(1+2\alpha c_i)} = \frac{P_{i-1,i}(c_{i+1} - c_i) - P_{i,i+1}(c_i - c_{i+1})}{h_i^0(1+2\alpha c_i)} \tag{3.12}$$

Which links the variation in concentration of solvent in the i^{th} layer to the concentration in the layers i-1 and i+1. Since the DBR is a periodic structure, the permeability $P_{i,i+1}$ must be equal among any pair of layers and we call it P_{DBR}. The only permeability that can be different is the one between the first layer and the air which we call P_{ext}. Moreover, the dry thickness h^0 and the first order swelling parameter α are the same for every layer. We can then write a system of equations

$$\begin{cases} \frac{dc_1}{dt} = \frac{P_{ext} * (c_0 - c_1) - P_{DBR}(c_1 - c_2)}{h^0(1+2\alpha c_1)} \\ \vdots \\ \frac{dc_i}{dt} = \frac{P_{DBR} * (c_{i-1} + c_{i+1} - 2c_i)}{h^0(1+2\alpha c_i)} \\ \vdots \\ \frac{dc_n}{dt} = \frac{P_{DBR} * (c_{n-1} - c_n)}{h^0(1+2\alpha c_n)} \end{cases} \tag{3.13}$$

Where we consider no diffusion through the substrate for the last layer n, being usually glass. This system of equations can be numerically solved using Euler's method and putting as bounding conditions:

$$c_i(0) = 0 \quad \text{for} \quad i = 1,2,\dots,n \tag{3.14}$$

Meaning that at the starting time the DBR is completely dry.
Having a system of equations able to provide $c_i(t)$, we can now find the thickness of each layer in the DBR using eq. 3.7. The evolution of layers thickness will be discussed ahead. However, now we need to make some further comments about the used model.

Diffusion in single layers

As already stated in the previous paragraph, we supposed that the diffusion of solvent inside a single layer is much faster than the diffusion through one soluble layer and the next one. To evaluate the consistency of this assumption, we must address the problem of diffusion inside a single layer and see if the time needed for the solvent to assume a constant concentration inside a single layer is much smaller than the time needed for the overall system to swell.
Let us then suppose that a small amount of solvent can penetrate inside a layer and diffuse inside it with creating only a negligible swelling. Since we supposed that the intralayer diffusion is very small, we can approximate the two sides of the layer as non-permeable barriers. We can now calculate how much time the solvent takes to obtain a homogeneous concentration inside the layer. This can be done finding an analytical solution to the problem following the approach proposed by Crank.[28]
We limit ourselves to the one-dimensional diffusion along x-axis. In this case, Fick's second law takes the form of eq. 3.15 and one of its possible solutions in a homogeneous media is reported in eq. 3.16.

$$\frac{\partial \mathrm{C}}{\partial \mathrm{t}} = \mathrm{D}\frac{\partial^2 \mathrm{C}}{\partial \mathrm{x}^2} \tag{3.15}$$

$$\mathrm{C} = \frac{\mathrm{M}}{\sqrt{\pi \mathrm{D}\mathrm{t}}} \mathrm{e}^{-\frac{\mathrm{x}^2}{4\mathrm{D}\mathrm{t}}} \tag{3.16}$$

Here D is the diffusion coefficient and M is constant which defines the total amount of material solved in the system.
The function, considered only for x>0, represents the spreading of a material inside a semi-infinite slab if it is initially concentrated in an infinitesimal thickness layer placed at x=0. Since eq. 3.16 has null first order derivative, the solution is also suitable if an impermeable barrier is at x=0 as it implies no mass transport at that position. If we want to consider a layer of thickness h where no mass transfer can occur at the borders, we can put a second impermeable barrier at x=h. The new solution then, must have null first order derivative also at x=h. To find a solution of this kind, we can exploit the linearity of eq. 3.15 and just add to eq. 3.16 a specular solution which mimics the reflection of the solvent by the barrier at x=L.

$$\mathrm{C} = \frac{\mathrm{M}}{\sqrt{\pi \mathrm{D}\mathrm{t}}} \left(\mathrm{e}^{-\frac{\mathrm{x}^2}{4\mathrm{D}\mathrm{t}}} + \mathrm{e}^{-\frac{(2\mathrm{h}-\mathrm{x})^2}{4\mathrm{D}\mathrm{t}}} \right) \tag{3.17}$$

The new function in eq. 3.17 is now compatible with a barrier at x=L but not compatible with a barrier at x=0. In order to account for both, then, it is necessary to sum infinite reflections, finally obtaining

$$C = \frac{M}{\sqrt{\pi D t}}\left\{ e^{-\frac{x^2}{4Dt}} + \sum_{n=1}^{\infty}\left[e^{-\frac{(x+2nh)^2}{4Dt}} + e^{-\frac{(2nh-x)^2}{4Dt}} \right]\right\} = \frac{M}{\sqrt{\pi D t}} \sum_{n=-\infty}^{\infty} e^{-\frac{(x+2nh)^2}{4Dt}} \quad (3.18)$$

The function of eq. 3.18, obviously, is valid in the interval 0<x<h and its integral is equal to the integral from -∞ to +∞ of 3.16, which is M. We have then obtained the right equation to describe the diffusion of solvent inside a flat layer of thickness h which is infiltrated at time t=0 by an amount M of material.

In this chapter, we report two main cases of polymer DBR solvent exposure: PS/CA DBR exposed to toluene vapors and PS/CA DBR exposed to methanol vapors. If we examine the case of methanol exposure, we can find in literature that the methanol diffusivity in CA is $D=2.5*10^{-8}$ cm^2/s.[29] Moreover, we know from optical simulations on the sample DBR that each CA layer is 167 nm thick when dry and becomes 185 nm at the end of exposure with a swelling of about 11%. As self-consistency proof then, we can limit ourselves to the case of a fully swelled layer, suppose the solvent can't swell the layer anymore and account for the time the solvent takes to reach a uniform concentration. Fig. 3.7 reports the solvent concentration profile inside a single polymer layer for different times calculated using the parameters just reported. The calculation has been done considering a total amount M_t of methanol and approximating for 11 terms in the sum of eq. 3.18. For short times, the methanol is more concentrated at the beginning of the layer. As the time goes by, it diffuses in the layer until the concentration becomes homogeneous. Remember that the supposition was that no transport or very inefficient transport occurs at the layer borders. The time the system takes to become homogeneous is quite short, in the order of some ms.

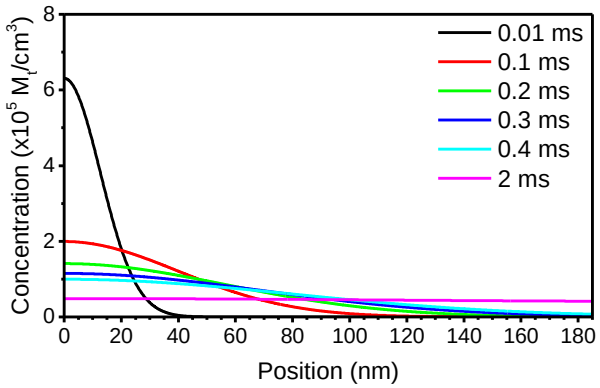

Fig. 3.7 Concentration profile of methanol inside a 185-nm-thick CA layer at different times.

To understand how much the concentration of methanol is homogeneous inside the layers, we compare the profiles with their variations. Indeed, we calculate the standard deviation of the concentration inside the layer and then divide by its mean value. Repeating the measure for each time under consideration, we can then observe how the dishomogeneity of the system decays over time. Fig. 3.8 reports this relative standard deviation as a function of time. After just 4 ms, the dishomogeneity drops by almost 3 orders of magnitude. If we compare this time with the typical experimental transition time observed in Fig. 3.5, we notice that the latter, being in the order of minutes, is much longer. Then, supposing that the processes occurring during exposure is limited by interlayer mass transport and not intralayer diffusion is self-consistent.

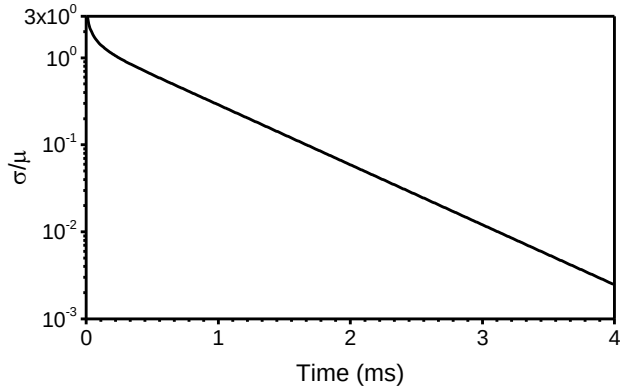

Fig. 3.8 Mean normalized standard deviation of the concentration profile of methanol in a CA layer as a function of time.

Simulation of the sensor optical response

The model so far proposed is able to simulate the swelling of polymer layers inside a DBR and supply their thickness as a function of time. However, it is not able to directly give the spectral response of the system. To calculate the spectral response, it is possible however to use the transfer matrix method.[30] The method is suitable to calculate the transmittance and reflectance spectra of planar multilayer structures once the parameters of the system are known. In particular, the most important parameters are the thickness of the layers composing the PhC and their refractive index. We can calculate the thicknesses using the model discussed in this chapter, but we have no information about the change of refractive index of polymers during the exposure to solvents. Since the layers change their thickness adsorbing solvent, one may think that also the refractive index of the polymer should change.

With the optical data in our hands, we cannot assess on the role of the refractive index during exposure. However, as a first approximation, we can suppose that, if a change of the index occurs, it is negligible compared to the change in thickness. Indeed, while the thickness may double, the refractive index cannot have so strong variations as empirical evidence shows. Observing Fig. 3.4 and Fig. 3.5, the PBG before and after exposure retains similar widths, meaning that the dielectric contrast between the materials composing the DBR is not significantly changed. At this point, we assumed that the refractive index of each

materials remains constant during exposure. Moreover, we can estimate a change in the refractive index using the Drude model for effective medium.[31] Let us reduce ourselves to the case of CA and methanol again. We suppose that the methanol penetrates inside the free volume created swelling the polymer and condensates there. The swelling induced by methanol is 185/167 which is the ratio between the final and initial thickness of the CA layers as extracted by optical simulations. If we suppose that the excess volume is only methanol and considering a refractive index of 1.33,[32] we can extract a modification in the refractive index of 0.8%, which is much lower than the 11% change in thickness. Since the modification is very reduced, we used the dispersions previously measured through ellipsometry for non-swelled films (chapter 2) to simulate the optical response of the systems without accounting for solvent induced changes.

Model parameters and critical points

The model has some critical points. First of all, we supposed no change in refractive index. Although this is a reasonable assumption as the experimental evidences suggest, it may not be valid in a lot of different solvent-polymer pairs we can investigate Indeed, in the final part of this chapter, we report an example where the index seems to change.[33]

Another critical point is the assumption that the swelling is linear with the solvent concentration. A supposition like that may be real for small quantities of solvent but may change for higher concentrations.

The fact that we supposed fast diffusion of solvent inside one of the two layers means that is the non-swelling polymer to limit the diffusion process which may be a too crude approximation.

Moreover, the model relies on some parameters which are just simulation parameters and are not simply related to known and easily measurable physical properties. One example is the permeability P used to characterize the diffusion through a non-permeable layer. In order to have a real estimation of this parameter, we need to know the exact diffusivity of the barrier layers as well as the sorption coefficient of every layer in the system.

Due to these reasons the model cannot be used to give quantitative analysis. It can however be used to understand in a qualitative way what's happening inside a polymer PhC during exposure to solvents in very particular cases like the ones we studied.

Effects during solvent exposure

Having a model that simulates the exposure of DBRs to solvents, we can now better investigate what happens inside the PhC in a qualitative way. We limit ourselves to the cases reported before in this chapter. To simulate sample exposure, we used the structures reported in Fig. 3.9 The panel (a) reports the structure exposed to methanol, which is composed by the glass, 30 alternated layers of PS and CA and a final PS layer in contact with air. Panel (b), instead, reports the structure exposed to PS which is composed by the glass, 30 alternated layers of PS:nanocomposite and CA and a final PS:nanocomposite layer in contact with air.

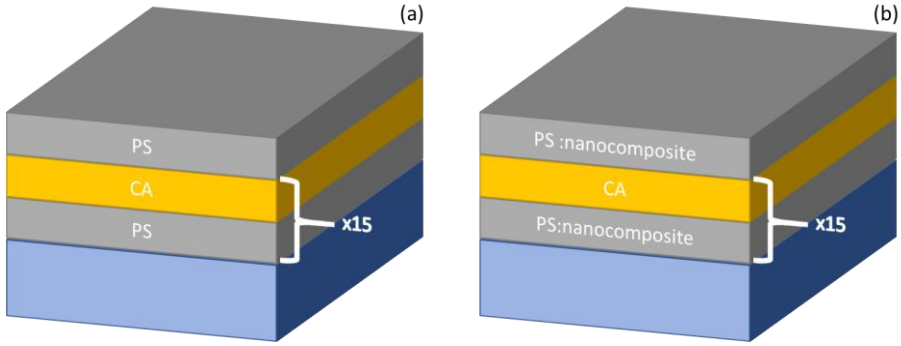

Fig. 3.9 Schematic structure of the DBRs used to create the simulations of this chapter. (a) Structure of the sample used for methanol exposure. (b) Structure of the sample used for toluene exposure.

Fig. 3.10 reports a contour map showing the simulated reflectance of the PS/CA DBR exposed to a solvent that modifies the properties of CA layers only. The parameters are chosen in order that the CA layers swell from 167 nm when dry to 185 nm when fully exposed. The permeabilities, as already discussed, are arbitrary parameters. They have been chosen in a way that $P_{DBR} = 1000\ P_{ext}$. In the map, in light blue is the low reflectance background while in red is the high reflectivity created by the PBG. As time passes, the PBG shifts from about 850 nm to about 950 nm. The process is fast and the PBG position stabilizes in a short time.

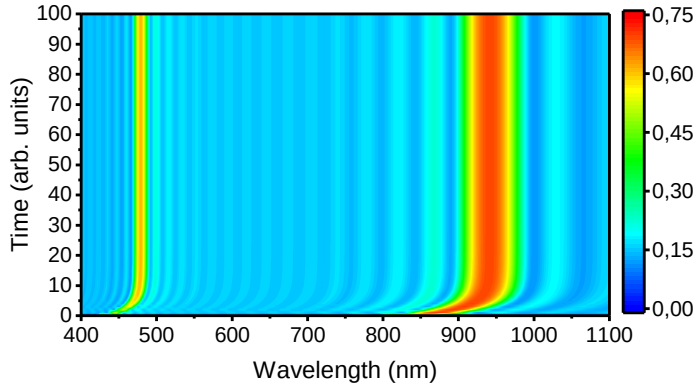

Fig. 3.10 Contour-plot of the modeled temporal evolution of a PS/CA DBR reflectance spectra during exposure to a CA solvent. The permeabilities maintain the ratio $P_{DBR} = 1000 P_{ext}$.

If we observe Fig. 3.5, we can notice that in the experimental case the PBG position is almost constant for long exposure times, in agreement with our model. However, a careful analysis shows that the swelling is not completely arrested for the time interval we examine. Indeed, as the PBG shifts, the shift becomes slower but a very weak drift is still visible. Although our model gives a good approximation of the DBR behavior, it is not able to reproduce in full the experimental data unless we consider a non-linear permeability, hence, to calculate the flux of material from one layer to the next one we would have to leave Eq. 3.5 and use a more complex law:

$$J_{i\rightarrow i+1} = P_{i,i+1}(c_i - c_{i+1}) + P^{NL}_{i,i+1}(c_i - c_{i+1})^2 \quad (3.19)$$

Such special case may be induced if the permeability is not constant with solvent concentration, but this hypothesis is far outside the scope of this work, which is limited to provide a first tentative description of the phenomenon. Notice that, at the best of our knowledge, this correlation between permeation and optical response has never so far reported in literature and what is more interesting from our point of view, instead, is the behavior of the different layers being exposed and how the PBG shifts uniformly. Fig. 3.11 reports the thickness of all the layers composing the DBR during vapor exposure using the proposed model. In this case, all the plots are superimposed, meaning that at any moment all the layers have the same thickness. In this situation, the periodicity of the system is maintained and the PBG never disappear.

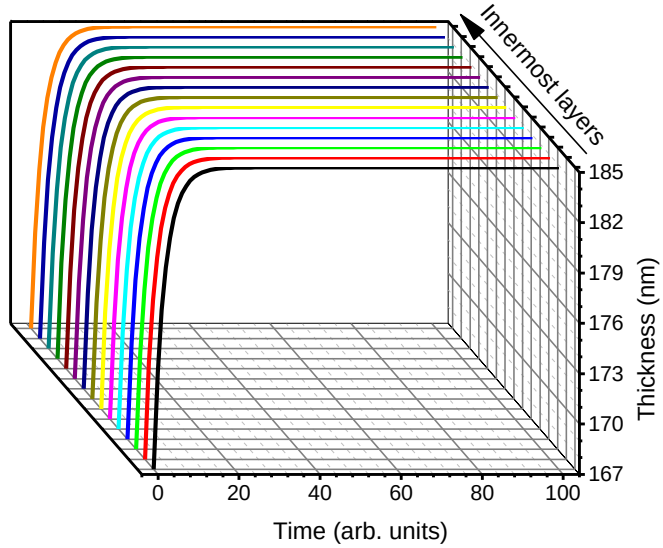

Fig. 3.11 Thickness of the different layers composing the simulated DBR during exposure.

If the permeability ratio is changed, instead, the shift of the PBG becomes more complicate. In order to study the effects of different permeabilities we can analyze the case of Fig. 3.4, which reports the spectra of a PS:nanocomposite/CA DBR exposed to toluene vapors. In that case, as already described, the PBG does not shift as a single entity but first disappears and then reappears at longer wavelengths showing many side bands in the meanwhile. Such effect may also be reproduced by our model. We can simulate the response using the known refractive indexes and the thicknesses obtained by optical simulations and profilometries.[11] Fig. 3.12 reports the simulated spectra. The permeabilities have been chosen in a way that $P_{DBR} = P_{ext}$. Again, the time scale is in arbitrary units because the model is not able to supply a quantitative modeling, at the moment. In order to have a fully quantitative analysis, the P coefficient should be measured and not used as fit parameters.

Nonetheless, we can recognize all the effects previously mentioned. The PBG disappears and rappears again at longer wavelengths. At the same time, some side bands gain in intensity and the disappear again.

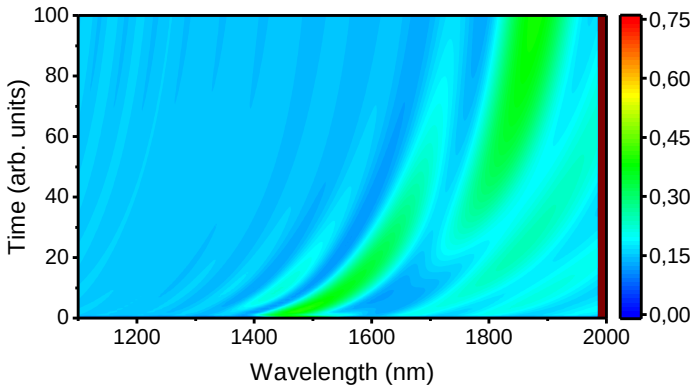

Fig. 3.12 Contour-plot of the modeled temporal evolution of a PS:nanocomposite/CA DBR reflectance spectra during exposure to a PS solvent. The permeabilities maintain the ratio $P_{DBR} = P_{ext}$.

It is interesting to study the thickness of each layer in this case. Fig. 3.13 reports the thickness of each layer calculated by the model. Conversely to the case of Fig. 3.11, the thicknesses are not superimposed. Each layer swells from 378 nm at the beginning to almost 515 nm in the end but with different speeds. Data in Fig. 31.13 show that, for some time intervals, every layer has a different thickness from the others, breaking the periodicity needed to create the PBG. This is visible in the reflectance spectra of Fig. 3.12 when the PBG disappears from 5 to 20 time units.

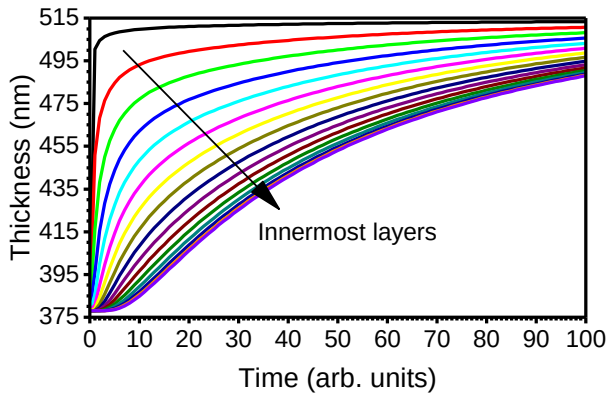

Fig. 3.13 Thickness of the different layers composing the simulated DBR during exposure.

The main difference among the two cases of Fig. 3.10 and Fig. 3.12 is in the ratio between the external and internal permeability. These two modeling parameters are indicative of the resistance encountered by the solvent during the diffusion from air to the first swelling

layer and from one layer to the next one, respectively. Such difference must be dictated by differences in the non-soluble layers. In the case of methanol exposure, the first PS layer prevents direct contact between air and CA. In this way, it strongly hinders the adsorption of solvent. Such barrier, however is not so strong inside the PBG where the diffusion from one CA layer to the next one is much faster. This difference in permeation barrier may be assigned to mechanical and chemical stresses induced by the growth of CA layers over the PS films; growing that lacks in the outermost PS barrier stratum. The high internal permeability allows the layers to immediately homogenize their concentrations before more solvent can be adsorbed by the DBR.
In the case of the PS:nanocomposite DBR exposed to toluene, instead, the outermost layer is composed by the polymer that swells. We can suppose that, in this case, the uptake of solvent by the outermost layer is even faster than the internal diffusion and the swelling layers do not have enough time to become homogeneous before the first layer uptake more solvent.
Using this model then, we have been able to have a better understand of the processes occurring during DBR exposure to solvents. The results also encourage further developments and improvements in the model in order to transform a qualitative analysis tool to a fully quantitative instrument. To this end, permeability, sorption, and diffusion measurements are key factors as would allow us to obtain the parameters we are now just arbitrarily setting.

Cellulose ternary planar photonic crystals for sensing

During the author's PhD thesis work, part of the time was dedicated to the production of a ternary photonic crystal using cellulose in collaboration with Prof. Robert Schennach from the Graz University of Technology.[33] Cellulose is biodegradable, renewable and one of the most abundant polysaccharides in nature. Despite its vast employment since millennia, it still is a material under a lively investigation. It is used for many applications and in many forms as fibers, films, plastics, composites and paper.[34] For the first time, we demonstrated the creation of cellulose planar photonic crystals using solution processing and studied their application for sensing. The samples we created were produced using spin coating in a bottom-up approach.
The multilayered photonic crystal structure subject of this study is composed by seven alternated tri-layers of Cellulose, Polyvinyl alcohol (PVA), and PVK.
PVA was dissolved in a 50/50 volume mixture of water and ethanol (20 g/l) while PVK was dissolved in toluene (28 g/l). Cellulose is hard to solvate in common organic solvents and it is difficult to form a solution easy to process by spin coating. Some solvents have been proposed to prepare thin film of cellulose like trifluoroacetic acid,[35] N-methylmorpholine-N-oxide with water[36], or lithium chloride in dimethylacetamide.[37] Such solvents, however, have been used to produce single layers and they cannot be efficiently used to grow a multilayer structure were the growth of several layers one over each other requires stringent conditions.[38] We used trimethylsilyl cellulose (TMSC) with a degree of substitution of 2.8–3.0 as a pure cellulose precursor.[39-43] 5 g/l TMSC have been dissolved in toluene and then heated to 80 °C in order to favor the dissolution. Such solutions have been filtered

using a PTFE syringe filter (0.2 µm) and then spin cast using the same conditions of the other polymers (125 rps for 60 seconds). After a thermal treatment, these new layers have been exposed to hydrochloric acid vapors. A drop of HCl 10% has been put in a closed petri dish together with the new spun layer so that the liquid does not touch the sample. The sample has been then kept inside the chamber for ten minutes.
The creation of a trilayer structure was motivated by the fact that the toluene solubility of TMSC might create problems when casting it over PVK layers since it will destroy the surface exposed to the solvent. The PVA layers are then inserted in order to protect the PVK ones.
Samples we obtained show good optical quality and are quite homogeneous. Fig. 3.14 reports reflectance spectra recorded in different spots on the surface of a sample. The spectra clearly show a reflectance peak at 460 nm which is about 100 nm wide. This is the signature of the PBG. Below 300 nm, the typical absorptions of the carbazolyl group[44-45] are observed mixed to the second diffraction order photonic band gap, which is often observed in polymer DBR and microcavities.[13, 46-47] Moreover, interference fringes are detected in the spectra background, which further testify the optical quality of the ternary structure. Fringes deeply extend in the near infrared. Comparing the spectra recorded in different points, it can also be seen that the optical response is quite uniform thus indicating the PhC being quite homogeneous over the whole surface.

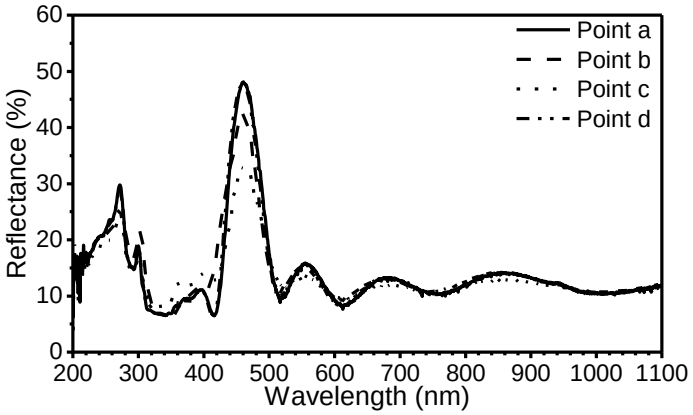

Fig. 3.14 Reflectance spectra of the triblock DBR as recorded in different points over the surface of the sample.

We also examined the trilayer sample through transmission electron microscopy (TEM). Fig. 3.15a shows a TEM cross section of the ternary photonic crystal. Despite the evident delamination, which is proven by the deformed bottom layer and by the other TEM image in Fig. 3.15b, we can observe many layers ordered in a repeated trilayer structure. This proves that the bottom-up spin coating does create different layers and avoid percolations and mixing of polymers. However, the periodicity of the layers is quite bad. We can suppose that this is given by the immersion in water used to prepare the samples for TEM imaging. Indeed, during the preparation for this analysis, the sample has been manually peeled off, embedded in epoxy (Specifix 40, Struers GmbH, Germany), cured for 4h at 70°C, and afterwards sliced using an ultramicrotome UC6 (Leica Microsystems, Vienna, Austria). The

cut ribbon was left to fall in water and then collected from the liquid surface and transferred to a 75 mesh grid coated with formvar (using a Perfect Loop, Diatome). In the process, the structure inevitably came in contact with the water that could penetrate deep inside the crystal and swell cellulose creating the disorder visible in Fig. 3.15a and b.

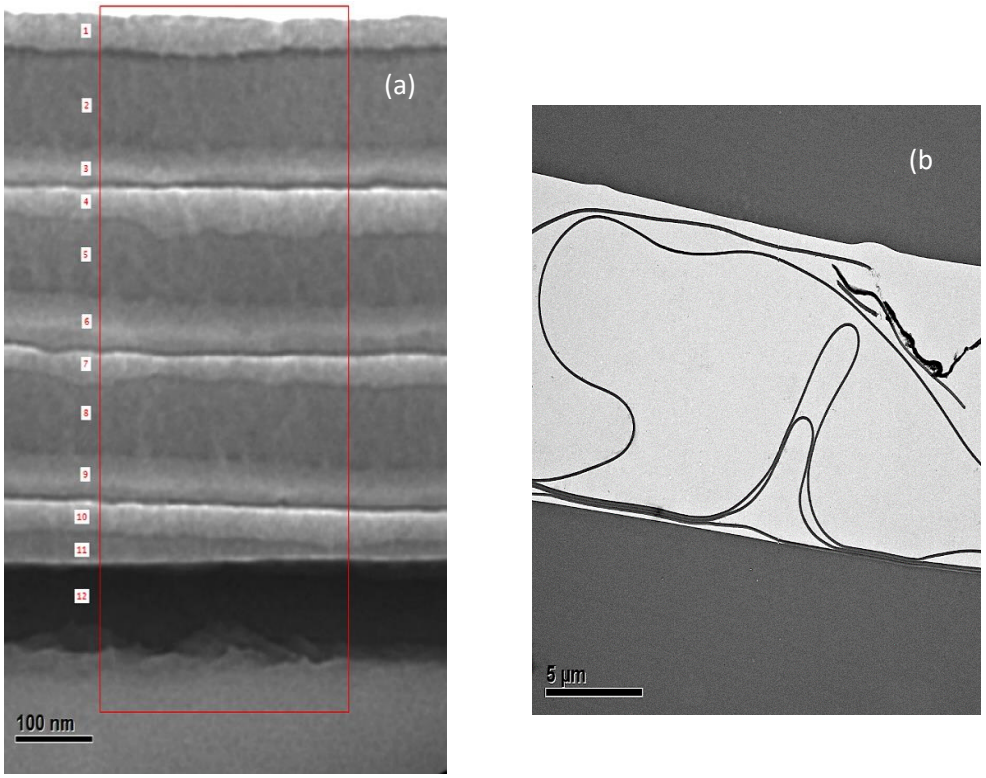

Fig. 3.15 TEM cross section of the spin coated planar ternary PhC.

Since the contact with water was of the sample was so detrimental for the sample, we have envisaged the use of this cellulose trilayer structure for sensing of water vapors. We then exposed the created PhC to water vapors for two and a half hours. Fig. 3.16 reports the transflectance spectra recorded during this time. At the end of the process, we can observe three main effects. The PBG redshifts of about 50 nm, its intensity increases, and its width passes from 0.33 eV to 0.41 eV. The red shift is induced by the swelling of the polymer layers as previously discussed in this chapter. The broadening of the PBG upon exposure and the corresponding intensity increase instead, can be due to some disorder induced in the structure during exposition or to a change in refractive indexes. Such change, which has been neglected during the rest of this chapter, seems to be quite strong and the remarkable response of our tri-block DBR to vapor strongly suggests the development of similar systems for polar molecules vapors sensing. Indeed, even though we are working in saturated atmosphere (unitary activity), the red shift observed for water vapor exposition (about 50 nm) and the change in the width is very clear. The entity of the shift, together with the position of the bandgap inside the visible spectra, joined to the easy fabrication procedure,

envisage the use of our planar all-polymer photonic crystals as chromatic photonic sensors with naked eye detection.

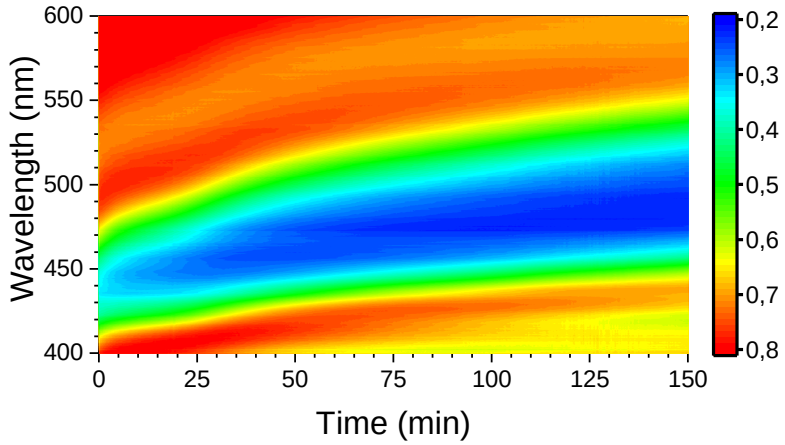

Fig. 3.16 Transflectance of the triblock planar PhC as a function of exposure time to water vapors.

References

(1) Agency for Toxic Substances and Disease Registry (ATSDR). Toxicological Profiles. (accessed 2017/12/11).
(2) Straif, K.; Cohen, A.; Samet, J., *Air Pollution and Cancer, IARC Scientific Publication No. 161*. International Agency or Research on Cancer: Lyon, France, 2013.
(3) Guo, H.; Lee, S. C.; Chan, L. Y.; Li, W. M., Risk Assessment of Exposure to Volatile Organic Compounds in Different Indoor Environments. *Environ. Res.* **2004,** *94*, 57-66.
(4) Wang, S.; Ang, H. M.; Tade, M. O., Volatile organic compounds in indoor environment and photocatalytic oxidation: State of the art. *Environ. Int.* **2007,** *33*, 694-705.
(5) Phillips, M.; Gleeson, K.; Hughes, J. M. B.; Greenberg, J.; Cataneo, R. N.; Baker, L.; McVay, W. P., Volatile organic compounds in breath as markers of lung cancer: a cross-sectional study. *The Lancet* **1999,** *353*, 1930-1933.
(6) Duan, J.; Tan, J.; Yang, L.; Wu, S.; Hao, J., Concentration, sources and ozone formation potential of volatile organic compounds (VOCs) during ozone episode in Beijing. *Atmos. Res.* **2008,** *88*, 25-35.
(7) Hansen, J.; Sato, M.; Ruedy, R.; Lacis, A.; Oinas, V., Global warming in the twenty-first century: An alternative scenario. *Proc. Natl. Acad. Sci. USA* **2000,** *97*, 9875-9880.
(8) Lippmann, M., Health Effects of Ozone: A Critical Review. *JAPCA* **1989,** *39*, 672-695.
(9) Seinfeld, J. H.; Pandis, S. N., *Atmospheric Chemistry and Physics: From Air Pollution to Climate Change*. John Wiley & Sons: 2012; p 1119.
(10) Vlaanderen, J.; Straif, K.; Ruder, A.; Blair, A.; Hansen, J.; Lynge, E.; Charbotel, B.; Loomis, D.; Kauppinen, T.; Kyyronen, P.; Pukkala, E.; Weiderpass, E.; Guha, N., Tetrachloroethylene Exposure and Bladder Cancer Risk: A Meta-Analysis of Dry-Cleaning-Worker Studies. *Environ. Health Perspect.* **2014,** *122*, 661-666.
(11) Lova, P. Polymer Distributed Bragg Reflectors for Label-free Vapor Sensing. PhD Thesis, Nanyang Technological University, Singapore, 2017.
(12) Lova, P.; Bastianini, C.; Giusto, P.; Patrini, M.; Rizzo, P.; Guerra, G.; Iodice, M.; Soci, C.; Comoretto, D., Label-Free Vapor Selectivity in Poly(p-Phenylene Oxide) Photonic Crystal Sensors. *ACS Appl. Mater. Interfaces* **2016,** *8*, 31941-31950.
(13) Lova, P.; Manfredi, G.; Boarino, L.; Comite, A.; Laus, M.; Patrini, M.; Marabelli, F.; Soci, C.; Comoretto, D., Polymer Distributed Bragg Reflectors for Vapor Sensing. *ACS Photonics* **2015,** *2*, 537-543.
(14) Toray Picasus Product Presentation. http://www.toray.com/products/films/fil_012.html (accessed 2017/10/13).

(15) Xie, Z.; Cao, K.; Zhao, Y.; Bai, L.; Gu, H.; Xu, H.; Gu, Z.-Z., An Optical Nose Chip Based on Mesoporous Colloidal Photonic Crystal Beads. *Adv. Mater.* **2014,** *26*, 2413-2418.
(16) Potyrailo, R. A.; Bonam, R. K.; Hartley, J. G.; Starkey, T. A.; Vukusic, P.; Vasudev, M.; Bunning, T.; Naik, R. R.; Tang, Z.; Palacios, M. A.; Larsen, M.; Le Tarte, L. A.; Grande, J. C.; Zhong, S.; Deng, T., Towards outperforming conventional sensor arrays with fabricated individual photonic vapour sensors inspired by Morpho butterflies. *Nat. Commun.* **2015,** *6*, 7959.
(17) Bajoni, D. Optical Spectroscopy Of Photonic Crystals And Microcavities. PhD thesis, Università di Pavia, 2003.
(18) Comoretto, D., *Organic and Hybrid Photonic Crystals*. 1 ed.; Springer International Publishing: Switzerland, 2015; p 497.
(19) Bonifacio, L. D.; Puzzo, D. P.; Breslav, S.; Willey, B. M.; McGeer, A.; Ozin, G. A., Towards the Photonic Nose: A Novel Platform for Molecule and Bacteria Identification. *Adv. Mater.* **2010,** *22*, 1351-1354.
(20) Hinterholzinger, F. M.; Ranft, A.; Feckl, J. M.; Ruhle, B.; Bein, T.; Lotsch, B. V., One-Dimensional Metal-Organic Framework Photonic Crystals Used as Platforms for Vapor Sorption. *J. Mater. Chem.* **2012,** *22*, 10356-10362.
(21) Lazarova, K.; Georgiev, R.; Vasileva, M.; Georgieva, B.; Spassova, M.; Malinowski, N.; Babeva, T., One-Dimensional PMMA–V_2O_5 Photonic Crystals Used as Color Indicators of Chloroform Vapors. *Opt. Quant. Electron.* **2016,** *48*, 310-317.
(22) Convertino, A.; Capobianchi, A.; Valentini, A.; Cirillo, E. N. M., A New Approach to Organic Solvent Detection: High-Reflectivity Bragg Reflectors Based on a Gold Nanoparticle/Teflon-like Composite Material. *Adv. Mater.* **2003,** *15*, 1103 - 1105.
(23) Convertino, A.; Capobianchi, A.; Valentini, A.; Cirillo, E. N. M., High Reflectivity Bragg Reflectors Based on a Gold Nanoparticle/Teflon-like Composite Material as a New Approach to Organic Solvent Detection. *Sens. Actuators, B* **2004,** *100*, 212-215.
(24) Mönch, W.; Dehnert, J.; Prucker, O.; Rühe, J.; Zappe, H., Tunable Bragg Filters Based on Polymer Swelling. *Appl. Opt.* **2006,** *45*, 4284-4290.
(25) Ahn, J.; Chung, W.-J.; Pinnau, I.; Guiver, M. D., Polysulfone/silica nanoparticle mixed-matrix membranes for gas separation. *J. Membr. Sci.* **2008,** *314*, 123-133.
(26) Lova, P.; Manfredi, G.; Servida, A.; Comoretto, D., Determination of Vapor Diffusion Coefficient and label-free selectivity by All-Polymer Distributed Bragg Reflectors. **In preparation**.
(27) Brandrup, J. I., Edmund H.; Grulke, Eric A.; Abe, Akihiro; Bloch, Daniel R., *Polymer Handbook (4th Edition)* John Wiley & Sons 2005.
(28) Crank, J., *The mathematics of diffusion*. 2nd ed.; Clarendon Express: Oxford, 1975; p 414.

(29) Perrin, L.; Nguyen, Q. T.; Sacco, D.; Lochon, P., Experimental Studies and Modelling of Sorption and Diffusion of Water and Alcohols in Cellulose Acetate. *Polym. Int.* **1997,** *42*, 9-16.
(30) Makino, T., Transfer Matrix Method with Applications to Distributed Feedback Optical Devices. *Progress In Electromagnetics Research* **1995,** *10*, 271-319.
(31) Braun, M. M.; Pilon, L., Effective optical properties of non-absorbing nanoporous thin films. *Thin Solid Films* **2006,** *496*, 505-514.
(32) El-Kashef, H., The necessary requirements imposed on polar dielectric laser dye solvents. *Physica B: Condensed Matter* **2000,** *279*, 295-301.
(33) Manfredi, G.; Mayrhofer, C.; Kothleitner, G.; Schennach, R.; Comoretto, D., Cellulose ternary photonic crystal created by solution processing. *Cellulose* **2016,** *23*, 2853-2862.
(34) Schurz, J., A bright future for cellulose. *Prog. Polym. Sci.* **1999,** *24*, 481-483.
(35) Geddes, A. L., Interaction of trifluoroacetic acid with cellulose and related compounds. *J. Polym. Sci* **1956,** *22*, 31-39.
(36) Yokota, S.; Kitaoka, T.; Wariishi, H., Surface morphology of cellulose films prepared by spin coating on silicon oxide substrates pretreated with cationic polyelectrolyte. *Applied Surface Science* **2007,** *253*, 4208-4214.
(37) Dawsey, T. R.; McCormick, C. L., The lithium chloride/dimethylacetamide solvent for cellulose: a literature review. *Journal of Macromolecular Science, Part C: Polymer Reviews* **1990,** *30*, 405-440.
(38) Unger, K.; Resel, R.; Czibula, C.; C. Ganser; Teichert, C.; Jakopic, G.; Canazza, G.; S. Gazzo; Comoretto, D. In *Distributed Bragg reflectors: Morphology of cellulose acetate and polystyrene multila*, 6th International Conference on Transparent Optical Networks (ICTON 2014), Graz, Austria, Graz, Austria, 2014; pp 1-4.
(39) Kontturi, E.; Thüne, P. C.; Niemantsverdriet, J. W., Novel method for preparing cellulose model surfaces by spin coating. *Polymer* **2003,** *44*, 3621-3625.
(40) Kontturi, E.; Thüne, P. C.; Alexeev, A.; Niemantsverdriet, J. W., Introducing open films of nanosized cellulose—atomic force microscopy and quantification of morphology. *Polymer* **2005,** *46*, 3307-3317.
(41) Kontturi, E.; Thüne, P. C.; Niemantsverdriet, J. W., Cellulose Model SurfacesSimplified Preparation by Spin Coating and Characterization by X-ray Photoelectron Spectroscopy, Infrared Spectroscopy, and Atomic Force Microscopy. *Langmuir* **2003,** *19*, 5735-5741.
(42) Rohm, S.; Hirn, U.; Ganser, C.; Teichert, C.; Schennach, R., Thin cellulose films as a model system for paper fibre bonds. *Cellulose* **2014,** *21*, 237-249.
(43) Mohan, T.; Kargl, R.; Doliška, A.; Vesel, A.; Köstler, S.; Ribitsch, V.; Stana-Kleinschek, K., Wettability and surface composition of partly and fully regenerated cellulose thin films from trimethylsilyl cellulose. *Journal of Colloid and Interface Science* **2011,** *358*, 604-610.

(44) Comoretto, D.; Dellepiane, G.; Cuniberti, C.; Rossi, L.; Borghesi, A.; LeMoigne, J., Photoinduced absorption of oriented poly[1,6-di(N-carbazolyl)-2,4-hexadiyne]. *Phys. Rev. B* **1996,** *53*, 15653-15659.
(45) Comoretto, D.; Cuniberti, C.; Musso, G. F.; Dellepiane, G.; Speroni, F.; Botta, C.; Luzzati, S., Optical-Properties and Long-Lived Charged Photoexcitations in Polydiacetylenes. *Phys. Rev. B* **1994,** *49*, 8059-8066.
(46) Knarr, R. J.; Manfredi, G.; Martinelli, E.; Pannocchia, M.; Repetto, D.; Mennucci, C.; Solano, I.; Canepa, M.; Mongeot, F. B. d.; Galli, G.; Comoretto, D., In-plane anisotropic photoresponse in all-polymer planar microcavities. *Polymer* **2016,** *84*, 383-390.
(47) Kriegel, I.; Scotognella, F., Band gap splitting and average transmission lowering in ordered and disordered one-dimensional photonic structures composed by more than two materials with the same optical thickness. *Optics Communications* **2015,** *338*, 523-527.

Chapter IV

Spectral redistribution of nanocrystals emission

PhCs and microcavities are interesting systems, which can find many applications. As already discussed throughout this thesis, all-polymer DBRs and microcavities have been already proposed as sensors,[1-3] lasers,[4-7] and all-optical modulators.[8-10] A particular interest is also devoted to the study of the modifications induced by the photonic environment to the properties of emitters. Concerning this argument, experimental works have been focused on inorganic microcavities that require complicated synthetic routes both time and costs expensive.[11-17] Spectroscopic properties, field confinement, and directional emission in the case of all-polymer systems, instead, have not been exhaustively addressed yet.[4-7]
This organic kind of structures can in principle be mass produced thanks to established fabrication technologies currently used in packaging industry,[18-23] hence being interesting from an industrial point of view. On the lab scale, instead, polymer multilayers can be easily prepared by spin-coating as largely discussed throughout the thesis. Moreover, polymer structures can be peeled-off from the substrate leading to free-standing and flexible photonic crystals adaptable to pre-formed surfaces (Fig. 4.1).[1, 5-6, 20-21, 24-33]
To study the optical properties modifications induced by polymer PhCs, a suitable reference material is desirable. In particular, colloidal nanocrystals (NCs) are considerably attractive thanks to their high fluorescence QY and spectral tunability through electronic structure engineering and surface functionalization. This kind of material can be adjusted in composition and shape to obtain tailored and stable electronic properties.[34] The choice of materials and shapes is very wide, offering the possibility to create lot of different NCs. In particular, CdSe have been used in lot of works. CdSe nanoplatelets[35] or core-shell structures as CdSe/CdS dot-in-rods[36] (DiRs) or giant-shells[37-38] have been used in several light-emitting applications,[39-43] including lasers working both in the pulsed and in the continuous wave regime.[44-50] Given their high surface-to-volume ratio, surface functionalization offers a great way to improve NCs properties. For instance, it is possible to improve passivation thus reducing photoluminescence (PL) quenching defects[51-55] or allowing solubility in many organic and polar solvents including water.[56-60] Surface functionalization can also promote self-organization and preparation of nanocomposites that can become crucial for solid state photonic structures and devices.[4, 24, 61-67]

In this chapter, we present the results producing high quality, large area, all-polymer planar microcavities embedding CdSe/CdS DiRs in the cavity layer. The microcavity itself is produced by spin coating, better treated in chapter 2. Here, we introduce the optical properties of the microcavity and discuss the emission modifications induced by the PhC.

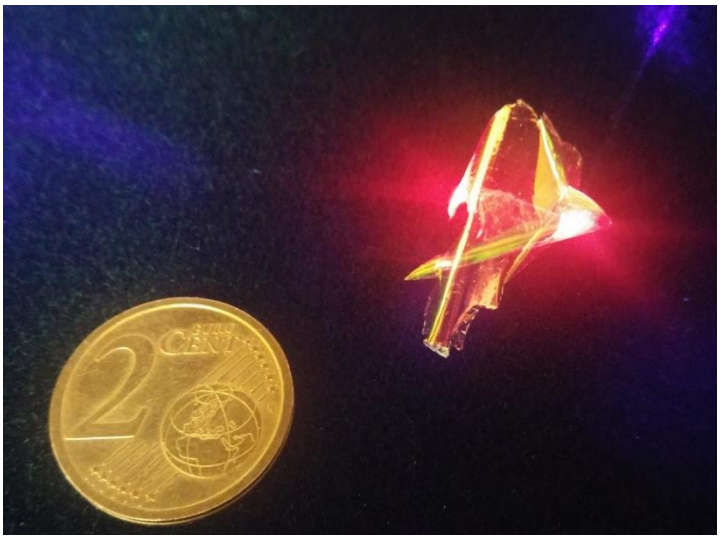

Fig. 4.1 Freestanding rolled-up microcavity under violet laser excitation where the bright DiRs red fluorescence is observed.

Nanocrystals properties

We used CdSe/CdS DiRs produced following a known procedure.[36] DiRs have been synthetized starting from cores having average size of 4.1 nm. The shells, shown in a TEM micrograph of Fig. 4.2a, have an average diameter of 4.7 ± 0.5 nm while having variable length that follows the distribution of Fig. 4.2b. Indeed, the statistics of the nanorod size distribution indicates a dominant population with length centered around 35 nm. However, we can also observe the presence of a large amount of shorter nanorods with lengths ranging from 5 to 25 nm. We consider them as impurities.

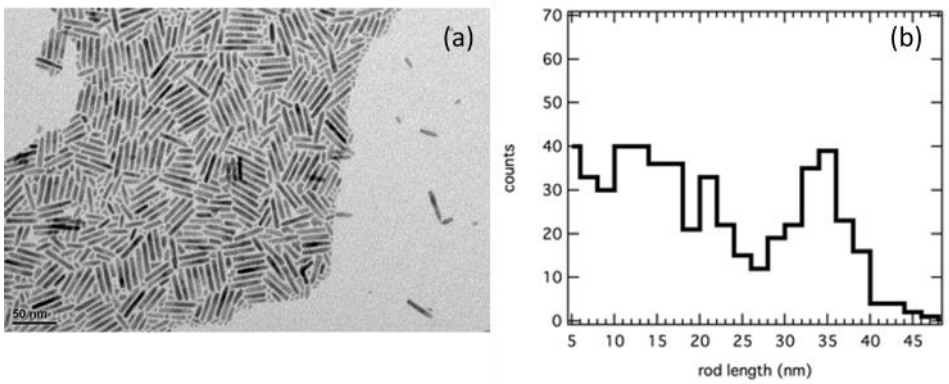

Fig. 4.2 (a) TEM micrograph of CdSe/CdS DiRs. (b) Size distribution of DiRs retrieved from TEM data.

Fig. 4.3 shows absorbance and PL spectra of DiRs dispersed in toluene. At 602 nm and 557 nm we can see two defined peaks related to the CdSe cores.[36] The absorption onset at 500

nm is created by the CdS DiRs shells. Comparing the features owed to CdSe to those owed to CdS, we can see how the latter ones are more intense. This is given by the larger amount of CdS in the nanocrystals. The PL spectrum (in red) of DiRs is centered at 612 nm and has a FWHM of 24 nm (79 meV). It is 10 nm Stokes-shifted compared to the CdSe cores band edge absorption. Moreover, the PL is asymmetrical. Its shape and the presence of a non-homogeneous distribution nanorods lengths (Fig. 4.2b) suggest that the PL can be the convolution of more peaks.

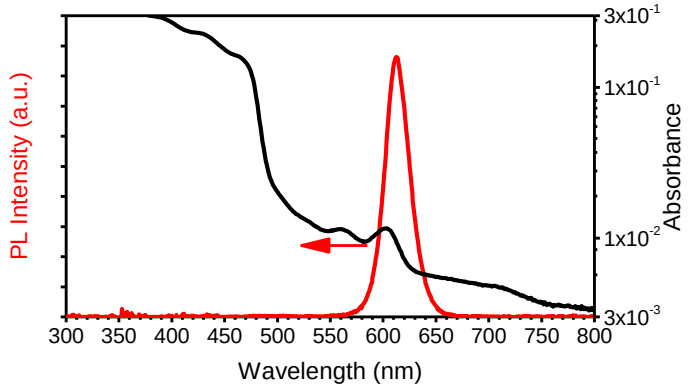

Fig. 4.3 Absorption (black) and fluorescence (red) spectra of nanocrystals dispersed in toluene.

Indeed, we de-convolved the spectrum into two Voigt-like (convolution of Gaussian and Lorentz lineshapes, as reported in Eq. 4.1) functions separated by about 10 nm.

$$y = y_0 + A \cdot \frac{2\ln 2}{\pi^{\frac{3}{2}}} \frac{w_L}{w_G^2} \cdot \int_{-\infty}^{+\infty} \frac{e^{-t^2}}{\left(\sqrt{\ln 2}\frac{w_L}{w_G}\right)^2 + \left(\sqrt{4\ln 2}\frac{x - x_c}{w_G} - t\right)^2} dt \qquad (4.1)$$

In Eq. 4.1, y_0 is a baseline value, A is the area of the Voigt function (in nm), and w_L and w_G are the width of the lorentzian and gaussian functions used in the convolution, respectively. The results of the deconvolution are shown in Fig. 4.4a and in Table 4.1. According to the size distribution (Fig. 4.2b) and to the relation between PL properties and DiRs length, we can assign the low energy peak (617 nm) to the emission of longer DiRs, while the high energy one (608 nm) is due to shorter DiRs.[34, 36]

Fig. 4.4b shows the ratio spectrum obtained by dividing the peaks obtained through the fit procedure. This shows that peak 1 (the one created by shorter DiRs) has its main contribution to the PL around 600 nm, where the ratio spectrum shows its minimum. On the other hand, peak 2 (created by longer DiRs) dominates at about 630 nm where the ratio spectrum is maximum.

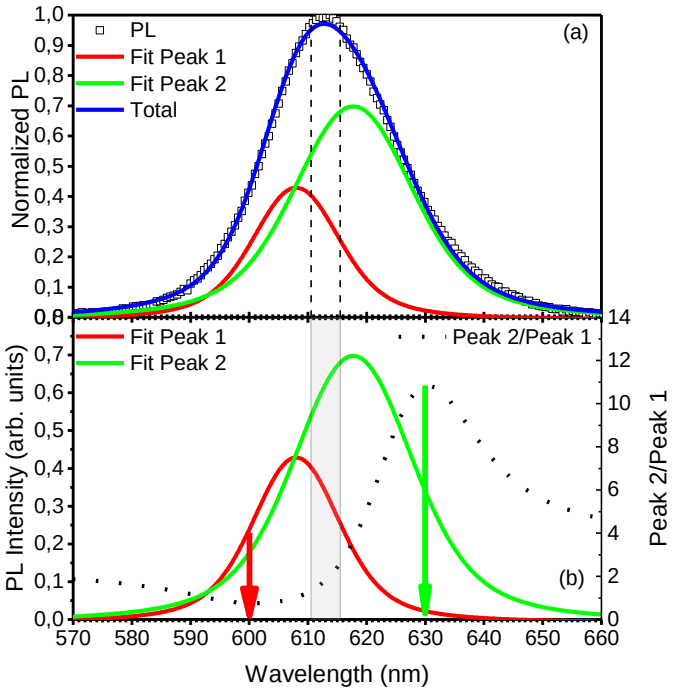

Fig. 4.4 (a) Deconvolution of the PL spectrum of the DiRs:PS nanocomposite reference film (blue line), peak 1 component (red), peak 2 component (green); (b) comparison of the peak 1 and peak 2 components, showing their spectral ratio (peak2/peak1) as dotted line. Arrows show spectral position where time resolved PL is recorded: 600 nm, mainly peak 1; 630 nm, mainly peak 2.

Table 4.1 Parameters of the fitted functions.

	x_c (nm)	Area (nm)	W_G (nm)	W_L (nm)
Peak 1	608	10	13	8
Peak 2	617	22	18	11

The reason behind the choice of deconvolving DiRs in two main components will be clearer further ahead in the chapter as the emission process will be discussed in more detail.

Nanocomposite properties

The aim of the work was to study the properties of DiRs embedded in a high optical quality all-polymer microcavity. To reach this objective, we opted for the use of a suitable nanocomposite. This has been obtained dissolving polystyrene into a DiRs:toluene dispersion (40 g/l, PS; 0.8 g/l, DiRs) and spin coating the solution at 4800 rpm. The grown nanocomposite films were then annealed at 80 °C for 10 minutes.

Fig. 4.5 reports the absorption and PL spectra of DiRs:PS nanocomposite films. There are remarkable differences in absorption from the toluene DiRs dispersion (Fig. 4.3). Between

500 nm and 650 nm, the peaks clearly observed in the liquid suspension are not visible in the case of spin coated DiRs:nanocomposite film. Instead, a broad tail is dominant for those wavelengths. This can be assigned to the scattering generated by the large amount of DiRs loaded into the nanocomposite. The CdS shell absorption still creates a peak at 480 nm.
The nanocomposite and the liquid suspension PLs shows the exact same shape, suggesting that light scattering induced by heavily loaded DiRs does not affect the electronic properties of the particles, which still act as isolated emitters.
To better understand DiRs aggregation does occur in nanocomposite film, we studied them by confocal microscopy; Fig. 4.6 shows confocal reflection (a) and fluorescence microscopy (b) images of a DiRs:PS nanocomposite film. We can observe a homogeneous DiRs distribution on sub-micron scale, indicating that in the nanocomposite aggregation effects are limited.

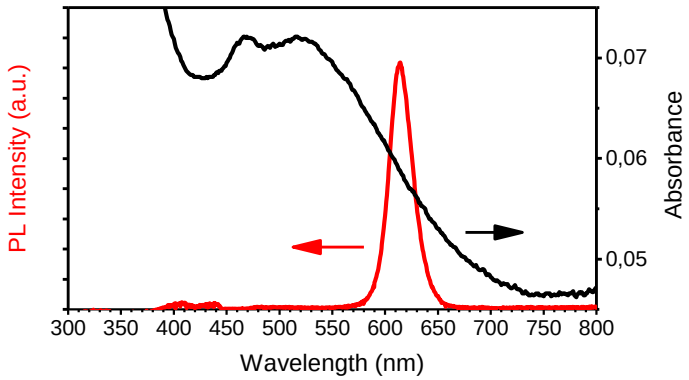

Fig. 4.5 Absorption (black) and fluorescence (red) spectra of nanocrystals dispersed in PS.

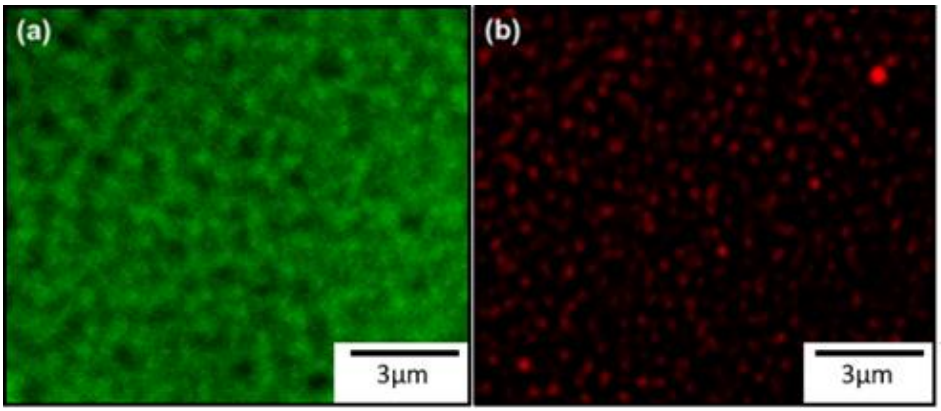

Fig. 4.6 Optical confocal microscopy images of the DiRs:PS nanocomposite film. (a) Reflection of a laser at 514 nm wavelength integrated over 500-550 nm. (b) DiRs fluorescence excited with a laser at 405 nm and recorded in the 575-625 integrated spectral range in the same spot as in (a).

Microcavity optical properties

Once we studied the properties of a reference nanocomposite film, we created a planar microcavity containing the emitting material as defect layer. As stated in previous chapters, it's possible to spin coat microcavities just creating one layer over each other. Indeed, we first created a DBR of 25 bilayers of PVK and CA by spin coating different solutions at 7500 rpm on 22x22 mm^2 glass substrate. PVK was dissolved in toluene (28 g/l) and CA was dissolved in 4-hydroxy-4-methyl-2-pentanone (35 g/l). After each PVK deposition, the sample was annealed at 80 °C for 1 minute to avoid percolation of CA solvent through the PVK layers.[68] After the first DBR was ready, we grown a DiRs:PS nanocomposite film over the last layer (made of CA). Once the nanocomposite film was annealed, we then created another DBR over it using the same procedure used to create the one below. Operating this way, as also shown in chapter 2, allows to obtain interfacial roughness of about 1 nm and to finely control the thickness of the layers.[28, 69] The microcavity structure is sketched in Fig. 4.7.

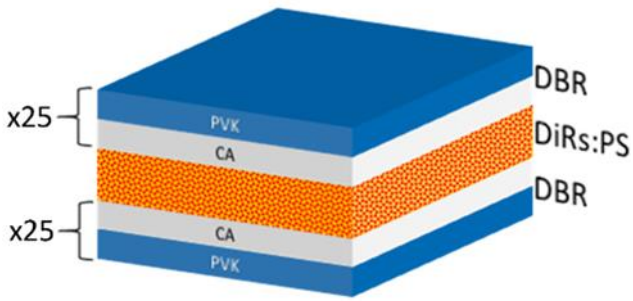

Fig. 4.7 Scheme of the planar microcavity.

Once we obtained the microcavity, we studied it using optical techniques. Its reflectance spectrum (Fig. 4.8) shows an intense and broad peak between 580 and 646 nm. This is created by the PBG of the PhC. The FWHM of the PBG band is 66 nm. This width is a direct consequence of the relatively large (compared to other polymer systems) dielectric contrast between PVK (n ~ 1.67 at λ=600 nm) and CA (n ~ 1.47 at λ=600 nm) as also reported in Chapter 2.[70] Inside the PBG, we observe a sharp minimum. It is centered at 613 nm and has a FWHM of ~2.5 nm. This, minimum in reflectance is created by the cavity mode created by the defect layers inside the PhC. Outside the PBG we can observe modulations induced by interference fringes and, below 350 nm, the reflectance spectrum is influenced by the absorption of PVK aromatic rings.[71-73] We do not observe a second order PBG at ~300 nm, confirming that the thickness of the layers in the dielectric mirrors fulfill the λ/4 condition. The bandwidth of the PBG then, can be analytically calculated as $\Delta E = \frac{4}{\pi} E \frac{|n_h - n_l|}{n_h + n_l}$.[61] According to this equation and to the refractive indexes we have, the expected bandwidth for this system is 60 nm; in good agreement with the experimental value (66 nm).

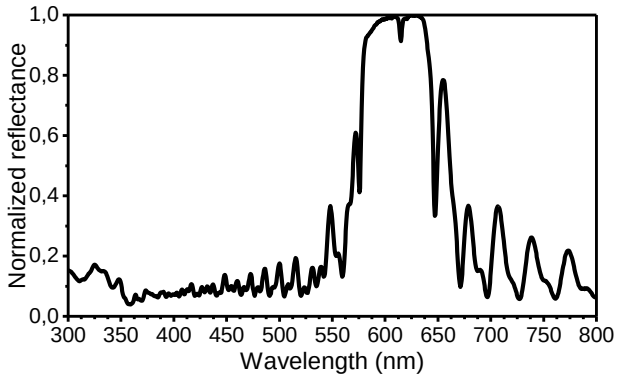

Fig. 4.8 Normalized reflectance spectrum of the microcavity.

To better understand the properties of our microcavity we tried to simulate the optical response of an analog structure through the TMM.[74] Although we had the refractive index of PVK, CA and PS, we were missing the nanocomposite refractive index.
To estimate its complex optical function, then, we first assumed that the DiRs have a small effect on the real part of the nanocomposite refractive index, hence it is very similar to that of PS.[75] We operated a first tentative fit of the transmittance of the microcavity neglecting DiRs absorption and obtaining a first estimation of the system layers thicknesses. However, since DiRs absorption clearly affects microcavity properties, we exploited the previously obtained thicknesses and the absorbance spectra of a reference film to obtain a very rough evaluation of the nanocomposite extinction coefficient. The procedure used was the following:
-The reference film is composed by a glass substrate, a CA layer and the nanocomposite layer as already discussed.
-The absorbance spectrum of the reference and of the glass substrate are recorded.
-The reference absorbance (A_c) is corrected subtracting the out-of-resonance effect of reflection losses.
-The extinction coefficient k is calculated as $A_c = log\frac{1}{T} = 0.43\alpha d = 0.43\frac{4\pi k}{\lambda}d$ where λ is the wavelength and d is the thickness of the nanocomposite layer as obtained by the overall microcavity response fit.
-For λ>700 nm we considered the extinction coefficient negligible (k=0).
-The thickness of the layers composing the microcavity is fitted again using the new extinction coefficient for the cavity layer.
-The procedure is repeated until the new thickness is identical to the previous one within 5%.
The obtained result is reported in Fig. 4.9.

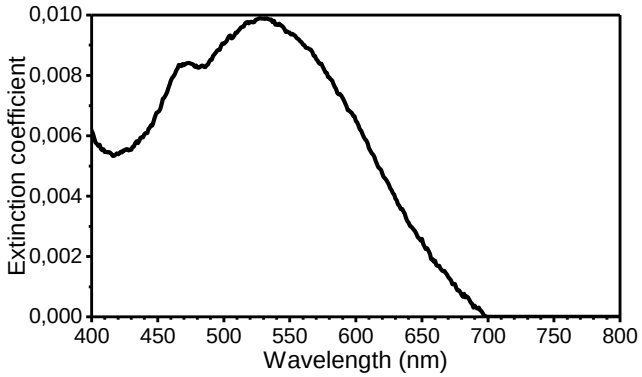

Fig. 4.9 Extinction coefficient of the DiRs:PS nanocomposite as obtained by the reported procedure.

The method we used does not assure us the Kramers-Kronig compatibility of the index we got. Nonetheless, it can be a useful instrument in a first approximation simulation. We fitted the thickness of the layers inside the microcavity and obtained 94 nm for PVK, 100 nm for CA, and 208 nm for DiRs:PS nanocomposite. These values are in agreement with those calculated by the analytical formulas for the λ/4 condition (92 nm for PVK and 104 nm for CA).[61]

Fig. 4.10a shows the microcavity measured and simulated transmittance spectrum. In the range 580-646 nm is visible a band of negligible transmittance containing a sharp and weak maximum centered at 613 nm created by the PBG and the cavity mode, respectively.

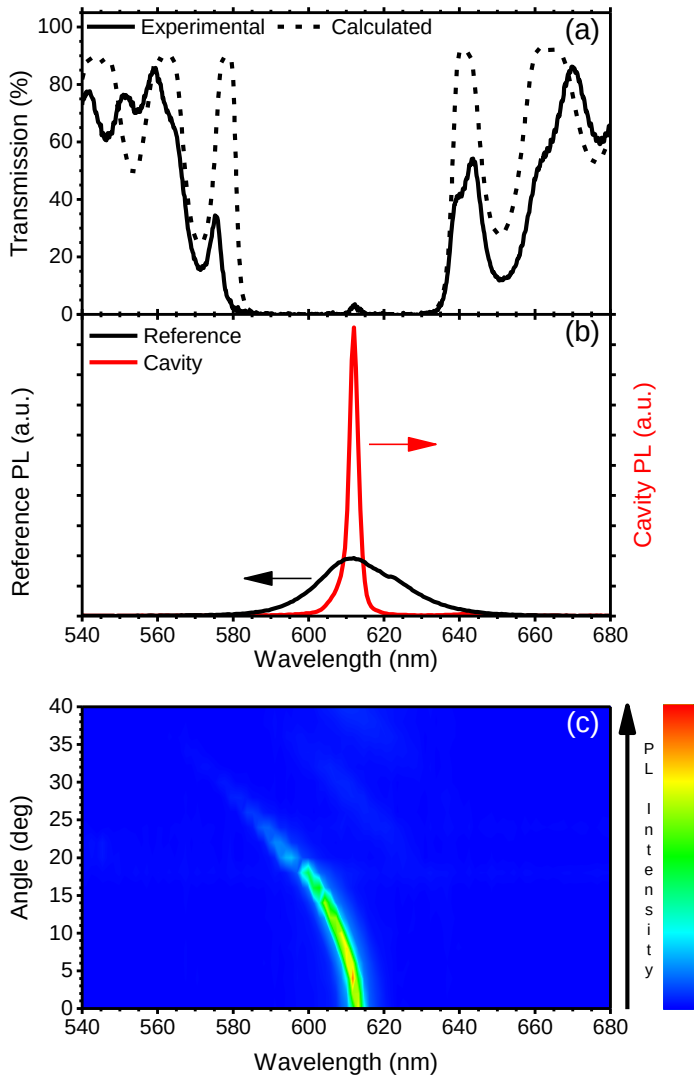

Fig. 4.10 (a) Experimental (continuous line) and calculated (dashed line) microcavity transmission spectra. (b) PL spectra for a microcavity (in red) and for a reference sample (in black) recorded in the very same conditions. (c) Contour plot of the microcavity fluorescence spectra as a function of the collection angle

Simulating the optical response for different angles, (Fig. 4.11) the simulation perfectly accounts for polarized angle-resolved transmittance spectra, further demonstrating the excellent optical quality of the created all-polymer microcavities.[61, 75]

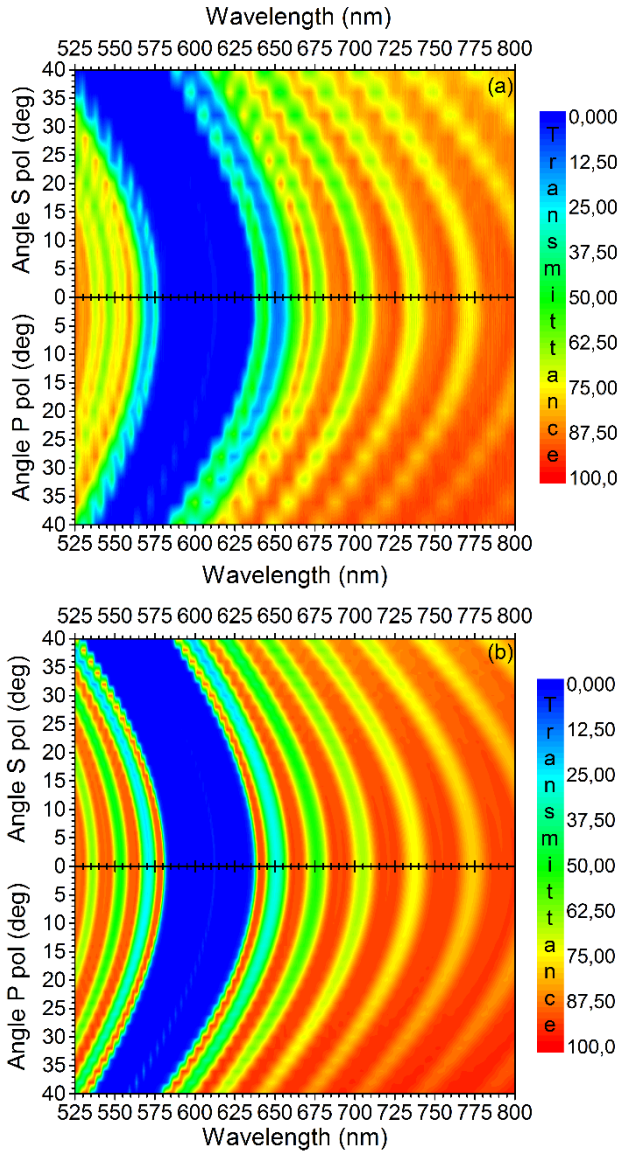

Fig. 4.11 (a) Experimental and (b) calculated transmittance spectra of the microcavity as a function of the incidence angle for S- (upper panel) and P-polarized (lower panel) light.

Fig. 4.10b shows the microcavity PL spectrum compared to the reference one. The two spectra are recorded in the very same conditions. Fig. 4.10 clearly shows the spectral re-shaping induced by the microcavity on the DiRs PL. Indeed, we observe a 10-fold sharpening of the PL spectrum and its reduction from 24 nm for the reference to 2.4 nm for the microcavity. Such difference is better highlighted in Fig. 4.12 that shows the ratio between the emission of microcavity and the emission of the reference. We can also see that the microcavity PL peak intensity is ~5 times larger than the reference one. From Fig. 4.10b is

also possible to extact the microcavity quality factor ($Q = \lambda/\Delta\lambda = 255$) which is the largest so far reported, at best of our knowledge, for planar all-polymer microcavities.[4-6, 20, 75-76]

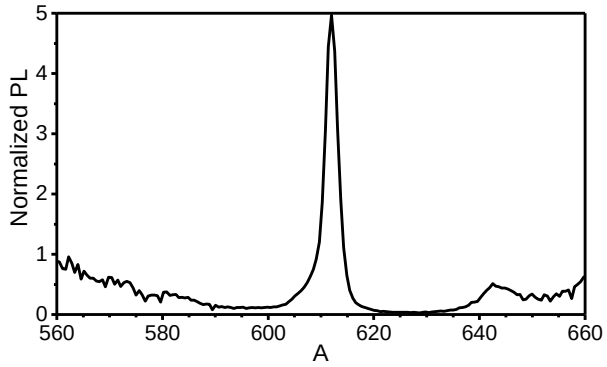

Fig. 4.12 Ratio between the microcavity and the reference PL spectra.

Density of photonic states modifications in microcavity

We have shown how the PL spectrum of the nanocomposite has been dramatically reshaped by the microcavity. Indeed, we observe a strong reduction of the intensity in the PBG spectral region and a strong increase at the cavity mode. This result agrees with previous findings obtained embedding emitters with broad PL spectra inside microcavities and indicates that spin coating allows to obtain finely tuned all-polymer microcavities.[75-76]
To explain the PL spectral redistribution we observe, we must introduce the well-known Fermi's golden rule. The traditional formula for the transition rate within the time-dependent weak perturbation approach is:

$$W(\omega) = \frac{2\pi}{\hbar} |< \boldsymbol{\mu} \cdot \mathbf{E} >|^2 \rho(\omega) \tag{4.2}$$

Where $\boldsymbol{\mu}$ is the transition dipole moment, $\mathbf{E}$ is the electric field, and $\rho(\omega)$ is the electronic density of final states. Inside a PhC, $\mathbf{E}$ is related to the allowed optical modes $\mathbf{E}_{n,\mathbf{k}}(\mathbf{r},\omega)$ within the dielectric lattice. Hence, the electric field must be treated as a series of modes, each contributing to the transition rate. Indeed, one must account for the number of photonic modes that allow the transition with energy $\hbar\omega$. This is done introducing the local density of photonic states (PDOS, $\rho_l(\mathbf{r},\omega)$):[75, 77-82]

$$\rho_l(\mathbf{r},\omega) = \frac{1}{(2\pi)^3} \sum_n \int d^3k \left|\boldsymbol{\mu} \cdot \mathbf{E}_{n,k}(\mathbf{r})\right|^2 \delta(\omega - \omega_{n,k}) \tag{4.3}$$

Where the space parameter is introduced in order to account for the spatial shape of the modes.
In the end, the transition rate, assumes the form:

$$W(\omega) = \frac{2\pi}{\hbar}\rho_l(\mathbf{r},\omega) \quad (4.4)$$

If we consider an emitter inside a homogeneous isotropic medium, the PDOS shows an ω^2 dependence as reported in chapter 1. In a microcavity, or in PhC in general, the PDOS spectral shape drastically changes.[77] At the PBG frequencies, $\rho_l(\mathbf{r},\omega)$ is negligible inside the crystal, while it is peaked for cavity modes energies. Consequently, the emitter PL spectrum (dictated by $W(\omega)$), which is dependent upon the spectral overlap between the "natural" emission of the material and the PDOS, is enhanced only in sharp spectral ranges and becomes suppressed for PBG energies. The intensity of the enhancement is related to the cavity modes volume, which mainly depend upon the dielectric contrast of the materials used to create the PhC.[61, 75]

Carefully observing eqs. 4.3 and 4.4, we notice that the number of modes inside a PhC depends upon the direction we are considering (due to the $\mathbf{k}$ dependence). Consequently, cavity emission assumes a directionality dictated by the PhC structure. In the case of DBRs, the dependence follows the exact same rules of the PBG, which shift toward higher energies as we consider angles further away from the normal to the crystal surface (Fig. 4.11).
This behavior is visible also in our sample. Fig. 4.10c and Fig. 4.13 shows the PL spectra as a function of the collection angle. For angle up to 15°, we observe almost no changes in PL intensity. As we observe angles over 15°, instead, we notice two main effects. The emission shifts toward higher energies and its peak intensity decreases. This can be easily explained in the above-mentioned framework. In fact, the emission is possible only where the PDOS is peaked. When the PDOS shifts, then, also the emission shifts. However, as this occurs, the spectral overlap between the photonic modes and the emitter spectrum reduces, reducing the PL intensity. In conclusion, in our sample, we introduced a dramatic change in the directionality of DiRs emission, which passes from an almost lambertian character, where the emission intensity is proportional to the cosine of the angle of emission, to a highly directional fluorescence given by the microcavity, which allows light propagation only along its axis.[80]

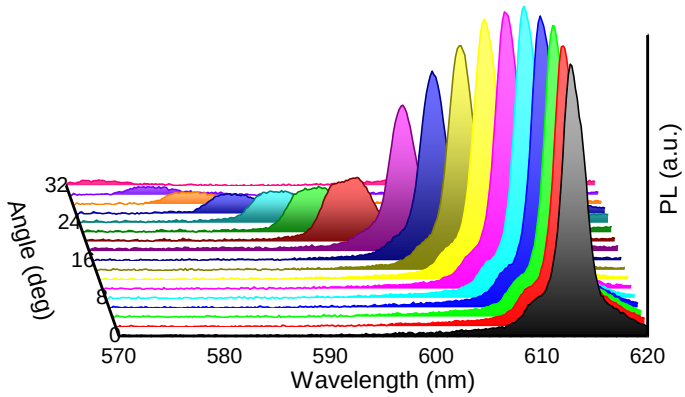

Fig. 4.13 Microcavity PL spectra as a function of the detection angle.

Integrating the microcavity PL intensity at normal detection over the full spectrum, we observe a ~25% reduction comparing to the reference. Hence, the overall emission is clearly not enhanced.[80] Since the geometry in the two measures is the same, this effect may be created by a reduction of emission efficiency. To better understand the reasons behind this reduction then, we executed PL QY measurements and observed that it is lower in the microcavity (6.5%) than in the reference (33%). To explain this result, we must account for the self-absorption caused by the relatively small (~10 nm) DiRs:PS nanocomposite Stokes shift. Indeed, as also observed in Fig. 4.9, the nanocomposite has a non-negligible extinction coefficient. This reduces PL intensity as emitted photons are reabsorbed. This phenomenon is strongly enhanced by the very long photon dwelling time inside the microcavity. Indeed, we can easily calculate the transit time of a photon inside a bare nanocomposite emitting layer accounting for the thickness and refractive index recurring to the simple formula $\tau_{dwell} = \frac{n_{cav} d_{cav}}{c}$. In the case of our reference layer, this time is in the order of 1 fs. Inside a microcavity, the dwelling time becomes higher since the DBR mirrors confine photons inside the defect layer. The time can be calculated using eq. 1.6 reported in chapter 1 and in the case of our microcavity is 83 fs. We can see that the dwelling time inside the microcavity is then extremely higher than the one inside the reference layer, hence the probability of self-absorption is greatly increased. The energy of each self-absorbed photon then, can be either re-emitted as another photon or be dispersed in non-radiative processes. In this way, self-absorption drastically reduces PL QY.

Lifetime modifications

The PDOS modifications operated by the microcavity should also modify emission lifetime. The radiative rate Γ_r is linked to emission lifetime by:

$$\tau_r^{-1} = \Gamma_r = \int d\omega \, W_r(\omega) \quad (4.5)$$

Therefore, enhancements in Γ_r also reduces emission lifetimes. To investigate this effect, we measured the PL decays for the nanocomposite reference film and for the microcavity using time correlated single photon counting (TCSPC) having time resolution of about 200 ps. TCSPC measures lifetimes observing the emission, hence the results depend upon the photons which are emitted. For a homogeneous emitter, the emission lifetime should be wavelength independent. In the case of inhomogeneous emitters, instead, we have that the PL is a collection of photons emitted by different processes and, unless extremely very special cases, spectral shifts in the various processes bring to a wavelength dependence. To account for these effects, we studied the cavity emission decay only for the defect mode wavelengths in the spectral range 610.5-615.5 nm (Fig. 4.14a). Compared to the reference, the microcavity PL decays slower for the initial 50 ns. For longer delays, instead, the two decays are similar. This behavior is clearly in contrast with the reduction of lifetime which we would have expected by a radiative rate enhancement.
To better understand these results, we fitted the decays by tri-exponential functions. The choice of a tri-exponential fit was dictated by simplicity reasons. Indeed, many different functional decays have been used in literature to describe the photophysics of single nanocrystals or highly controlled suspensions.[83-87] However, we decided to use a simple model in order to better understand the dynamics underlying the emission modifications. Table 4.2 summarizes both the lifetimes (τ_i) and the relative weights (A_i) extracted by the fits.

Table 4.2 Lifetime (τ_i) and relative intensity (A_i) of the different decays as deduced from the fitting procedure.

	τ_1 (ns)	A_1	τ_2 (ns)	A_2	τ_3 (ns)	A_3
Microcavity (613 nm)	6.7 ± 0.4	0.13 ± 0.04	12.0 ± 0.1	0.83 ± 0.04	40.3 ± 0.8	0.04 ± 0.03
Reference (613 nm)	6.4 ± 0.7	0.35 ± 0.05	13.2 ± 0.3	0.61 ± 0.06	43 ± 4	0.04 ± 0.01
Reference (600 nm)	5.2 ±0.5	0.56±0.06	13.1±1	0.42±0.07	56 ±5	0.02
Reference (630 nm)	-	0	12.6 ±0.6	0.86±0.02	51 ±3	0.14 ±0.02

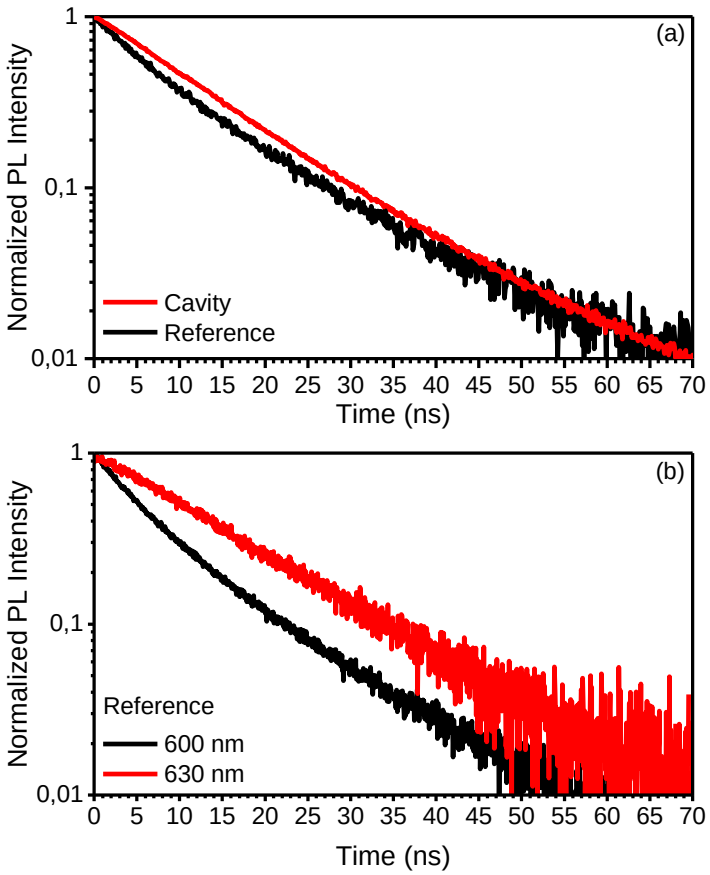

Fig. 4.14 (a) Normalized DIRs PL decay for microcavity (red line) and reference (black line). (b) Spectrally resolved decay for the reference: 600 nm, mainly peak1 component; 630 nm, mainly peak2 component

The long-living PL component (~40 ns) has a marginal role in each emission. This very weak contribution (few percents) can be assigned to surface traps and we discard it from further discussion.[88-89]

The two faster contributes are instead the ones having the major role and we assign them to the different emissions due to the DiRs size distribution we extracted before (Fig. 4.4 and Table 4.1). In order to understand which lifetime is related to which emission process, we studied the emission of the reference nanocomposite film at different wavelengths (we also report two of the measured decays in Fig. 4.14b). At 600 nm, the highest energy contribution to the PL is almost maximum (Fig. 4.4b) and the fast decay (5.2 ns) contributes for 56% to the decay (Table 4.2). At this wavelength, the slower decay (13.1 ns) weights only for 42%. On the other hand, at 630 nm we see that the fast component disappears while the slower one (12.6 ns) weight grows to 86% of the overall decay.

At 613 nm, in correspondence of the cavity mode, we observe that the relative weights of the fast and slow PL decay components (A_1 and A_2) are 35% and 61%, respectively. We can

compare them analyzing the deconvoluted DiRs PL spectrum (Fig. 4.4). Integrating the spectra in the range 610.5-615.5 nm, we observe that the weight of the two contribution is very similar to the one observed for the lifetimes (~35% for the short wavelength emission and ~ 65% for the long wavelength one). In light of all these observations, we assign the fast decay τ_1 to the short wavelength emission (608 nm) created by shorter DiRs while we assign the fast decay τ_2 to the long wavelength PL component (613 nm) related to DiRs with ~35 nm length. Another hint supporting this assignment is given by the fact that longer DiRs should have a better surface passivation due to the more developed CdS shell, hence reduced non-radiative recombination rate and longer lifetimes.[52-54]

Since we have discerned the various PL components, we are now able to discuss the modifications induced by the microcavity to the emission properties. The DiRs show a smaller τ_2 in microcavity than in the reference sample, while τ_1 is constant within the experimental uncertainty. The relative weight of the component with longer lifetime, A_2, drastically grows from 61 to 83% inside the microcavity while the fast component weight A_1 decreases from 35% to 13%. This different response is created by the unbalanced spectral overlap between the cavity mode and the two different emissions. We can expect an excellent overlap for the slow decay peaked at 617 nm while the overlap is reduced for the fast component peaked at 608 nm. We observe then a reduction of lifetime for the slow component from 13.2 to 12 ns. On the same time, this component intensity grows. The fast decay (~6 ns), instead, is spectrally shifted respect to the PDOS peak and the emission rate is not strongly modified. Then, the component retains the same lifetime.

These effects might suggest the presence of Purcell effect for the PL contribution given by longer DiRs. However, a reduction in τ_2 alone is not sufficient to prove it. Purcell effect is very difficult to observe.[90-91] Although photonic environment does modify emission processes, PL lifetime decrease may be brought also by increments in non-radiative decays rate introduced by microcavity growth. However, as previously discussed for the QY, we do not expect any change in the non-radiative recombination rate for DiR:PS nanocomposite since the cavity layer is prepared in the very same way of the reference one.

We then assume that the lifetime changes occur only in the radiative rates.[92] Additional work will be necessary to further support this interpretation.

References

(1) Lova, P.; Manfredi, G.; Boarino, L.; Comite, A.; Laus, M.; Patrini, M.; Marabelli, F.; Soci, C.; Comoretto, D., Polymer Distributed Bragg Reflectors for Vapor Sensing. *ACS Photonics* **2015,** *2*, 537-543.
(2) Lova, P.; Bastianini, C.; Giusto, P.; Patrini, M.; Rizzo, P.; Guerra, G.; Iodice, M.; Soci, C.; Comoretto, D., Label-Free Vapor Selectivity in Poly(p-Phenylene Oxide) Photonic Crystal Sensors. *ACS Appl. Mater. Interfaces* **2016,** *8*, 31941-31950.
(3) Lova, P.; Manfredi, G.; Boarino, L.; Laus, M.; Urbinati, G.; Losco, T.; Marabelli, F.; Caratto, V.; Ferretti, M.; Castellano, M.; Soci, C.; Comoretto, D., Hybrid ZnO:polystyrene nanocomposite for all-polymer photonic crystals. *Phys. Stat. Solidi C* **2015,** *12*, 158-162.
(4) Canazza, G.; Scotognella, F.; Lanzani, G.; De Silvestri, S.; Zavelani-Rossi, M.; Comoretto, D., Lasing from All-polymer Microcavities. *Laser Phys. Lett.* **2014,** *11*, 035804.
(5) Menon, V. M.; Luberto, M.; Valappil, N. V.; Chatterjee, S., Lasing from InGaP Quantum Dots in a Spin-coated Flexible Microcavity. *Opt. Express* **2008,** *16*, 19535-19540.
(6) Valappil, N. V.; Luberto, M.; Menon, V. M.; Zeylikovich, I.; Gayen, T. K.; Franco, J.; Das, B. B.; Alfano, R. R., Solution processed microcavity structures with embedded quantum dots. *Phot. Nano. Fund. Appl.* **2007,** *5*, 184-188.
(7) Komikado, T.; Yoshida, S.; Umegaki, S., Surface-emitting Distributed-feedback Dye Laser of a Polymeric Multilayer Fabricated by Spin Coating. *Appl. Phys. Lett.* **2006,** *89*, 061123.
(8) Knarr III, R. J.; Manfredi, G.; Martinelli, E.; Pannocchia, M.; Repetto, D.; Mennucci, C.; Solano, I.; Canepa, M.; Buatier de Mongeot, F.; Galli, G.; Comoretto, D., In-plane Anisotropic Photoresponse in All-polymer Planar Microcavities. *Polymer* **2016,** *84*, 383-390
(9) Moritsugu, M.; Kim, S.-n.; Kubo, S.; Ogata, T.; Nonaka, T.; Sato, O.; Kurihara, S., Photoswitching properties of photonic crystals infiltrated with polymer liquid crystals having azobenzene side chain groups with different methylene spacers. *React. Funct. Polym.* **2011,** *71*, 30-35.
(10) Moritsugu, M.; Ishikawa, T.; Kawata, T.; Ogata, T.; Kuwahara, Y.; Kurihara, S., Thermal and Photochemical Control of Molecular Orientation of Azo-Functionalized Polymer Liquid Crystals and Application for Photo-Rewritable Paper. *Macromol. Rapid Commun.* **2011,** *32*, 1546-1550.
(11) Park, T. J.; Hwang, S. K.; Park, S.; Cho, S. H.; Park, T. H.; Jeong, B.; Kang, H. S.; Ryu, D. Y.; Huh, J.; Thomas, E. L.; Park, C., Electrically Tunable Soft-Solid Block Copolymer Structural Color. *ACS Nano* **2015**.
(12) Chiang, Y.-W.; Chou, C.-Y.; Wu, C.-S.; Lin, E.-L.; Yoon, J.; Thomas, E. L., Large-Area Block Copolymer Photonic Gel Films with Solvent-Evaporation-Induced Red- and Blue-Shift Reflective Bands. *Macromolecules* **2015,** *48*, 4004-4011.
(13) Calvo, M. E.; Colodrero, S.; Hidalgo, N.; Lozano, G.; Lopez-Lopez, C.; Sanchez-Sobrado, O.; Miguez, H., Porous one dimensional photonic crystals: novel multifunctional materials for environmental and energy applications. *Energ. Environ. Sci.* **2011,** *4*, 4800-4812.
(14) Calvo, M. E.; Colodrero, S.; Rojas, T. C.; Anta, J. A.; Ocaña, M.; Míguez, H., Photoconducting Bragg Mirrors based on TiO_2 Nanoparticle Multilayers. *Adv. Funct. Mater.* **2008,** *18*, 2708-2715.
(15) Puzzo, D. P.; Scotognella, F.; Zavelani-Rossi, M.; Sebastian, M.; Lough, A. J.; Manners, I.;

Lanzani, G.; Tubino, R.; Ozin, G. A., Distributed Feedback Lasing from a Composite Poly(phenylene vinylene)−Nanoparticle One-Dimensional Photonic Crystal. *Nano Lett.* **2009,** *9*, 4273-4278.
(16) Lotsch, B. V.; Ozin, G. A., Photonic Clays: A New Family of Functional 1D Photonic Crystals. *ACS Nano* **2008,** *2*, 2065-2074.
(17) Jiménez-Solano, A.; Galisteo-López, J. F.; Míguez, H., Fine Tuning the Emission Properties of Nanoemitters in Multilayered Structures by Deterministic Control of their Local Photonic Environment. *Small* **2015,** *11*, 2727-2732.
(18) Song, H.; Singer, K.; Lott, J.; Wu, Y.; Zhou, J.; Andrews, J.; Baer, E.; Hiltner, A.; Weder, C., Continuous Melt Processing of All-polymer Distributed Feedback Lasers. *J. Mater. Chem.* **2009,** *19*, 7520-7524.
(19) Toray Picasus Product Presentation. http://www.toray.com/products/films/fil_012.html (accessed 2017/10/13).
(20) Hou, L.; Hou, Q.; Mo, Y.; Peng, J.; Cao, Y., All-organic flexible polymer microcavity light-emitting diodes using 3M reflective multilayer polymer mirrors. *Appl. Phys. Lett.* **2005,** *87*, 243504.
(21) Weber, M. F.; Stover, C. A.; Gilbert, L. R.; Nevitt, T. J.; A. J. Ouderkirk, Giant Birefringent Optics in Multilayer Polymer Mirrors. *Science* **2000,** *287*, 2451-2456.
(22) Kim, J. C.; Cakmak, M.; Zhou, X., Effect of Composition on Orientation, Optical and Mechanical Properties of Bi-axially Drawn PEN and PEN/PEI Blend Films. *Polymer* **1998,** *39*, 4225–4234.
(23) Ponting, M.; Hiltner, A.; Baer, E., Polymer Nanostructures by Forced Assembly: Process, Structure, and Properties. *Macromolecular Symposia* **2010,** *294*, 19-32.
(24) Goldenberg, L. M.; Lisinetskii, V.; Schrader, S., All-polymer Spin-coated Organic Vertical-cavity Surface-emitting Laser with High Conversion Efficiency. *Appl. Phys. B* **2015,** *120*, 271-277.
(25) Calvo, M. E.; Castro Smirnov, J. R.; Míguez, H., Novel approaches to flexible visible transparent hybrid films for ultraviolet protection. *J. Polym. Sci., Part B: Polym. Phys.* **2012,** *50*, 945-956.
(26) Fink, Y.; Winn, J. N.; Fan, S.; Chen, C.; Michel, J.; Joannopoulos, J. D.; Thomas, E. L., A Dielectric Omnidirectional Reflector. *Science* **1998,** *282*, 1679-1682.
(27) Goldenberg, L. M.; Lisinetskii, V.; Schrader, S., Fast and simple fabrication of organic Bragg mirrors - application to plastic microchip lasers. *Laser Phys. Lett.* **2013,** *10*, 055808.
(28) Radice, S. V.; Srinivasan, P.; Comoretto, D.; Gazzo, S. One-dimensional planar photonic crystals including fluoropolymer compositions and corresponding fabrication methods. 9 June 2016 (09.06.2016), 2016.
(29) Najda, S. P. An optoelectronic semiconductor device. EP 0795941A1, 12.03.1997, 1997.
(30) Ryan, H.; Maria, C. Photonic Polymer Multilayers for Colorimetric Radiation Sensing. US20160252625, 2016.
(31) Chang, J.-H. Method for manufacturing a reflective optical film. 2016.
(32) Bai, Z.; Joo, J.; Sung, I.-K.; Taylor, J. C. Multilayer Polymer Composite for encapsulating quantum dots. 2016.
(33) Goldenberg, L. M.; Lisinetskii, V.; Gritsai, Y.; Stumpe, J.; Schrader, S., Second Order DFB

Lasing using Reusable Grating Inscribed in Azobenzene-containing Material. *Opt. Mater. Express* **2012,** *2*, 11-19.
(34) Angeloni, I.; Raja, W.; Brescia, R.; Polovitsyn, A.; De Donato, F.; Canepa, M.; Bertoni, G.; Proietti Zaccaria, R.; Moreels, I., Disentangling the Role of Shape, Ligands, and Dielectric Constants in the Absorption Properties of Colloidal CdSe/CdS Nanocrystals. *ACS Photonics* **2016,** *3*, 58-67.
(35) Nasilowski, M.; Mahler, B.; Lhuillier, E.; Ithurria, S.; Dubertret, B., Two-Dimensional Colloidal Nanocrystals. *Chem. Rev.* **2016,** *116*, 10934-10982.
(36) Carbone, L.; Nobile, C.; De Giorgi, M.; Sala, F. D.; Morello, G.; Pompa, P.; Hytch, M.; Snoeck, E.; Fiore, A.; Franchini, I. R.; Nadasan, M.; Silvestre, A. F.; Chiodo, L.; Kudera, S.; Cingolani, R.; Krahne, R.; Manna, L., Synthesis and Micrometer-Scale Assembly of Colloidal CdSe/CdS Nanorods Prepared by a Seeded Growth Approach. *Nano Lett.* **2007,** *7*, 2942-2950.
(37) Chen, Y.; Vela, J.; Htoon, H.; Casson, J. L.; Werder, D. J.; Bussian, D. A.; Klimov, V. I.; Hollingsworth, J. A., "Giant" Multishell CdSe Nanocrystal Quantum Dots with Suppressed Blinking. *J. Am. Chem. Soc.* **2008,** *130*, 5026-5027.
(38) Christodoulou, S.; Vaccaro, G.; Pinchetti, V.; De Donato, F.; Grim, J. Q.; Casu, A.; Genovese, A.; Vicidomini, G.; Diaspro, A.; Brovelli, S.; Manna, L.; Moreels, I., Synthesis of Highly Luminescent Wurtzite CdSe/CdS Giant-shell Nanocrystals Using a Fast Continuous Injection Route. *J. Mater. Chem. C* **2014,** *2*, 3439-3447.
(39) Dai, X.; Zhang, Z.; Jin, Y.; Niu, Y.; Cao, H.; Liang, X.; Chen, L.; Wang, J.; Peng, X., Solution-processed, High-performance Light-emitting Diodes Based on Quantum Dots. *Nature* **2014,** *515*, 96-99.
(40) Nam, S.; Oh, N.; Zhai, Y.; Shim, M., High Efficiency and Optical Anisotropy in Double-Heterojunction Nanorod Light-Emitting Diodes. *ACS Nano* **2015,** *9*, 878-885.
(41) Yang, Y.; Zheng, Y.; Cao, W.; Titov, A.; Hyvonen, J.; Manders, J. R.; Xue, J.; Holloway, P. H.; Qian, L., High-efficiency Light-emitting Devices Based on Quantum Dots with Tailored Nanostructures. *Nat. Photonics* **2015,** *9*, 259-266.
(42) Lin, C. H.; Lafalce, E.; Jung, J.; Smith, M. J.; Malak, S. T.; Aryal, S.; Yoon, Y. J.; Zhai, Y.; Lin, Z.; Vardeny, Z. V.; Tsukruk, V. V., Core/Alloyed-Shell Quantum Dot Robust Solid Films with High Optical Gains. *ACS Photonics* **2016,** *3*, 647-658.
(43) Jiang, Y.; Oh, N.; Shim, M., Double-Heterojunction Nanorod Light-Emitting Diodes with High Efficiencies at High Brightness Using Self-Assembled Monolayers. *ACS Photonics* **2016,** *3*, 1862-1868.
(44) Grim, J. Q.; Christodoulou, S.; Di Stasio, F.; Krahne, R.; Cingolani, R.; Manna, L.; Moreels, I., Continuous-wave Biexciton Lasing at Room Temperature using Solution-processed Quantum Wells. *Nat. Nanotechnol.* **2014,** *9*, 891-895.
(45) Min, B.; Kima, S.; Okamoto, K.; Yang, L.; Scherer, A.; Atwater, H.; Vahalab, K., Ultralow Threshold On-chip Microcavity Nanocrystal Quantum Dot Lasers. *Appl. Phys. Lett.* **2006,** *89*, 191124.
(46) Dang, C.; Lee, J.; Breen, C.; Steckel, J. S.; Coe-Sullivan, S.; Nurmikko, A., Red, Green and Blue Lasing Enabled by Single-exciton Gain in Colloidal Quantum Dot Films. *Nat. Nanotechnol.* **2012**, 335-339.

(47) Schaefer, J.; Mondia, J. P.; Sharma, R.; Lu, Z. H.; Susha, A. S.; Rogach, A. L.; Wang, L. J., Quantum Dot Microdrop Laser. *Nano Lett.* **2012,** *8*, 1709-1712.
(48) Kelestemur, Y.; Cihan, A. F.; Guzelturk, B.; Demir, H. V., Type-tunable Amplified Spontaneous Emission from Core-seeded CdSe/CdS Nanorods Controlled by Exciton–exciton Interaction. *Nanoscale* **2014,** *6*, 8509-8514.
(49) Gollner, C.; Ziegler, J.; Protesescu, L.; Dirin, D. N.; Lechner, R. T.; Fritz-Popovski, G.; Sytnyk, M.; Yakunin, S.; Rotter, S.; Yousefi Amin, A. A.; Vidal, C.; Hrelescu, C.; Klar, T. A.; Kovalenko, M. V.; Heiss, W., Random Lasing with Systematic Threshold Behavior in Films of CdSe/CdS Core/Thick-Shell Colloidal Quantum Dots. *ACS Nano* **2015,** *9*, 9792-9801.
(50) Di Stasio, F.; Polovitsyn, A.; Angeloni, I.; Moreels, I.; Krahne, R., Broadband Amplified Spontaneous Emission and Random Lasing from Wurtzite CdSe/CdS "Giant-Shell" Nanocrystals. *ACS Photonics* **2016,** *3*, 2083-2088.
(51) Pu, C.; Peng, X., To Battle Surface Traps on CdSe/CdS Core/Shell Nanocrystals: Shell Isolation versus Surface Treatment. *J. Am. Chem. Soc.* **2016,** *138*, 8134-8142.
(52) Jones, M.; Lo, S. S.; Scholes, G. D., Quantitative Modeling of the Role of Surface Traps in CdSe/CdS/ZnS Nanocrystal Photoluminescence Decay Dynamics. *Proc. Natl. Acad. Sci. USA* **2009,** *106*, 3011-3016.
(53) Jones, M.; Kumar, S.; Lo, S. S.; Scholes, G. D., Exciton Trapping and Recombination in Type II CdSe/CdTe Nanorod Heterostructures. *J. Phys. Chem. C* **2008,** *112*, 5423-5431.
(54) Lin, W.; Niu, Y.; Meng, R.; Huang, L.; Cao, H.; Zhang, Z.; Qin, H.; Peng, X., Shell-thickness dependent optical properties of CdSe/CdS core/shell nanocrystals coated with thiol ligands. *Nano Res.* **2016,** *9*, 260-271.
(55) Zhou, R.; Stalder, R.; Xie, D.; Cao, W.; Zheng, Y.; Yang, Y.; Plaisant, M.; Holloway, P. H.; Schanze, K. S.; Reynolds, J. R.; Xue, J., Enhancing the Efficiency of Solution-Processed Polymer:Colloidal Nanocrystal Hybrid Photovoltaic Cells Using Ethanedithiol Treatment. *ACS Nano* **2013,** *7*, 4846-4854.
(56) Zavelani-Rossi, M.; Krahne, R.; Della Valle, G.; Longhi, S.; Franchini, I. R.; Girardo, S.; Scotognella, F.; Pisignano, D.; Manna, L.; Lanzani, G.; Tassone, F., Self-assembled CdSe/CdS nanorod micro-lasers fabricated from solution by capillary jet deposition. *Laser Photonics Rev.* **2012,** *6*, 678-683.
(57) Zavelani-Rossi, M.; Lupo, M. G.; Krahne, R.; Manna, L.; Lanzani, G., Lasing in Self-assembled Microcavities of CdSe/CdS Core/shell Colloidal Quantum Rods. *Nanoscale* **2010,** *2*, 931-935.
(58) Moreels, I.; Rainò, G.; Gomes, R.; Hens, Z.; Stöferle, T.; Mahrt, R. F., Nearly Temperature-Independent Threshold for Amplified Spontaneous Emission in Colloidal CdSe/CdS Quantum Dot-in-Rods. *Adv. Mater.* **2012,** *24*, OP231–OP235.
(59) Fischer, A.; Rollny, L.; Pan, J.; Carey, G. H.; Thon, S. M.; Hoogland, S.; Voznyy, O.; Zhitomirsky, D.; Kim, J. Y.; Bakr, O. M.; Sargent, E. H., Directly Deposited Quantum Dot Solids Using a Colloidally Stable Nanoparticle Ink. *Adv. Mater.* **2013,** *25*, 5742-5749.
(60) Di Stasio, F.; Grim, J. Q.; Lesnyak, V.; Rastogi, P.; Manna, L.; Moreels, I.; Krahne, R., Single-Mode Lasing from Colloidal Water-Soluble CdSe/CdS Quantum Dot-in-Rods. *Small* **2015,** *11*, 1328-1334.
(61) Comoretto, D., *Organic and Hybrid Photonic Crystals*. 1 ed.; Springer International

Publishing: Switzerland, 2015; p 497.
(62) Fogg, D. E.; Radzilowski, L. H.; Dabbousi, B. O.; Schrock, R. R.; Thomas, E. L.; Bawendi, M. G., Fabrication of Quantum Dot-Polymer Composites: Semiconductor Nanoclusters in Dual-Function Polymer Matrices with Electron-Transporting and Cluster-Passivating Properties. *Macromolecules* **1997,** *30*, 8433-8439.
(63) Zanella, M.; Gomes, R.; Povia, M.; Giannini, C.; Zhang, Y.; Riskin, A.; Bael, M. V.; Hens, Z.; Manna, L., Self-Assembled Multilayers of Vertically Aligned Semiconductor Nanorods on Device-Scale Areas. *Adv. Mater.* **2011,** *23*, 2205–2209.
(64) Arciniegas, M. P.; Stasio, F. D.; Li, H.; Altamura, D.; De Trizio, L.; Prato, M.; Scarpellini, A.; Moreels, I.; Krahne, R.; Manna, L., Self-Assembled Dense Colloidal Cu_2Te Nanodisk Networks in P3HT Thin Films with Enhanced Photocurrent. *Adv. Funct. Mater.* **2016,** *26*, 4535-4542.
(65) Li, G.; Tan, Z.-K.; Di, D.; Lai, M. L.; Jiang, L.; Lim, J. H.-W.; Friend, R. H.; Greenham, N. C., Efficient Light-Emitting Diodes Based on Nanocrystalline Perovskite in a Dielectric Polymer Matrix. *Nano Lett.* **2015,** *15*, 2640-2644.
(66) Rippa, M.; Capasso, R.; Mormile, P.; De Nicola, S.; Zanella, M.; Manna, L.; Nenna, G.; Petti, L., Bragg Extraction of Light in 2D Photonic Thue–Morse Quasicrystals Patterned in Active CdSe/CdS Nanorod–polymer Nanocomposites. *Nanoscale* **2013,** *5*, 331-336.
(67) Peng, S.; Zhang, R.; Chen, V. H.; Khabiboulline, E. T.; Braun, P.; Atwater, H. A., Three-Dimensional Single Gyroid Photonic Crystals with a Mid-Infrared Bandgap. *ACS Photonics* **2016,** *3*, 1131-1137.
(68) Komikado, T.; Inoue, A.; Masuda, K.; Ando, T.; Umegaki, S., Multi-layered mirrors fabricated by spin-coating organic polymers. *Thin Solid Films* **2007,** *515*, 3887-3892.
(69) Unger, K.; Resel, R.; Czibula, C.; C. Ganser; Teichert, C.; Jakopic, G.; Canazza, G.; S. Gazzo; Comoretto, D. In *Distributed Bragg reflectors: Morphology of cellulose acetate and polystyrene multila*, 6th International Conference on Transparent Optical Networks (ICTON 2014), Graz, Austria, Graz, Austria, 2014; pp 1-4.
(70) Fornasari, L.; Floris, F.; Patrini, M.; Comoretto, D.; Marabelli, F., Demonstration of fluorescence enhancement via Bloch surface waves in all-polymer multilayer structures. *PCCP* **2016,** *18*, 14086-14093.
(71) Comoretto, D.; Dellepiane, G.; Cuniberti, C.; Rossi, L.; Borghesi, A.; LeMoigne, J., Photoinduced absorption of oriented poly[1,6-di(N-carbazolyl)-2,4-hexadiyne]. *Phys. Rev. B* **1996,** *53*, 15653-15659.
(72) Comoretto, D.; Moggio, I.; Cuniberti, C.; Dellepiane, G.; Giardini, M. E.; Borghesi, A., Long-lived photoexcited states in polydiacetylenes with different molecular and supramolecular organization. *Phys. Rev. B* **1997,** *56*, 10264-10270.
(73) Moroni, L.; Salvi, P. R.; Gellini, C.; Dellepiane, G.; Comoretto, D.; Cuniberti, C., Two-photon spectroscopy of pi-conjugated polymers: The case of poly[1,6-bis(3,6-dihexadecyl-N-carbazolyl)-2,4-hexadiyne] (polyDCHD-HS). *J. Phys. Chem. A* **2001,** *105*, 7759-7764.
(74) Skorobogatiy, M.; Yang, J., *Fundamentals of Photonic Crystal Guiding*. Cambridge University Press: 2009.
(75) Frezza, L.; Patrini, M.; Liscidini, M.; Comoretto, D., Directional Enhancement of Spontaneous Emission in Polymer Flexible Microcavities. *J. Phys. Chem. C* **2011,** *115*, 19939-

19946.
(76) Gazzo, S.; Manfredi, G.; Poetzsch, R.; Wei, Q.; Alloisio, M.; Voit, B.; Comoretto, D., High refractive index hyperbranched polyvinylsulfides for planar one-dimensional all-polymer photonic crystals. *J. Polym. Sci., Part B: Polym. Phys.* **2016,** *54*, 73-80.
(77) Barth, M.; Gruber, A.; Cichos, F., Spectral and Angular Redistribution of Photoluminescence Near a Photonic Stop Band. *Phys. Rev. B* **2005,** *72*, 085129.
(78) Björk, G.; Machida, S.; Yamamoto, Y.; Igeta, K., Modification of spontaneous emission rate in planar dielectric microcavity structures. *Phys. Rev. A* **1991,** *44*, 669-681.
(79) Björk, G., On the spontaneous lifetime change in an ideal planar microcavity - transition from a mode continuuum to quantized modes. *IEEE J. Quantum Electron.* **1994,** *30*, 2314-2318.
(80) Schubert, E. F.; Hunt, N. E. J.; Micovic, M.; Malik, R. J.; Sivco, D. L.; Cho, A. Y.; Zydzik, G. J., Highly Efficient Light-Emitting Diodes with Microcavities. *Science* **1994,** *265*, 943-945.
(81) Liscidini, M.; Andreani, L. C., Photonic Crystals: An Introductory Survey. In *Organic and Hybrid Photonic Crystals*, Comoretto, D., Ed. Springer International Publishing: Switzerland, 2015; pp 3-29.
(82) Berti, L.; Cucini, M.; Di Stasio, F.; Comoretto, D.; Galli, M.; Marabelli, F.; Manfredi, N.; Marinzi, C.; Abbotto, A., Spectroscopic Investigation of Artificial Opals Infiltrated with a Heteroaromatic Quadrupolar Dye. *J. Phys. Chem. C* **2010,** *114*, 2403-2413.
(83) Rabouw, F. T.; Lunnemann, P.; van Dijk-Moes, R. J. A.; Frimmer, M.; Pietra, F.; Koenderink, A. F.; Vanmaekelbergh, D., Reduced Auger Recombination in Single CdSe/CdS Nanorods by One-Dimensional Electron Delocalization. *Nano Lett.* **2013,** *13*, 4884-4892.
(84) Galland, C.; Ghosh, Y.; Steinbruck, A.; Sykora, M.; Hollingsworth, J. A.; Klimov, V. I.; Htoon, H., Two types of luminescence blinking revealed by spectroelectrochemistry of single quantum dots. *Nature* **2011,** *479*, 203-207.
(85) Mallek-Zouari, I.; Buil, S.; Quélin, X.; Mahler, B.; Dubertret, B.; Hermier, J.-P., Plasmon assisted single photon emission of CdSe/CdS nanocrystals deposited on random gold film. *Appl. Phys. Lett.* **2010,** *97*, 053109.
(86) Schlegel, G.; Bohnenberger, J.; Potapova, I.; Mews, A., Fluorescence Decay Time of Single Semiconductor Nanocrystals. *Phys. Rev. Lett.* **2002,** *88*, 137401.
(87) Califano, M., Photoinduced Surface Trapping and the Observed Carrier Multiplication Yields in Static CdSe Nanocrystal Samples. *ACS Nano* **2011,** *5*, 3614-3621.
(88) Kaur, G.; Kaur, H.; Tripathi, S. K., Fluorescence Relaxation Dynamics of CdSe and CdSe/CdS Core/shell Quantum Dots. *AIP Conf. Proc.* **2014,** *1591*, 420-422.
(89) Jones, M.; Lo, S. S.; Scholes, G. D., Quantitative modeling of the role of surface traps in CdSe/CdS/ZnS nanocrystal photoluminescence decay dynamics. *PNAS* **2009,** *106*, 3011-3016.
(90) Gérard, J.-M.; Gayral, B., Strong Purcell Effect for InAs Quantum Boxes in Three-Dimensional Solid-State Microcavities. *J. Lightwave Technol.* **1999,** *17*, 2089-2095.
(91) Baba, T.; Sano, D., Low-Threshold Lasing and Purcell Effect in Microdisk Lasers at Room Temperature. *IEEE J. Sel. Topics Quantum Electron.* **2003,** *9*, 1340-1346.
(92) Manfredi, G.; Lova, P.; Di Stasio, F.; Krahne, R.; Comoretto, D., Directional Fluorescence Spectral Narrowing in All-Polymer Microcavities Doped with CdSe/CdS Dot-in-Rod

Nanocrystals. *ACS Photonics* **2017,** *4*, 1761-1769.

Chapter V

Lasing from polymer microcavities

Nowadays, lasers can be applied to a lot of different fields and their wide use requires the development of new simple and cost-effective fabrication methods for low power sources.[1-3] From this point of view, vertical cavity surface emitting lasers (VCSEL)[4] are very suited to cover the role of leading technology in this market.[5] A VCSEL is a planar microcavity formed by two dielectric mirrors embedding an opportunely engineered gain medium that can be possibly integrated into nanopillars. The high refractive index of materials composing the cavity with respect to the surrounding air gives rise to a remarkable lateral confinement.[6] This kind of structure is easy to produce and can be used for fiber communication systems, optical disk reading, laser printers, and sensing.[7-11] Currently, these systems require expensive and time consuming epitaxial manufactures to obtain high quality VCSELs based on crystalline emitters.[4, 12-13] Therefore, the possibility to use techniques like solution processing or extrusion is interesting to reduce the complexity of processes and to reduce the costs.[14] In this field, materials that can be processed by solution are attractive both for the development of tunable emitters and for the fabrication of photonic structures that act as resonators.[15-18] From the fabrication point of view, we already proved that high quality planar photonic crystals can be grown by spin-coating in a laboratory.[19-28] Indeed, lasing in all-polymer distributed Bragg reflectors and microcavities containing different gain media has already been demonstrated.[23, 29-31]

Another fundamental element of a lasing system is the emitting material. Colloidal semiconductor nanocrystals are appealing to be coupled with polymer systems given their nature. They can be integrated into solid-state devices through simple manufacturing techniques such as spin-, bar-, or dip- coating, which have been already used for polymers.[32-34] Moreover, they usually have high photoluminescence efficiencies and can be easily tuned for the application they are needed since their electronic and chemical-physical properties can be engineered via wet chemistry.[35-39] As a proof of their potential, NCs are already available for commercial purposes.[40] CdSe and CdSe/CdS systems are among the best performing NCs as already explained in chapter 4, and several research groups have already reported amplified spontaneous emission (ASE) and lasing from these materials.[32-34, 41-52]

In particular, we reported hybrid microcavities made of polymers doped with CdSe/CdS dot-in-rods (DiRs).[26] Chapter 4 is focused only on fluorescence enhancement and lifetimes modification. This was made possible by the use of a low concentration of DiRs in the nanocomposite emitting layer in order to prevent lasing action. Moreover, the DiRs did not present any light amplification effect.

This chapter reports on the fabrication of a polymer/DiRs VCSEL. In this work, we adopted a different strategy if compared with what is reported in chapter 4. Indeed, to increase the NCs density and achieve a low lasing threshold, we created a very dense layer of DiRs drop-

casting a liquid dispersion on a polymer DBR. Such approach, however, supplies a film of high rugosity and does not allow to continue the fabrication of the top DBR by spin-coating. Therefore, we prepared a second DBR separately, and pressed it on top of the first one to obtain the full optical resonator. This approach grants proof-of-concept VCSEL devices made of good quality dielectric mirrors.[23, 25-26, 53]
Throughout this chapter, we discuss the optical properties of this VCSEL and report on its lasing properties under fs-optical pumping. We also show a comparison with literature data revealing that our VCSEL can provide an interesting alternative to other common solutions when low power adaptable devices are needed.

Lasing

Laser stays for Light Amplification by Stimulated Emission of Radiation and this term either indicates a light beam created through a specific process or a device that creates such beam.
The theoretical basis behind lasing can be found in a paper published by Einstein in 1917[54] and will not be extensively reported here, however, we will briefly introduce the main phenomena underlying the process.
A light emitting material has three main ways to interact with photons of specific energy; it can absorb hitting photons, it can spontaneously emit photons (fluorescence), or it can emit photons under the stimulus of the light suitably accorded in frequency. Each transition is correlated with an electronic jump as reported in Fig. 5.1. The stimulated emission is the main responsible for lasing. It occurs when an electron is hit by a photon and decays to a lower energy level emitting another photon with the same frequency and phase of the one that started the process. In this way, the light that interact with the system is amplified.

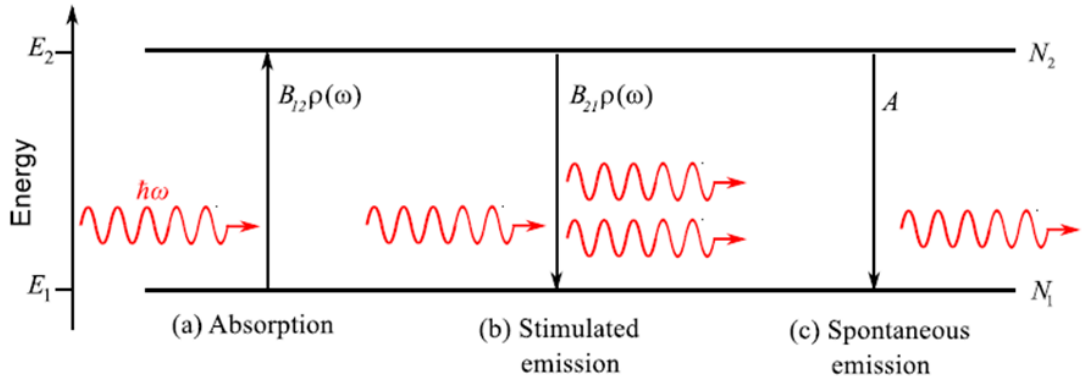

Fig. 5.1 Main interaction pathways of a photon with a two levels system.

Stimulated emission is concurrent with absorption and the probability that an excited electron can decay to a lower state by stimulated emission is exactly identical to the one that a ground electron can be promoted to excited state absorbing a photon.[54] When a material is hit by light then, the overall effect depends on the balance of population in the excited and ground states. If the ground state is more populated than the excited state, which is the normal condition of a material, the light will be absorbed, otherwise, it will be

amplified by stimulated emission. The equilibrium population for which the probability of absorption is identical to the one of stimulated emission is called population inversion and, in this condition, the material is completely transparent.
The reported case is a simplified one. The probability of transition depends also on the density of states and on other factors, however, the main concept behind light amplification is always the same.[55] In order to achieve light amplification, it is necessary to bring an high number of electrons to excited state. This is possible only if the system has three or more energetic levels (Fig. 5.2) and the injection of electrons in the excited state is called pumping.

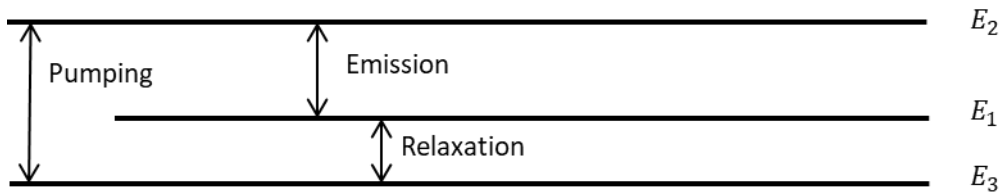

Fig. 5.2 Schematic representation of a three levels system with the main possible transitions.

A material which has been pumped over population inversion amplifies the light that hits it. Such amplification is restricted to specific wavelengths and is usually visible in amplified spontaneous emission measurements (ASE). Indeed, once population inversion is reached, the typical emission spectrum of the material shows a narrow peak which intensity grows with a superlinear behavior. The peak is created by the fraction of light that is spontaneously emitted by the material and then gets amplified. Since the transitions that allow population inversion are less than all the transitions that allow spontaneous emission, the ASE peak is necessarily sharper than the PL lineshape. The process can be extremely enhanced if the material is inserted inside an optical resonator like the one shown in Fig. 5.3. The light is continuously reflected inside the resonator and is amplified multiple times as it crosses the material which is held in population inversion conditions. Eventually, photons can come out of the resonator through a semireflective mirror. The light spectral linewidth is strongly reduced and the outgoing beam is highly collimated and intense. Due to the almost monochromaticity of laser, the light is also extremely coherent both temporally and spatially, which means that the light preserves its phase properties even at long distances and for different times.

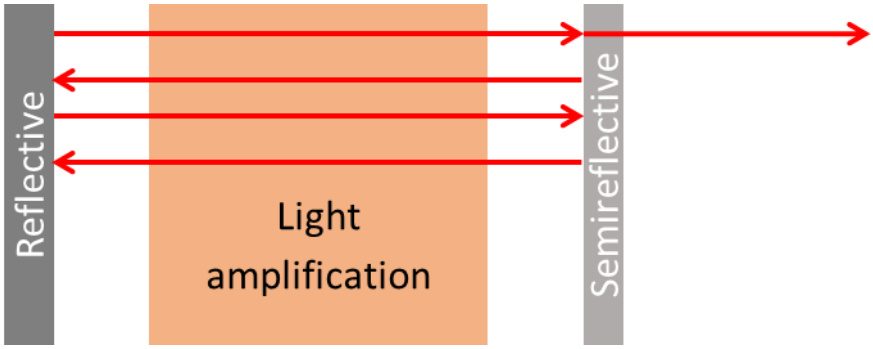

Fig. 5.3 Schematic representation of a lasing device.

Analysis of the DiRs used to obtain lasing

We used colloidal nanocrystals as gain material inside our microcavity. Such particles are CdSe/CdS DiRs similar to the one of chapter 4 but possessing intrinsic ASE, differently from them. They were synthetized according to an already published procedure[56] starting from CdSe cores with 4 nm diameter.

Fig. 5.4a shows a transmission electron microscopy (TEM) image of the DiRs used in this work. The DiRs have an almost conical shape and we studied their size distribution in length and diameter. Fig. 5.4b shows DiRs size distribution histograms obtained by TEM image analysis of 100 DiRs. The average length is 17 ± 3 nm while the mean base diameter is 5 ± 1 nm. The DiRs population seems to be more monodisperse if compared to the one of DiRs already reported in chapter 4.

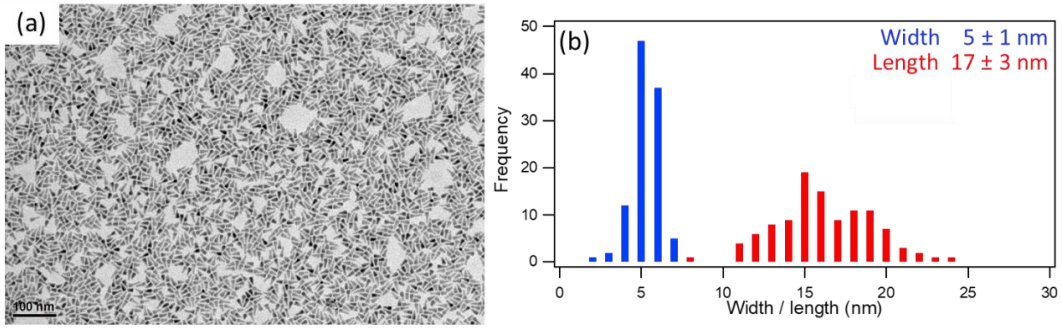

Fig. 5.4 (a) TEM image of DiRs used in this study. (b) Histograms showing statistics of the DiR length (in red) and diameter (in blue).

We created a reference NCs film drop-casting a DiRs solution in toluene (10 g/l, 200 µl) over a cellulose acetate (CA) layer. After the deposition, the solvent was left to evaporate for 2 hours.

Fig. 5.5 reports the absorbance (black) and continuous wave (CW) photoluminescence (PL) (red) spectra of the drop-cast DiRs film. The absorbance spectrum is afflicted by a light scattering background induced by the roughness of the film. Nonetheless, it clearly shows two peaks at about 625 and 595 nm. We assign them to CdSe cores electronic transitions.[56]

The shoulder at ~520 nm originates instead from the CdS shell. The CW PL spectrum of the DiRs film displays a single Voigt-shaped peak[26] with full width half maximum (FWHM) of 27 nm, corresponding to 82 meV. This single peak is comparable to the one of the NCs used in chapter 4 but no deconvolution in more emissions is needed this time. Indeed, such analysis may probably be done but is completely superfluous to the purpose of this work. The PL peak is centered at 639 nm and shows a 14 nm Stokes shift.

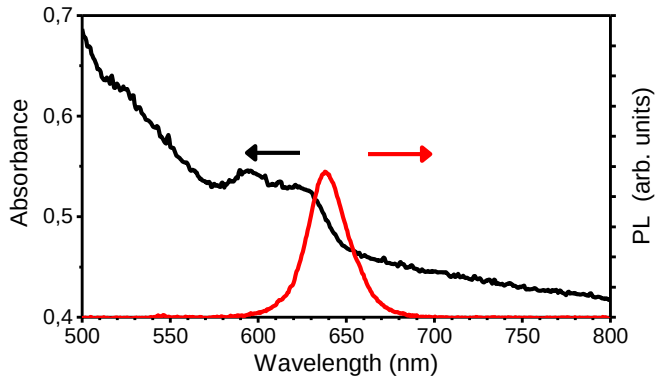

Fig. 5.5 Absorbance (black) and CW PL (red) of a DiRs reference film.

To investigate if the DiRs show light amplification, which is a necessary pre-requisite to obtain lasing from the active material in a suitable optical cavity, in Fig. 5.6a we report the emission of the reference film under fs pumping for different fluences. The measure were carried out using a Ti:sapphire laser (Coherent Legend Elite seeded by a Ti:sapphire fs laser, λ = 405 nm, 70 fs pulse FWHM and repetition rate of 1 kHz) for excitation, and an Ocean Optics HR4000 spectrometer coupled to an optical fibre for collection. The excitation beam was focused with a cylindrical lens onto the sample, thus obtaining a stripe-shaped beam profile. The collection was executed at ~90° respect to the excitation beam. For fluences lower than 280 μJ/cm^2, we observe a single broad PL peak centered at 646 nm. We report in Fig. 5.7 a comparison between a normalized fs spectrum and a CW one. The FWHM of the two emissions is almost unvaried but the fs peak is 6 nm red-shifted compared to the CW one. This red-shift may be ascribed to the different measurement geometry; indeed, in the CW measurements the PL is collected at normal incidence. In the fs conditions, instead, the longer optical path in the nanocrystal film increases self-absorption effects, and results in a spectral shift.

For fluences larger than 280 μJ/cm^2, a new sharp peak is detected at 640 nm and becomes dominant with increasing excitation power density. This peak is 6 nm wide, ~1/4 of the low power density PL emission. Fig. 5.6b shows the emission intensity at 640 nm (black squares) and at 660 nm (red squares) for different pumping fluences. At 660 nm, the PL intensity grows linearly and represent the DiRs PL. The intensity at 640 nm, instead, shows two different regimes: under weak pumping (below ~280 μJ/cm^2) the intensity increases linearly with a small slope and, once a certain threshold is reached, the slope dramatically increases. This behavior is typical of ASE and we can ascribe the 640-nm peak to the light

amplification given by the reaching of population inversion. Comparing the emission intensity for weak and strong excitation fluence we can set the ASE threshold at ~230 μJ/cm^2, in agreement with previous observations on similar systems.[32]

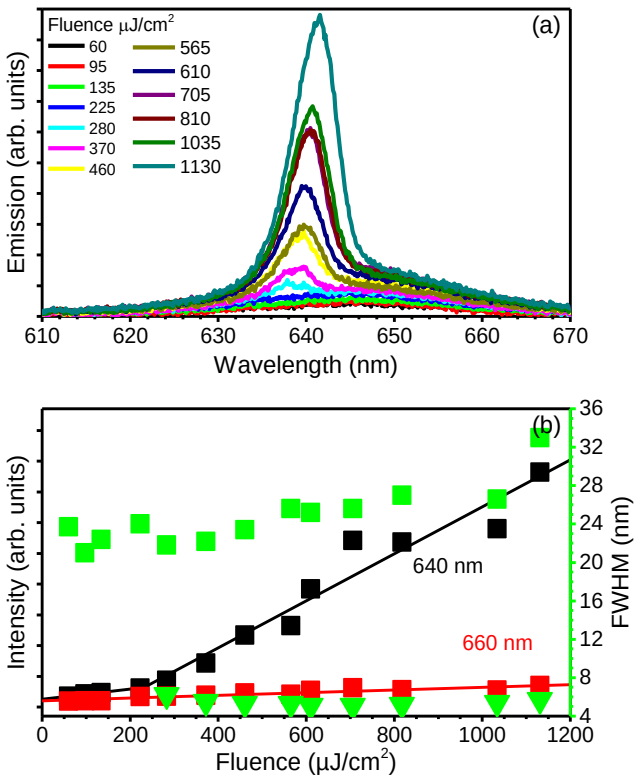

Fig. 5.6 (a) DiRs film emission spectra as a function of fs-pumping fluence; (b) Emission intensity at 640 (black squares) and 660 nm (red squares) as a function of excitation fluence. In green, the FWHM of the emission components. In squares is the PL background and in triangles is the emerging peak.

Fig. 5.6b also shows the FWHM of the two emission components. The values have been obtained fitting the spectra with two Lorentz-shaped curves. The green squares are indicative of the PL created by spontaneous emission and have an almost constant value of FWHM=26 nm. The green triangles, which are present only for fluences over the threshold, indicate the width of the ASE peak. They assume an almost constant value of 5-6 nm.

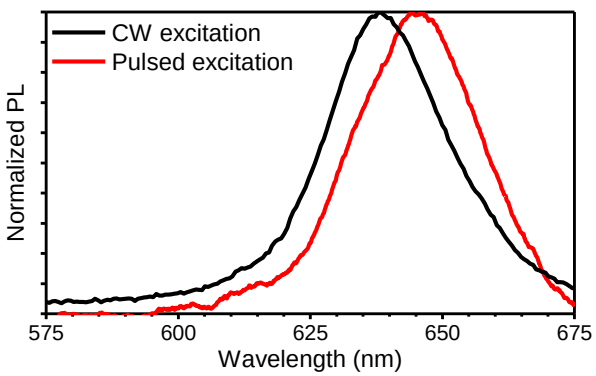

Fig. 5.7 Normalized PL of the DiRs film under CW (black) and pulsed fs excitation (red).

Microcavity production and optical characterization

Once we were sure that the DiRs do amplify light, we created the photonic structure that works as VCSEL as schematically shown in Fig. 5.8.

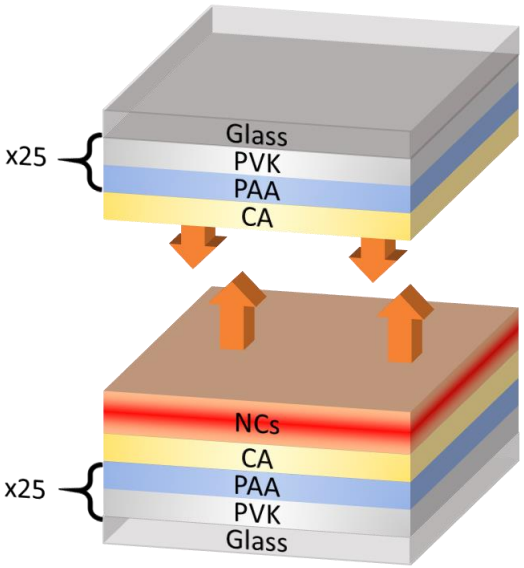

Fig. 5.8 Sketch of the microcavity structure, which consist of two polymer DBRs sandwiching one DirS layer.

The planar microcavity has been prepared by sandwiching two identical polymer DBRs, one of which was covered by a drop-cast DiRs film. The DBRs were made of twenty-five alternated bilayers of polyacrylic acid (PAA) and polyvinylcarbazole (PVK) grown by spin coating solutions in 4-methyl-2-pentanol (40 g/l, for PAA) and in toluene (40 g/l, for PVK) at 8400 rpm on top of a 20x20 mm^2 coverslip glass substrate. PVK and PAA, as already explained in chapter 2, are a polymer pair suitable to create high optical quality DBRs by spin coating.[57] We spin coated a capping layer of cellulose acetate (CA) at 2400 rpm from a

solution in diaceton alcohol (35 g/l) over each DBR and we annealed them at 60°C for 10 minutes. We drop-cast a DiRs solution in toluene (around 10 g/l, 200 µl) on one DBR and left the solvent to evaporate for 2 hours. After this step, the second DBR was pressed on top of the first one, thus creating the planar microcavity.
Fig. 5.9 reports the microcavity reflectance spectra measured on six different spots over the sample surface. The six spectra show minor differences, proving the homogeneity of the DBR mirrors employed to build the planar microcavity. The microcavity spectrum shows a broad and rectangular shaped reflectance peak in the spectral range 605-645 created by the PBG. Its FWHM is 37 nm, in agreement with the one obtained using the relations expressed in chapter 1 and considering n_{PVK}=1.66 and n_{PAA}=1.51 as found in literature and shown in chapter 2.[57-60]

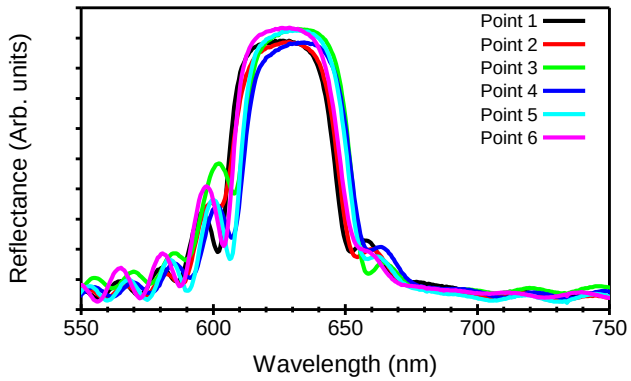

Fig. 5.9 Reflectance of the microcavity recorded at different spots on its surface.

The PBG is narrower than the PL peak of the DiRs (ranging from 620 to 670 nm) but completely covers the ASE peak (Fig. 5.6), thus creating a functional resonator. The reflectance spectra do not show any cavity mode. This is unusual and probably owed to the scarce homogeneity in the DiRs layer. We report in Fig. 5.10 confocal fluorescence microscopies of the DiRs film. The fluorescence images were recorded with a NIKON A1 confocal microscope with a 10x objective, under excitation with a laser at 402 nm. The emission was detected in the range from 590-650 nm.
The layers are evidently inhomogeneous and very different densities are present throughout the surface. Moreover, from the xyz scan we can estimate the thickness of the cavity layer to be around 5-10 µm.

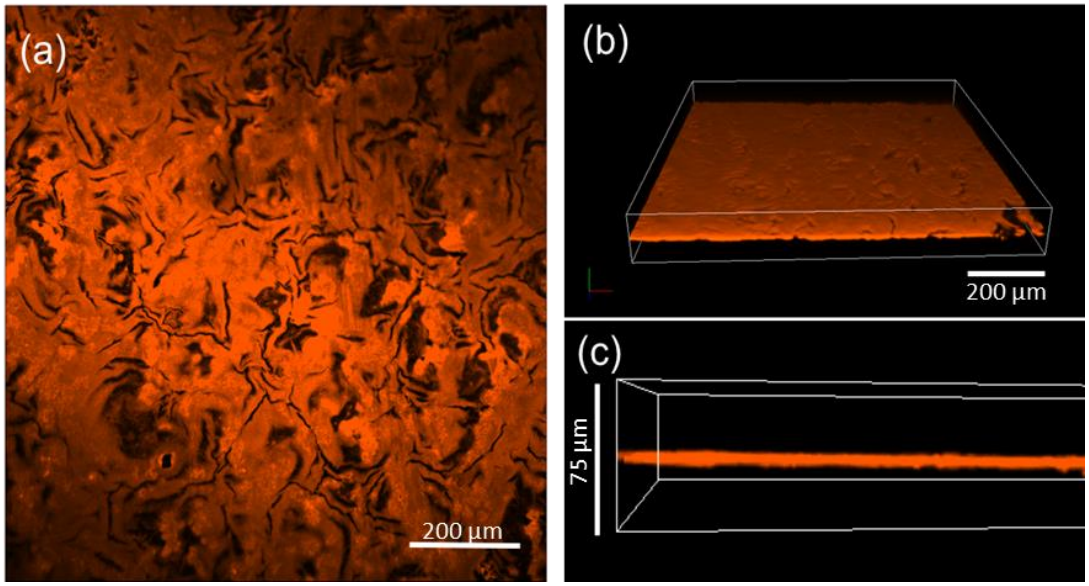

Fig. 5.10 Confocal fluorescence microscopy images of the DiRs film recorded from a reopened microcavi-ty. (a) Top view, (b-c) 3D representation of stacked images recorded in a xyz scan at different viewing angles. Scale bars correspond to 200 µm in (a-b), and to 75 µm in (c).

Fig. 5.11 shows the normalized CW PL spectra of the microcavity (red curve) and of the reference (black curve). In the microcavity, the PL of the DiRs is suppressed in correspondence of the PBG between 600 and 640 nm and nearly unchanged outside this range. Another weak peak is visible in correspondence of the PL tail at 595 nm. This signal is better visible in the rescaled microcavity spectrum.

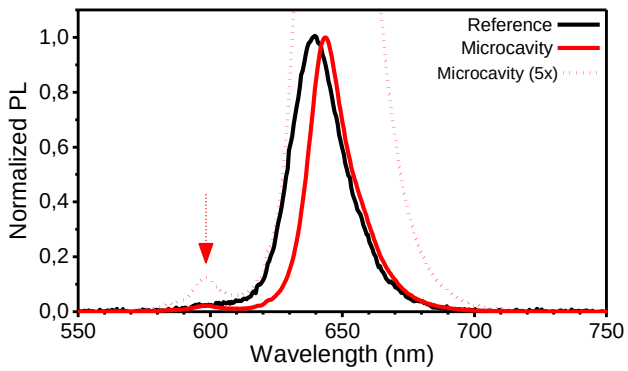

Fig. 5.11 PL spectra of the DiRs film (black line) and microcavity (red line) under CW excitation. The arrow indicates the weak peak at the PBG edge in the microcavity PL spectrum (magnified x5, red dotted line).

Such a small spectral variation between the two PL is hardly comparable with the emission reshaping usually induced by planar microcavities.[23, 26, 57] Indeed, a great difference may be

seen if compared to the case of chapter 4. The absence of a cavity mode is related to the inhomogeneity of the DiRs layer which introduces scattering losses and hinders the formation of cavity modes in CW PL experiments.
The inhomogeneity of the sample also introduces different responses of the sample under fs excitation for investigation over different spots. Some areas show only ASE while others clearly show lasing.

ASE in the microcavity

Fig. 5.12a reports the emission spectra under fs excitation from an area of the microcavity sample that only shows ASE. This effect is due to the relatively low homogeneity of the DiRs layer. For low fluences, the emission is similar to the one under CE excitation reported in Fig. 5.11. As the fluence increases, this signal increases too and, over 110 $\mu J/cm^2$, a sharp high energy shoulder starts growing at 640 nm. The new structure is very similar to the ASE shown for a bare DiRs film in Fig. 5.6. Therefore, we assign this peak to ASE filtered by the microcavity PBG.
Interestingly, these spectra also show a new peak for fluences larger than 400 $\mu J/cm^2$. This peak is centered at 594 nm, outside of the PBG, and strongly gains in intensity with increasing fluence. Its position is comparable to one of the DiRs two absorption peaks shown in Fig. 5.5. Hence, we assign this new ASE signal to higher energy optical transitions.
Fig. 5.12b shows the fluence dependence of emission intensity at different wavelengths (595, 640 and 660 nm). These are representative of different phenomena: the intensity at 660 nm indicates the DiRs spontaneous emission, the intensity at 640 nm indicates the ASE peak, and the intensity at 595 nm indicates the higher energy transition ASE which we were not able to see for a bare DiRs film. At 640 nm, the increase of the signal is linear with a slope of 10.2 $cm^2\ \mu J^{-1}$ up to 320 $\mu J/cm^2$. After this fluence, the intensity saturates. The high-energy part of the emission, instead, initially grows linearly with a slope comparable to that of the spontaneous emission. However, after 400 $\mu J/cm^2$, the slope rises to 4.8 $cm^2\ \mu J^{-1}$. This behavior gives a further indication of ASE from higher energy transitions which is confirmed also by some studies on similar giant shell core-shell nanocrystals.[45]

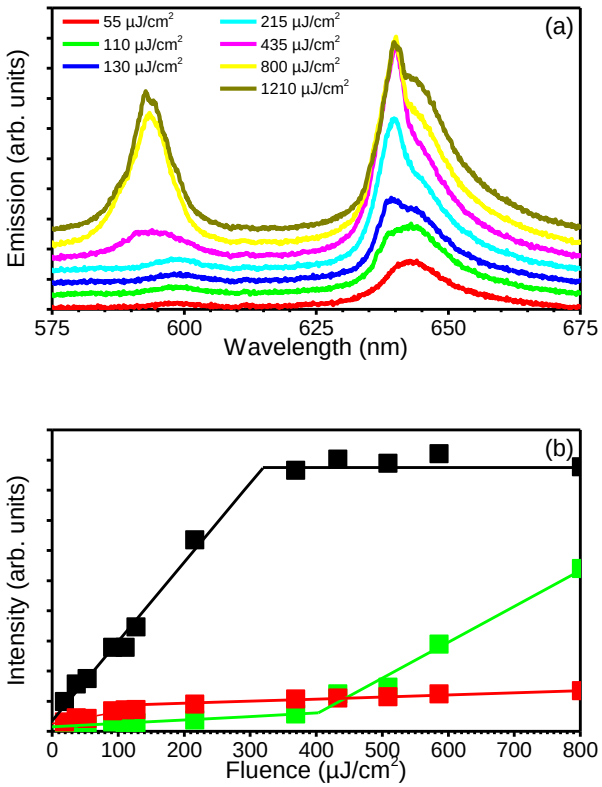

Fig. 5.12 (a) fs PL spectra recorded from the microcavity as a function of pumping fluence from a region that does not manifest lasing; (b) Emission intensity at different wavelengths as a function of the pumping fluence (594 nm, high energy PL, in green; 640 nm, corresponding to the microcavity PL maximum, in black; 660 nm, related to the bare DiRs PL, in red).

Lasing in the microcavity

Fig. 5.13 shows the microcavity emission spectra collected at different excitation fluences in a spot showing lasing.

At the lowest measured pumping fluence (25 μJ/cm^2), the emission shape is different from the CW one shown in Fig. 5.11. We observe several peaks between 635 and 645 nm, which are more visible in the magnified scale plot of Fig. 5.13b. Increasing the pumping fluence to 55 μJ/cm^2, three sharp peaks located at 635 nm, 637 nm, and 640 nm become more distinguishable. Moreover, at this fluence, a second background PL signal modulated by the PBG starts growing. This background signal is similar to the one reported for CW pumping. As fluence increases the peak positioned at 640 nm grows faster compared to the other ones and then becomes dominant. The FWHM of this structure is ~1 nm, which is however limited by the spectrometer resolution.

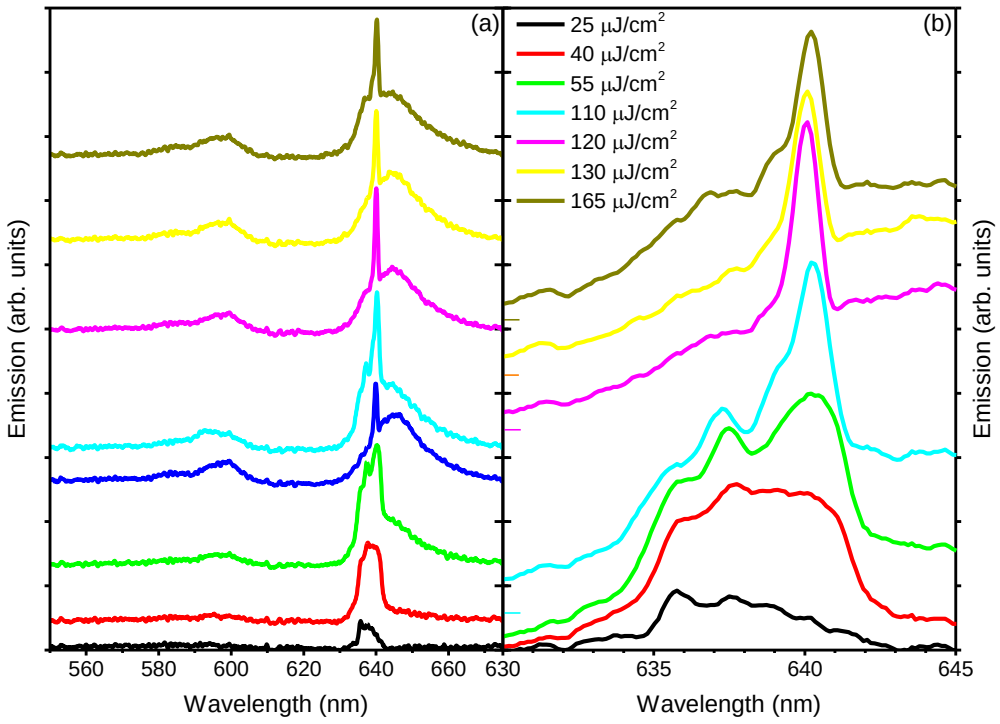

Fig. 5.13 (a) Stacked fs emission spectra of the microcavity collected perpendicular (normal angle) to the sample surface for different pumping fluences. (b) Spectra of panel (a) on a magnified scale.

Fig. 5.14 compares the intensity of the 640-nm peak with the one collected at 660 nm for different fluences. The latter is associated to the DiRs PL (red dots) and increases linearly with the excitation power density with a slope of 1.8 cm^2 μJ^{-1}. This value agrees and is comparable (since the measures were taken with the same geometry and conditions) with the data retrieved in Fig. 5.12 for the spots of the sample showing only ASE (1.6 cm^2 μJ^{-1}). The intensity of the lasing peak at 640 nm, instead, increases with a steeper slope of 38.8 cm^2 μJ^{-1}, before saturating at ~60-70 $\mu J/cm^2$. This behavior, together with the FWHM, which is 6 times sharper than the ASE peak, allow us to assign the peak to lasing.

In our measures, the emission spectra always contain lasing modes, even at the lowest fluence used. The lasing peaks grow at different rates with fluence until the signal at 640 nm becomes dominant. This effect may be induced by gain spectral hole-burning, typical of materials showing inhomogeneous broadening.[61]

Since we were not able to measure spectra not showing peaks, we consider 25 $\mu J/cm^2$ as an upper limit for our microcavity lasing threshold.

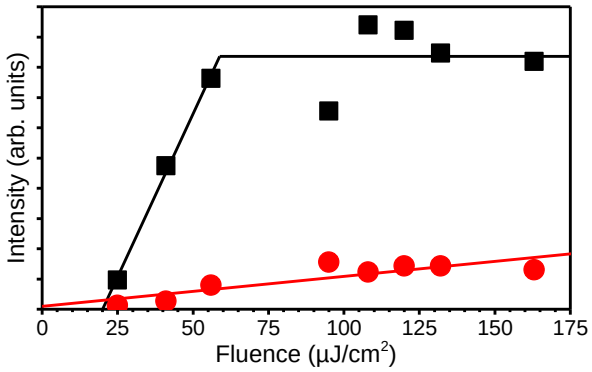

Fig. 5.14 Microcavity emission intensity at 640 nm (black squares) and 660 nm (red circles) against the pump fluence.

Another important suggestion of lasing is given by measures for normal and off-axis detection respect to the sample. Indeed, Fig. 5.15 shows two spectra of the microcavity emission. Both are recorded under fs excitation for fluences above lasing threshold but in one case the light is collected off-axis (black line) while in the other is collected at normal angle from the sample (red line). While for normal incidence there is a clear laser emission at 640 nm, for off-axis collection, the emission spectrum only shows the features typical of CW PL. These proves the directionality of the emission given by the planar resonator and allows to exclude random lasing which is not directional.[62-63]

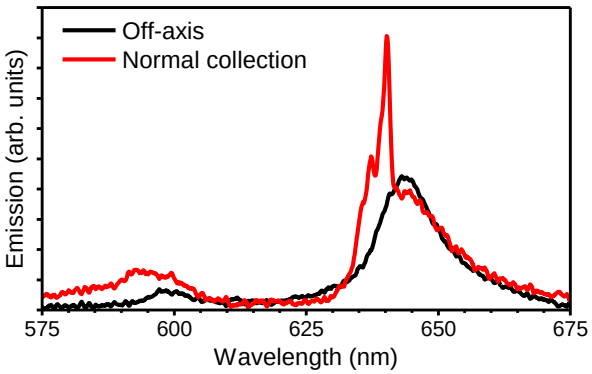

Fig. 5.15 Microcavity emission spectra under fs pumping at 108 μJ/cm² collected at normal angle from the sample (red) and off-axis (black).

The multipeak structure we observe at low fluencies can help us to better understand the photonic structure properties. Indeed, we can treat the microcavity as a Fabry-Perot etalon and suppose that each peak in the emission spectra is created by a resonator mode. Then,

the optical length of the cavity can be estimated by the free spectral range $\Delta\lambda_{fsr}$, which is the difference in wavelength between the resonator modes. From Fig. 5.13 we obtain the distance between neighboring peaks as ~2nm. Considering this as the free spectral range of the resonator we can then estimate the cavity optical length (d) from:[61, 64]

$$\Delta\lambda_{\mathrm{fsr}} = \frac{\lambda^2}{2\mathrm{nd}} \tag{5.1}$$

Being $\lambda = 640\,nm$ and $\Delta\lambda_{fsr} = 2\,nm$, we obtain an optical length $nd = 102\ \mu m$. For a DiRs refractive index of 2.5,[39] we can then estimate a geometrical thickness of 41 μm. This value is much larger than what we measured with confocal fluorescence on the central region of the film. One possible explanation is that the optical path we estimate considers in reality also empty regions, which are created by thicker nanocrystal aggregates that act as spacers. We notice however that a similar DiRs film thickness was reported in ref.[34] for a comparable fabrication process.

The lasing threshold we obtained for our microcavity is in agreement with the one reported for coffee-ring resonators made of similar DiRs[32] and well compares with the one of similar all-organic microcavities.[23, 65-66] The threshold, however, is few orders of magnitude lower than what has been reported for spin coated VCSEL containing NCs.[29] In literature, lower thresholds are reported only for inorganic planar microcavity, where the larger dielectric contrast helps in getting better light confinment[67-71] and for more complicated resonators like microdisks.[72-73]

In conclusion, the VCSEL we prepared shows lasing with pumping threshold below 25 $\mu J/cm^2$ which is one of the lowest value reported so far for polymer-NCs systems.[74]

This is a preliminary step in the development of free-standing lasers that are easily tunable over a wide spectral range and adaptable to photonic devices where low-power and simple structures are desired.

References

(1) Tan, Z.; Yang, C.; Zhu, Y.; Xu, Z.; Zou, K.; Zhang, F.; Wang, Z., High Speed Band-Limited 850-nm VCSEL Link Based on Time-Domain Interference Elimination. *IEEE Photon. Technol. Lett.* **2017,** *29*, 751-754.
(2) Sheffi, N.; Sadot, D., Energy-Efficient VCSEL Array Using Power and Offset Allocation of Spatial Multiplexing in Graded-Index Multimode Fiber. *J. Lightwave Technol.* **2017,** *35*, 2098-2108.
(3) Pavan, S. K.; Lavrencik, J.; Ralph, S. E., VCSEL-Based PAM-4 Links up to 62 Gbit/s Over OM3, OM4, and WB-MMF: Performance Comparison at 850 nm and 1050 nm. *J. Lightwave Technol.* **2017,** *35*, 1614-1623.
(4) Haruhisa, S.; Ken-ichi, I.; Chiyuki, K.; Yasuharu, S., GaInAsP/InP Surface Emitting Injection Lasers. *Jpn. J. Appl. Phys.* **1979,** *18*, 2329.
(5) Koyama, F., Recent Advances of VCSEL Photonics. *J. Lightwave Technol.* **2006,** *24*, 4502-4513.
(6) Scofield, A. C.; Kim, S.-H.; Shapiro, J. N.; Lin, A.; Liang, B.; Scherer, A.; Huffaker, D. L., Bottom-up Photonic Crystal Lasers. *Nano Lett.* **2011,** *11*, 5387-5390.
(7) Hu, B.; Jin, G.; Liu, T.; Wang, J., A Precision Fiber Bragg Grating Interrogation System using Long-wavelength Vertical-cavity Surface-emitting Laser. *Photonic Sensors* **2016,** *6*, 351-358.
(8) Chang-Hasnain, C. J., Tunable VCSEL. *IEEE J. Sel. Topics Quantum Electron.* **2000,** *6*, 978-987.
(9) Vahala, K. J., Optical Microcavities. *Nature* **2003,** *424*, 839-846.
(10) Mizunami, T.; Yamada, T.; Tsuchiya, S., Interrogation of fiber-Bragg-grating temperature and strain sensors with a temperature-stabilized VCSEL. *Opt. Rev.* **2016,** *23*, 703-707.
(11) Iga, K., Surface-emitting laser-its birth and generation of new optoelectronics field. *IEEE J. Sel. Topics Quantum Electron.* **2000,** *6*, 1201-1215.
(12) Jatta, S.; Zogal, K.; Kögel, B.; Haberle, K.; Sydlo, C.; Meissner, P., Realization of Tunable Optical Components with ICP-CVD. *Frequenz* **2008,** *62*, 96-99.
(13) Breiland, W. G.; Allerman, A. A.; Klem, J. F.; Waldrip, K. E., Distributed Bragg Reflectors for Vertical-Cavity Surface-Emitting Lasers. *MRS Bull.* **2011,** *27*, 520-524.
(14) Andrews, J. H.; Crescimanno, M.; Dawson, N. J.; Mao, G.; Petrus, J. B.; Singer, K. D.; Baer, E.; Song, H., Folding flexible co-extruded all-polymer multilayer distributed feedback films to control lasing. *Opt. Express* **2012,** *20*, 15580-15588.
(15) Song, H.; Singer, K.; Lott, J.; Wu, Y.; Zhou, J.; Andrews, J.; Baer, E.; Hiltner, A.; Weder, C., Continuous Melt Processing of All-polymer Distributed Feedback Lasers. *J. Mater. Chem.* **2009,** *19*, 7520-7524.
(16) L. Hou, Q. H., Y. Mo, J. Peng, and Y. Cao, All-organic Flexible Polymer Microcavity Light-emitting Diodes using 3M Reflective Multilayer Polymer Mirrors. *Appl. Phys. Lett.* **2005,** *87*, 243504.
(17) Weber, M. F.; Stover, C. A.; Gilbert, L. R.; Nevitt, T. J.; Ouderkirk, A. J., Giant Birefringent Optics in Multilayer Polymer Mirrors. *Science* **2000,** *287*, 2451.
(18) Lee, J.-H.; Koh, C. Y.; Singer, J. P.; Jeon, S.-J.; Maldovan, M.; Stein, O.; Thomas, E. L., 25th Anniversary Article: Ordered Polymer Structures for the Engineering of Photons and Phonons. *Adv. Mater.* **2014,** *26*, 532-569.
(19) Comoretto, D., *Organic and Hybrid Photonic Crystals*. 1 ed.; Springer International

Publishing: Switzerland, 2015; p 497.
(20) Gazzo, S.; Manfredi, G.; Pötzsch, R.; Wei, Q.; Alloisio, M.; Voit, B.; Comoretto, D., High Refractive Index Hyperbranched Polyvinylsulfides for Planar One-dimensional All-polymer Photonic Crystals. *J. Polym. Sci., Part B: Polym. Phys.* **2016,** *54*, 73-80.
(21) Lova, P.; Bastianini, C.; Giusto, P.; Patrini, M.; Rizzo, P.; Guerra, G.; Iodice, M.; Soci, C.; Comoretto, D., Label-Free Vapor Selectivity in Poly(p-Phenylene Oxide) Photonic Crystal Sensors. *ACS Appl. Mater. Interfaces* **2016,** *8*, 31941-31950.
(22) K. Unger, R. R., C. Czibula, C. Ganser, C. Teichert, G. Jakopic, G. Canazza, S. Gazzo, D. Comoretto In *Distributed Bragg reflectors: Morphology of cellulose acetate and polystyrene multilayer*, 6th International Conference on Transparent Optical Networks (ICTON), Graz, Austria, Graz, Austria, 2014; pp 1-4.
(23) Canazza, G.; Scotognella, F.; Lanzani, G.; Silvestri, S. D.; Zavelani-Rossi, M.; Comoretto, D., Lasing from All-polymer Microcavities. *Laser Phys. Lett.* **2014,** *11*, 035804.
(24) Manfredi, G.; Mayrhofer, C.; Kothleitner, G.; Schennach, R.; Comoretto, D., Cellulose ternary photonic crystal created by solution processing. *Cellulose* **2016,** *23*, 2853-2862.
(25) Knarr III, R. J.; Manfredi, G.; Martinelli, E.; Pannocchia, M.; Repetto, D.; Mennucci, C.; Solano, I.; Canepa, M.; Buatier de Mongeot, F.; Galli, G.; Comoretto, D., In-plane Anisotropic Photoresponse in All-polymer Planar Microcavities. *Polymer* **2016,** *84*, 383-390
(26) Manfredi, G.; Lova, P.; Di Stasio, F.; Krahne, R.; Comoretto, D., Directional Fluorescence Spectral Narrowing in All-Polymer Microcavities Doped with CdSe/CdS Dot-in-Rod Nanocrystals. *ACS Photonics* **2017,** *4*, 1761-1769.
(27) Lova, P.; Manfredi, G.; Boarino, L.; Comite, A.; Laus, M.; Patrini, M.; Marabelli, F.; Soci, C.; Comoretto, D., Polymer Distributed Bragg Reflectors for Vapor Sensing. *ACS Photonics* **2015,** *2*, 537-543.
(28) Lova, P.; Manfredi, G.; Boarino, L.; Laus, M.; Urbinati, G.; Losco, T.; Marabelli, F.; Caratto, V.; Ferretti, M.; Castellano, M.; Soci, C.; Comoretto, D., Hybrid ZnO:polystyrene nanocomposite for all-polymer photonic crystals. *Phys. Status Solidi C* **2015,** *12*, 158-162.
(29) Menon, V. M.; Luberto, M.; Valappil, N. V.; Chatterjee, S., Lasing from InGaP Quantum Dots in a Spin-coated Flexible Microcavity. *Opt. Express* **2008,** *16*, 19535-19540.
(30) Komikado, T.; Yoshida, S.; Umegaki, S., Surface-emitting Distributed-feedback Dye Laser of a Polymeric Multilayer Fabricated by Spin Coating. *Appl. Phys. Lett.* **2006,** *89*, 061123.
(31) Scotognella, F.; Monguzzi, A.; Cucini, M.; Meinardi, F.; Comoretto, D.; Tubino, R., One Dimensional Polymeric Organic Photonic Crystals for DFB Lasers. *Int. J. Photoenergy* **2008,** *2008*, 4.
(32) Di Stasio, F.; Grim, J. Q.; Lesnyak, V.; Rastogi, P.; Manna, L.; Moreels, I.; Krahne, R., Single-Mode Lasing from Colloidal Water-Soluble CdSe/CdS Quantum Dot-in-Rods. *Small* **2015,** *11*, 1328-1334.
(33) Moreels, I.; Rainò, G.; Gomes, R.; Hens, Z.; Stöferle, T.; Mahrt, R. F., Nearly Temperature-Independent Threshold for Amplified Spontaneous Emission in Colloidal CdSe/CdS Quantum Dot-in-Rods. *Adv. Mater.* **2012,** *24*, OP231-OP235.
(34) Grim, J. Q.; Christodoulou, S.; Di Stasio, F.; Krahne, R.; Cingolani, R.; Manna, L.; Moreels, I., Continuous-wave Biexciton Lasing at Room Temperature using Solution-processed Quantum Wells. *Nat. Nanotechnol.* **2014,** *9*, 891-895.
(35) Burda, C.; Chen, X.; Narayanan, R.; El-Sayed, M. A., Chemistry and Properties of

Nanocrystals of Different Shapes. *Chem. Rev.* **2005,** *105*, 1025-1102.
(36) Alivisatos, A. P., Semiconductor Clusters, Nanocrystals, and Quantum Dots. *Science* **1996,** *271*, 933.
(37) Sun, Q.; Wang, Y. A.; Li, L. S.; Wang, D.; Zhu, T.; Xu, J.; Yang, C.; Li, Y., Bright, Multicoloured Light-emitting Diodes Based on Quantum Dots. *Nat. Photonics* **2007,** *1*, 717-722.
(38) Grim, J. Q.; Manna, L.; Moreels, I., A Sustainable Future for Photonic Colloidal Nanocrystals. *Chem. Soc. Rev.* **2015,** *44*, 5897-5914.
(39) Angeloni, I.; Raja, W.; Brescia, R.; Polovitsyn, A.; De Donato, F.; Canepa, M.; Bertoni, G.; Proietti Zaccaria, R.; Moreels, I., Disentangling the Role of Shape, Ligands, and Dielectric Constants in the Absorption Properties of Colloidal CdSe/CdS Nanocrystals. *ACS Photonics* **2016,** *3*, 58-67.
(40) http://www.nanosysinc.com/ (accessed 07/20/2017).
(41) Murray, C. B.; Norris, D. J.; Bawendi, M. G., Synthesis and Characterization of Nearly Monodisperse CdE (E = Sulfur, Selenium, Tellurium) Semiconductor Nanocrystallites. *J. Am. Chem. Soc.* **1993,** *115*, 8706-8715.
(42) Peng, X.; Manna, L.; Yang, W.; Wickham, J.; Scher, E.; Kadavanich, A.; Alivisatos, A. P., Shape Control of CdSe Nanocrystals. *Nature* **2000,** *404*, 59-61.
(43) Qu, L.; Peng, X., Control of Photoluminescence Properties of CdSe Nanocrystals in Growth. *J. Am. Chem. Soc.* **2002,** *124*, 2049-2055.
(44) Mashford, B. S.; Stevenson, M.; Popovic, Z.; Hamilton, C.; Zhou, Z.; Breen, C.; Steckel, J.; Bulovic, V.; Bawendi, M.; Coe-Sullivan, S.; Kazlas, P. T., High-efficiency Quantum-dot Light-emitting Devices with Enhanced Charge Injection. *Nat. Photonics* **2013,** *7*, 407-412.
(45) Di Stasio, F.; Polovitsyn, A.; Angeloni, I.; Moreels, I.; Krahne, R., Broadband Amplified Spontaneous Emission and Random Lasing from Wurtzite CdSe/CdS "Giant-Shell" Nanocrystals. *ACS Photonics* **2016,** *3*, 2083-2088.
(46) Dang, C.; Lee, J.; Breen, C.; Steckel, J. S.; Coe-Sullivan, S.; Nurmikko, A., Red, green and blue lasing enabled by single-exciton gain in colloidal quantum dot films. *Nat. Nanotechnol.* **2012,** *7*, 335-339.
(47) Park, Y.-S.; Bae, W. K.; Baker, T.; Lim, J.; Klimov, V. I., Effect of Auger Recombination on Lasing in Heterostructured Quantum Dots with Engineered Core/Shell Interfaces. *Nano Lett.* **2015,** *15*, 7319-7328.
(48) Klimov, V. I.; Ivanov, S. A.; Nanda, J.; Achermann, M.; Bezel, I.; McGuire, J. A.; Piryatinski, A., Single-exciton optical gain in semiconductor nanocrystals. *Nature* **2007,** *447*, 441-446.
(49) Kelestemur, Y.; Cihan, A. F.; Guzelturk, B.; Demir, H. V., Type-tunable amplified spontaneous emission from core-seeded CdSe/CdS nanorods controlled by exciton-exciton interaction. *Nanoscale* **2014,** *6*, 8509-8514.
(50) Grivas, C.; Li, C.; Andreakou, P.; Wang, P.; Ding, M.; Brambilla, G.; Manna, L.; Lagoudakis, P., Single-mode tunable laser emission in the single-exciton regime from colloidal nanocrystals. *Nat. Commun.* **2013,** *4*, 2376.
(51) Fan, F.; Voznyy, O.; Sabatini, R. P.; Bicanic, K. T.; Adachi, M. M.; McBride, J. R.; Reid, K. R.; Park, Y.-S.; Li, X.; Jain, A.; Quintero-Bermudez, R.; Saravanapavanantham, M.; Liu, M.; Korkusinski, M.; Hawrylak, P.; Klimov, V. I.; Rosenthal, S. J.; Hoogland, S.; Sargent, E. H., Continuous-wave lasing in colloidal quantum dot solids enabled by facet-selective epitaxy.

Nature **2017,** *544*, 75-79.
(52) Adachi, M. M.; Fan, F.; Sellan, D. P.; Hoogland, S.; Voznyy, O.; Houtepen, A. J.; Parrish, K. D.; Kanjanaboos, P.; Malen, J. A.; Sargent, E. H., Microsecond-sustained lasing from colloidal quantum dot solids. *Nat. Commun.* **2015,** *6*, 8694.
(53) Stasio, F. D.; Berti, L.; Burger, M.; Marabelli, F.; Gardin, S.; Dainese, T.; Signorini, R.; Bozio, R.; Comoretto, D., Amplified Spontaneous Emission from Opal Photonic Crystals Engineered with Structural Defects. *PCCP* **2009,** *11*, 11515-11519.
(54) Einstein, A., Quantentheorie der Strahlung. *Phys. Z.* **1917,** *18*, 121-128.
(55) Yariv, A., *Quantum electronics*. Third ed.; John Wiley & Sons: United States of America, 1988.
(56) Carbone, L.; Nobile, C.; De Giorgi, M.; Sala, F. D.; Morello, G.; Pompa, P.; Hytch, M.; Snoeck, E.; Fiore, A.; Franchini, I. R.; Nadasan, M.; Silvestre, A. F.; Chiodo, L.; Kudera, S.; Cingolani, R.; Krahne, R.; Manna, L., Synthesis and Micrometer-Scale Assembly of Colloidal CdSe/CdS Nanorods Prepared by a Seeded Growth Approach. *Nano Lett.* **2007,** *7*, 2942-2950.
(57) Lova, P.; Grande, V.; Manfredi, G.; Patrini, M.; Herbst, S.; Würthner, F.; Comoretto, D., All-Polymer Photonic Microcavities Doped with Perylene Bisimide J-Aggregates. *Adv. Opt. Mater.*, DOI: 10.1002/adom.201700523.
(58) Fornasari, L.; Floris, F.; Patrini, M.; Comoretto, D.; Marabelli, F., Demonstration of fluorescence enhancement via Bloch surface waves in all-polymer multilayer structures. *PCCP* **2016,** *18*, 14086-14093.
(59) Comoretto, D.; Dellepiane, G.; Cuniberti, C.; Rossi, L.; Borghesi, A.; Le Moigne, J., Photoinduced absorption of oriented poly[1,6-di(N-carbazolyl)-2,4-hexadiyne]. *Phys. Rev. B* **1996,** *53*, 15653-15659.
(60) Lanzani, G.; Zavelani-Rossi, M.; Cerullo, G.; Comoretto, D.; Dellepiane, G., Real-time observation of coherent nuclear motion in polydiacetylene isolated chains. *Phys. Rev. B* **2004,** *69*, 134302.
(61) Svelto, O., *Principles of Lasers*. 4th Edition ed.; Springer Science + Business Media, Inc.: New York, 1998.
(62) Shkunov, M. N.; DeLong, M. C.; Raikh, M. E.; Vardeny, Z. V.; Zakhidov, A. A.; Baughman, R. H., Photonic versus Random Lasing in Opal Single Crystals. *Synth. Met.* **2001,** *116*, 485.
(63) Polson, R. C.; Vardeny, Z. V., Organic random laser in the weak-scattering regime. *Phys. Rev. B* **2005,** *71*, 045205.
(64) Hecht, E., *Optics*. Addison-Wesley: San Francisco, 2002.
(65) Takeuchi, H.; Natsume, K.; Suzuki, S.; Sakata, H., Microcavity Distributed-feedback Laser using Dye-doped Polymeric Thin Films. *Electron. Lett* **2007,** *43*, 30-32.
(66) Goldenberg, L. M.; Lisinetskii, V.; Gritsai, Y.; Stumpe, J.; Schrader, S., Second Order DFB Lasing using Reusable Grating Inscribed in Azobenzene-containing Material. *Opt. Mater. Express* **2012,** *2*, 11-19.
(67) Palatnik, A.; Aviv, H.; Tischler, Y. R., Microcavity Laser Based on a Single Molecule Thick High Gain Layer. *ACS Nano* **2017,** *11*, 4514-4520.
(68) Ding, Y.; Fan, H.; Zhang, X.; Jiang, X.; Xiao, M., Ultralow-threshold neodymium-doped microsphere lasers on a silicon chip. *Opt. Commun.* **2017,** *395*, 51-54.
(69) Lee, T.-W.; Park, O. O.; Cho, H. N.; Kim, D. Y.; Kim, Y. C., Low-threshold lasing in a

microcavity of fluorene-based liquid-crystalline polymer blends. *J. Appl. Phys.* **2003,** *93*, 1367-1370.
(70) Palatnik, A.; Tischler, Y. R., Solid-State Rhodamine 6G Microcavity Laser. *IEEE Photon. Technol. Lett.* **2016,** *28*, 1823-1826.
(71) Persano, L.; Camposeo, A.; Carro, P. D.; Mele, E.; Cingolani, R.; Pisignano, D., Low-threshold blue-emitting monolithic polymer vertical cavity surface-emitting lasers. *Appl. Phys. Lett.* **2006,** *89*, 121111.
(72) Sun, H.; Chen, X.; Wang, H.; Lu, Q.; Yang, H.; Xie, S.; Wu, X., Fabrication of Lasing Whispering Gallery Mode Microresonators by Controllable Injection Method. *IEEE Photon. J.* **2017,** *9*, 1-6.
(73) Yoshioka, H.; Ota, T.; Chen, C.; Ryu, S.; Yasui, K.; Oki, Y., Extreme ultra-low lasing threshold of full-polymeric fundamental microdisk printed with room-temperature atmospheric ink-jet technique. *Sci. Rep.* **2015,** *5*, 10623.
(74) Manfredi, G.; Lova, P.; Stasio, F. D.; Rastogi, P.; Krahne, R.; Comoretto, D., Lasing from Dot-in-Rod Nanocrystals in Planar Polymer Microcavities. **In preparation**.

Conclusions

In this thesis, we reported results obtained creating all-polymer photonic crystals and microcavities. The systems are planar multilayer structures allowing to manipulate light propagation as well as light-matter interaction through simple and versatile methods. These types of photonic devices can be mass produced as proven by products already on the market. Moreover, they can be built starting from cheap materials and are very promising for future applications. To create the photonic crystals, we rely on spin coating. Although this technique could be not fully appealing on industrial scale, it is also very reliable and versatile on a lab scale. It allows to create proof-of-concept devices at very cheap costs and in relatively limited times using non-expensive equipment.

In chapter 2 we have shown how high optical quality polymer films can be spin coated and how the thickness, thickness homogeneity, refractive index, and surface roughness depend on the main process parameters. We supplied rules of thumbs and laws that are followed by many processes. We have also shown the parameters for the main commercial polymers used in the creation of DBRs and studied their optical response.

In chapter 3 we have described a permeation model of analytes through all-polymer and composite DBRs. Such DBRs have been shown to act as transducers of vapor phase chemical stimuli to an optical response. We have developed a model in order to account for the change of the optical response upon exposure to different analytes. Although we focused on the modelling of the response, we also supplied experimental results on moisture sensing with ad hoc developed ternary photonic structures.

In chapter 4 we have shown the production of a polymer microcavity containing easily tunable emitting nanocrystals embedded in a nanocomposite layer. We studied the optical response of the system and highlighted all the modifications induced by the photonic crystal. Such device, reaching a very high quality factor, can be used to fine tune the spectral properties of emitters and to obtain directional emission. Such result may be interesting for the study of photonic properties of materials and to obtain emission rate enhancement which would grant important repercussion in the development of more efficient LEDs.

In chapter 5 we have shown lasing in a polymer VCSEL containing emitting nanocrystals. Such devices, produced through an unusual process, envisage the production of cheap and efficient lasers that can be used for low power applications like data transfer in big data mining centers or in fiber communication systems. Indeed, despite the use of simple processes and the creation of a still non-optimized device, we obtained an interestingly low lasing threshold which encourages to further develop this kind of structure.

All results here shown encourage future developments in the field of polymer planar photonic crystals as they provide interesting and potentially scalable solutions for different technological problems such as disposable sensors, large area light source and cheap lasers.

Publications list

In preparation or close to submission

Lasing from Dot-in-Rod Nanocrystals in Planar Polymer Microcavities
Giovanni Manfredi, Paola Lova, Francesco Di Stasio, Prachi Rastogi, Roman Krahne, Davide Comoretto

Determination of Vapor Diffusion Coefficient and Label-free Selectivity by All-Polymer Distributed Bragg Reflectors
Paola Lova, **Giovanni Manfredi**, Alberto Servida, Davide Comoretto

Spin coating of polymer films for photonic structures
Giovanni Manfredi, Hartmut Fröb, Karl Leo, Davide Comoretto

Papers in peer reviewed journals

7 **All-Polymer Photonic Microcavities Doped with Perylene Bisimide J-Aggregates**
Paola Lova, Vincenzo Grande, **Giovanni Manfredi**, Maddalena Patrini, Stefanie Herbst, Frank Würthner, Davide Comoretto
Advanced Optical Materials, **2017,** DOI: 10.1002/adom.201700523

6 **Directional Fluorescence Spectral Narrowing in All-Polymer Microcavities Doped with CdSe/CdS Dot-in-Rod Nanocrystals**
Giovanni Manfredi, Paola Lova, Francesco Di Stasio, Roman Krahne, Davide Comoretto
ACS Photonics, **2017**, Volume 4, pp 1761-1769

5 **Cellulose ternary photonic crystal created by solution processing**
Giovanni Manfredi, Claudia Mayrhofer, Gerald Kothleitner, Robert Schennach, Davide Comoretto
Cellulose, **2016**, Volume 23, pp 2853-2862

4 **In-plane anisotropic photoresponse in all-polymer planar microcavities**
Robert J. Knarr III, **Giovanni Manfredi**, Elisa Martinelli, Matteo Pannocchia, Diego Repetto, Carlo Mennucci, Ilaria Solano, Maurizio Canepa, Francesco Buatier de Mongeot, Giancarlo Galli, Davide Comoretto
Polymer, **2016**, Volume 84, pp 383-390

3 **High Refractive Index Hyperbranched Polyvinylsulfides for planar one-dimensional all-polymer photonic crystals**
Serena Gazzo, **Giovanni Manfredi**, Robert Pötzsch, Qiang Wei, Marina Alloisio, Brigitte Voit, Davide Comoretto
Journal of Polymer Science PART B: Polymer Physics, **2015**, Volume 54 (1), pp 73-80

2 **Polymer Distributed Bragg Reflectors for Vapor Sensing**
Paola Lova, **Giovanni Manfredi**, Luca Boarino, Antonio Comite, Michele Laus, Maddalena Patrini, Franco Marabelli, Cesare Soci, Davide Comoretto
ACS Photonics, **2015**, Volume 2 (4), pp 537–543

1 **Hybrid ZnO:polystyrene nanocomposite for all-polymer photonic crystals**
Paola Lova, **Giovanni Manfredi**, Luca Boarino, Michele Laus, Giulia Urbinati, Tonia Losco, Franco Marabelli, Valentina Caratto, Maurizio Ferretti, Maila Castellano, Cesare Soci, Davide Comoretto
Physica Status Solidi (C), **2015**, Volume 12, pp 158-162

Book contributions

Organic & Hybrid Photonic Crystals
Edited by Davide Comoretto, Springer, Berlin. **2015**

Spin coated Polymer and Hybrid Multilayers and Microcavities
Francesco Scotognella, Simone Varo, Luigino Criante, Serena Gazzo, **Giovanni Manfredi**, Robert J. Knarr III, Davide Comoretto

Conference communications

2017

EMRS Fall meeting (Warsaw, September 17-21 2017)

Hybrid polymer inorganic microcavities using CdSe/CdS nanorods: from fluorescence enhancement to lasing — Oral, **Speaker**
Giovanni Manfredi, Paola Lova, Francesco Di Stasio, Roman Krahne, Davide Comoretto

International School on Hybrid and Organic Photovoltaics ISOPHOS (Arbatax, September 3-7 2017)

Fluorescence enhancement and lasing from hybrid polymer inorganic microcavities containing CdSe/CdS nanorods — Poster, **Presenter**, **Poster award**
Giovanni Manfredi, Paola Lova, Francesco Di Stasio, Roman Krahne, Davide Comoretto

Macrogiovani 2017 (Trento, June 22-23)

Polymer and Hybrid Materials for Photonic Crystals — Oral, **Speaker**
Giovanni Manfredi, Paola Lova, Pavlo Perkhun, Alba Surace, Davide Comoretto

Polymer and Hybrid Materials for Photonic Crystals — Poster, **Author**
Giovanni Manfredi, Paola Lova, Pavlo Perkhun, Alba Surace, Davide Comoretto

EPF Summer School - Transport Phenomena in Polymers and Hybrid Materials (Gargnano, May 14-19)

Polymer Photonic Crystals — Poster, **Author**
Giovanni Manfredi, Alba Surace, Pavlo Perkhun, Paola Lova, Davide Comoretto

2016

EOSAM 2016 (Berlin, September 26-30)

Hybrid polymer inorganic microcavities with CdSe/CdS nanocrystals — Oral, **Speaker**
Giovanni Manfredi, Francesco di Stasio, Roman Krahne, Davide Comoretto

Tailoring One-Dimensional Photonic Crystals with Embedded Silver Nanoparticles — Poster, **Co-author**
Marina Alloiso. Eliana Piccinini, Massimo Ottonelli, **Giovanni Manfredi**, Davide Comoretto

ESOPS20 (Dresden, September 11-14)

Hybrid polymer inorganic microcavities with CdSe/CdS nanocrystals — Poster, **Presenter**, **Poster award**
Giovanni Manfredi, Paola Lova, Chiara Bastianini, Paolo Giusto, Davide Comoretto

2015

ICES 15 (Messina, October 12-15)

Hybrid polymer inorganic microcavities with CdSe/CdS nanocrystals — Poster, **Presenter**
Giovanni Manfredi, Francesco di Stasio, Roman Krahne, Davide Comoretto

ECOF 14 (Genova, June 29 – July 2)

All-polymer flexible Distributed Bragg Reflectors and Microcavities — Oral, **Speaker**
Giovanni Manfredi, Serena Gazzo, Robert J. Knarr III, Eliana Piccinini, Marina Alloisio, Davide Comoretto

15th European Polymer Federation Congress (Dresden, June 21 - 26)

Vapor Sensing by All-polymer 1D Planar Photonic Crystals — Oral, **Co-author**
Paola Lova, Maddalena Patrini, Franco Marabelli, Giorgio Guizzetti, **Giovanni Manfredi**, Antonio Comite, Michele Laus, Luca Boarino, Graziella Ianniello, Paola Rizzo, Christophe Daniel, Gaetano Guerra, Cesare Soci, Davide Comoretto

All-polymer Flexible Photoresponsive Microcavities — Poster, **Co-author**
Robert J. Knarr III, **Giovanni Manfredi**, Elisa Martinelli, Matteo Pannocchia, Giancarlo Galli, Davide Comoretto

SPP 2015 (Santa Margherita Ligure, June 7-10)

Plasmonic Nanostructures @ Photonic Crystals — Poster, **Co-author**
Davide Comoretto, Valentina Robbiano, Marco Cucini, **Giovanni Manfredi**, Eliana Piccinini, Marina Alloisio

Fourth International Symposium Frontiers in Polymer Science (Riva del Garda, May 20-22)

Polymer Photonic Crystal Structures — Poster, **Co-author**
Emanuele Bozzoni, Simone Congiu, Serena Gazzo, Robert J. Knarr III, Filippo La Rosa, **Giovanni Manfredi**, Davide Comoretto, Paola Lova, Cesare Soci, Graziella Ianniello, Paola Rizzo, Christophe Daniel, Gaetano Guerra, Elisa Martinelli, Giancarlo Galli, Katia Sparnacci, Michele Laus, Luca Boarino, Massimiliano Lanzi, Giampaolo Zuccheri

EMRS Spring Meeting 2015 (Lille, May 11-15)

Poster
Presenter
Oral
Speaker

Hybrid polymer inorganic microcavities using CdSe/CdS nanorods

Giovanni Manfredi, Francesco Di Stasio, Roman Krahne, Davide Comoretto

Polymer Photonic Crystal Vapor Sensors

Paola Lova, Maddalena Patrini, Franco Marabelli, **Giovanni Manfredi**, Antonio Comite, Michele Laus, Luca Boarino, Graziella Ianniello, Paola Rizzo, Christophe Daniel, Gaetano Guerra, Cesare Soci, Davide Comoretto

Acknowledgments

For the work of this thesis I would like to thank the University of Genova. Some special thanks go to Prof. Adriana Saccone for the hard work in coordinating the PhD course. I'd also like to thank the administrative part of the Department of Chemistry and of the University for the patience shown in solving funding problems and in particular Anna Barabino, Paolo Mosto, and the pro-rector Prof. Enrico Giunchiglia.
Special thanks to the Technical University of Dresden and to the Institute for Applied Photophysics for hosting me during my period abroad. I would like to thank the Prof. Karl Leo for giving me the possibility to work in their institute and Prof. Hartmut Fröb for accepting me in the Olaser group.
I'd like to thanks Prof. Robert Schennach for the collaboration and for the genuine interest he showed in every request and every communication.
I also thank Roman Krahne and Francesco Di Stasio for the collaboration and the discussions about the best strategies to use in order to bring ahead the work.
The thesis work would have not been possible without the support of the Italian Ministry of University, Research and Instruction through the funding "Progetti di Ricerca di Rilevante Interesse Nazionale 2010−2011" Program (Materiali Polimerici Nanostrutturati con strutture molecolari e cristalline mirate, per tecnologie avanzate e per l'ambiente, 2010XLLNM3).
Some thanks must be also given to the support by the European Union's Horizon 2020 research and innovation program under the Marie Sklodowska-Curie Grant Agreement No. 643238.

Ringraziamenti

Quest'ultima parte è l'unica in italiano. Ho relegato all'inglese la parte un po' più istituzionale dei ringraziamenti per lasciare alla mia lingua madre i ringraziamenti più sentiti.
Vorrei innanzitutto ribadire i miei ringraziamenti ad Anna Barabino, Paolo Mosto ed al prorettore Prof. Enrico Giunchiglia per l'interesse dimostrato alla mia situazione creata da un regolamento lacunoso. Ringrazio ancora per l'impegno e la solerzia dimostrate nel risolvere i problemi. Aggiungo ulteriori ringraziamenti ad Anna Barabino per la pazienza portata verso di me e verso tutti perché non siamo molto pratici con la burocrazia e la consegna di "carta".
Vorrei inoltre ringraziare di nuovo la Prof.ssa Adriana Saccone per l'impegno con cui amministra il Dipartimento di Chimica ed i corsi di dottorato.
Un ringraziamento speciale va a Roman Krahne e a Francesco Di Stasio, che sono stati sì collaboratori, ma sempre disponibili alla discussione ed all'incontro.
Vorrei ringraziare Marco Liscidini per le numerose delucidazioni teoriche, le chiacchierate e per avermi permesso di seguire il corso da lui tenuto.
Inevitabilmente, in questi anni, sono venuto a contatto con un gran numero di persone durante i miei studi di dottorato. Studenti, collaboratori, amministrativi, professori. Ognuno ha avuto il suo ruolo, piccolo o grande che sia, e per questo vorrei ringraziarlo.
Non posso però non spendere qualche riga in più per coloro coi quali ho formato un legame un po' più stretto.
Innanzitutto quel cazzone di Paolo Giusto che è andato a fare il figo a Potsdam. Avremmo tutti voluto ti fossi fermato da noi ma hai scelto la tua strada e mi sento di dirti che hai fatto bene. Ti auguro tutte le fortune possibili e di riuscire a crearti una carriera coi fiocchi e di recuperare tonnellate di filtri di sigarette. In bocca al lupo.
Ad Alba ANTONELLA Surace dico grazie per il supporto morale in un momento difficile e la disponibilità ad ascoltare le mie menate. E se è vero che il favore è stato largamente ricambiato per tutte le tue fregnacce e piagnistei, è anche vero che la musica trash in laboratorio è stata un punto di forza del tutto. Quindi aggiungo solo: "Portami l'acqua che c'ho sete".
Paola Lova è sempre stata un punto di riferimento storico per tutti noi dentro al laboratorio. Col suo modo di fare un po' da mamma e un po' da scassaballe ha saputo dare un tocco in più alle giornate. Inutile ricordare tutti gli spritz bevuti e le invettive tirate contro gli studenti. Grazie di tutto e in bocca al lupo per la tua ricerca del leggendario "posto fisso".
Ringrazio anche Filippo, Serena, Selena, Gabriele e Marco per la compagnia in laboratorio e tutti i ragazzi del progetto Synchronics per le cene insieme.
Ringrazio apertamente Davide Comoretto per essere stato ben più di un semplice supervisor. Al di là di caramelle, cioccolatini e pranzi offerti, ci hai sempre lasciati liberi di provare, di autogestirci e ci hai cazziato quando era il momento giusto. Non ti sei mai fatto remore ad esporre la tua visione delle cose ed a fornire consiglio. Gli insegnamenti dati vanno ben oltre il professionale. Anche se non sei mai riuscito a portare molta finezza nel laboratorio (pessima scelta delle donne), sei riuscito a creare un piccolo ambiente davvero

caloroso dove tutti vorrebbero lavorare.
Devo dire che il giorno in cui ho lasciato il laboratorio una lacrima mi è scesa e lo devo a tutti a voi.
Grazie.
Ma un ringraziamento va a tutti nella mia vita, a tutte le persone, a tutti quelli che hanno avuto un ruolo piccolo o grande nel mio evolvere come persona. A chi c'è, c'è stato o ci sarà.
A Genova, città di cui mi sono innamorato. Città che lascia un segno nell'animo nonostante i modi bruschi, o forse proprio grazie a quelli.
Ai miei amici, anche se li sento poco: Lorenzo, Nick, Arjola, Jonny, Monta, Luca, Dany. Un po' tutti.
Tutto l'affetto va ai miei genitori ed ai miei fratelli. A loro il merito di avermi educato, di avermi supportato e di avermi anche convinto ad intraprendere la strada che ho preso senza paure. Solo ultimamente però mi rendo conto che mi hanno trasmesso anche di più, mi hanno fatto capire com'è che voglio sia il mondo a venire, mi hanno trasmesso un pezzo di loro e mi sento in dovere di difenderlo e portarlo avanti.
Ed alla fine, voglio concludere con Roberta. Ci siamo conosciuti da poco e non hai avuto effettivamente un ruolo preponderante durante il mio dottorato. Nonostante questo, direi che mi hai abbastanza stravolto le idee e mai avrei pensato di poter essere talmente sincero ed a mio agio con una persona. Mai avrei pensato di poter trovare tante certezze in una voce e tanto amore nei modi. Risparmierò le cose più personali per noi due però grazie a te, perché se ultimamente sono più sereno, se non ho stress nello scrivere questa tesi, sappi che molto del merito è tuo.